6. Asignación estructural de las bandas de proteínas en espectroscopia de infrarrojo

La asignación de bandas es un paso necesario, tanto para obtener una estimación de estructura secundaria a partir de espectros de IR, como para otras informaciones estructurales. Con el tiempo varios autores han propuesto intervalos de aparición de diferentes estructuras, principalmente para hélices alfa, láminas beta, giros reversos y estructuras no ordenadas (ver punto 2.2.2 de la Introducción). Estos intervalos son guías útiles para una asignación estándar, y permite a los no iniciados en la técnica asignar bandas de una manera justificada. Sin embargo, estos intervalos son utilizados a veces sin reconocer sus limitaciones y problemas: A) Los límites varían según el autor, a veces de manera importante. B) Los límites propuestos para las diferentes estructuras muestran un grado variable de solapamiento y el usuario ha de decidir en estos casos la asignación.

Los intervalos propuestos se basan tanto en cálculos teóricos como en estudios experimentales con péptidos que adoptan una estructura secundaria pura o semipura, pero principalmente se basan en los resultados obtenidos en proteínas con estructura tridimensional conocida. En este caso se asignan bandas para encontrar una concordancia entre la estimación de estructura secundaria obtenida por IR y la obtenida por otros métodos espectroscópicos o la obtenida directamente a partir de su estructura cristalográfica.

En conclusión, la ambigüedad en la asignación de bandas deja una libertad relativamente grande a la interpretación de los espectros de IR, de tal manera que la experiencia, la corazonada o los prejuicios del investigador o el estado del conocimiento del momento tendrán cierto peso en la asignación estructural.

En este capitulo se pretende realizar un estudio bibliográfico crítico que reúna las diferentes fuentes para realizar la asignación de bandas en la amida I (y amida II). Estas fuentes son estudios teóricos sobre estructuras estándares, de polipéptidos y de proteínas, estudios experimentales sobre péptidos o proteínas que adoptan una única estructura o una estructura mayoritaria, y proteínas de estructura conocida; en este último caso estudiadas tanto por ajuste de bandas como por técnica de reconocimiento de patrones. En los siguientes puntos detallaremos diferentes fuentes y en el último punto realizaremos una recopilación.

6.1. Estudios teóricos

Los estudios teóricos intentan determinar las frecuencias de vibración amida de una estructura peptídica. Para ello requieren la estructura tridimensional de la molécula, valores de la fuerza de los enlaces, el valor y ángulo de los diferentes momentos dipolares de transición amida (necesarios para determinar acoplamientos dipolares) y diferentes asunciones para simplificar el problema y hacerlo resoluble. Normalmente sólo se estudia las vibraciones amida I y amida II, y en algunas ocasiones el de la amida A u otras vibraciones amidas.

6.1.1. Hélices alfa

Existen dos conformaciones de hélices alfa, la α_I (la habitual) y la α_{II}. Ambas tienen el mismo número de aminoácidos por giro, 3,6, pero difieren en los ángulos diédricos ϕ y φ del enlace peptídico y en la longitud del puente de hidrógeno N-H···O=C (mayor para α_{II}). La conformación α_I es la habitual en proteínas, aunque la hélice α_{II} es candidata a encontrase en la bacteriorodopsina (Krimm y Bandekar, 1986).

Para una hélice alfa cada vibración amida se separa en diferentes modos de vibración: A, B y E (degenerado). Para una hélice infinita sólo los modos A y E_1 son activos en IR, mientras que en Raman son activos los modos A, E_1 y E_2. Para la vibración amida I el modo más intenso en IR es el A y en Raman el E_1. Para la amida II el modo más intenso es el E_1 en IR y Raman, aunque hay que decir que en Raman la amida II muestra muy poco intensidad. El modo de vibración A tiene la dirección del eje de la hélice (||) y el modo E es perpendicular ($\perp$) al eje de la hélice (Krimm y Bandekar, 1986; Nevskaya y Chirgadze, 1976).

Nevskaya y Chirgadze (1976) estudiaron teóricamente las frecuencias de vibración de la amida I y amida II de las hélices alfa. Para la estructura de la hélice utilizaron valores estándares de esta estructura.

Para hélices alfa infinitas determinan para la amida I que el modo E_1 aparece a 1657 cm^{-1} y el A sobre 1653 cm^{-1}. El modo A es el más intenso y representa el 75% del área, mientras que el modo E_1 representa el 25%. Para la amida II el modo E_1 aparece a 1544 cm^{-1} (93%) y el A sobre 1525 cm^{-1} (7%).

Para una hélice alfa finita regular el modo E_1 se separa en E_1' y E_1'' y, además, modos de vibración E de mayor orden se convierten en activos. Para la amida I el modo A sigue siendo el más intenso, pero en menor medida que para la hélice infinita. En algunos casos la separación entre el modo A y los modos E podría superar los 30 cm^{-1}. Además, el modo de vibración A, que determina en gran medida el máximo de vibración de las hélices alfa, sufre un desplazamiento en función del número *n* de residuos de la hélice. Así para $n = \infty$ $\nu = 1653$ cm^{-1}; para $n = 20$, $\nu = 1655$ cm^{-1}; y para $n = 10$, $\nu = 1663$ cm^{-1}. Para la amida II la longitud de la hélice tendría un efecto moderado en la frecuencia de vibración.

Chirgadze et al. (1976) estudiaron hélices alfa irregulares (los ángulos ϕ y φ varían aleatóriamente respecto a los valores estándares de residuo a residuo) mediante estudios teóricos y experimentales, y su efecto en la frecuencia y anchura de las bandas. Para una hélice regular calculan que su amida I tiene un máximo a 1653 cm^{-1}, para una hélice irregular el máximo se determina a 1650 cm^{-1} y la banda se hace mucho más ancha.

Krimm y Bandekar (1986) realizaron y recopilaron estudios teóricos y experimentales de su grupo. En los estudios teóricos de las hélices alfa asumieron estructuras infinitas, pues su simetría reduce el número de vibraciones y simplifica los cálculos. Los estudios de las hélices alfa se basaron en la estructura cristalina de la poli-Ala y poli-Glu cuando adoptan esta conformación.

Para los cálculos obtenidos para la poli-Ala el modo A se predice a 1657 cm^{-1}, el E_1 a 1655 cm^{-1} y el E_2 a 1645 cm^{-1} para la amida I, mientras que en la amida II tenemos 1519, 1538 y 1540 cm^{-1}

respectivamente (recordemos que en IR sólo los modos A y E_1 son activos). Los valores experimentales observados coinciden bien con las posiciones teóricas para las vibraciones A y E_1, así como su separación e intensidad relativa.

Respecto a las posiciones en la amida I' de la poli-Ala, los estudios teóricos predicen un desplazamiento de ≈ 10 cm^{-1} al sustituir el N-H amida por N-D, con posiciones para los modos A, E_1 y E_2 de 1647, 1648 y 1640 cm^{-1}, respectivamente. La amida II' mostrará los máximos a 1452, 1445 y 1445 cm^{-1}, respectivamente (Dwivedi y Krimm, 1984).

Para la estructura basada en la poli-Glu predicen bandas a 1657 cm^{-1} (A), 1655 (E_1) y 1645 (E_2) cm^{-1} para la amida I, y para la amida II a 1517 cm^{-1} (A), 1537 (E_1) y 1539 (E_2) cm^{-1} (Sengupta y Krimm, 1985). La coincidencia con los datos experimentales es también buena.

Reisdorf y Krimm (1995) estudiaron la separación entre el modo de vibración A y el E para vibraciones amida I, amida I' y amida II de hélices alfa de longitud finita, basados en los parámetros de la poli-Ala. Para $n = 10$ (longitud media de las hélices alfa en proteínas solubles (Pelton y McLean, 2000)) la separación entre la vibración A y E es de $\Delta\nu \approx 12$ cm^{-1} para la amida I, $\Delta\nu \approx 0$ cm^{-1} para la amida I' y $\Delta\nu \approx -15$ cm^{-1} para la amida II. Para $n = 25$ (longitud próxima a una hélice transmembrana) la separación entre la vibración A y E es de $\Delta\nu \approx 4$ cm^{-1} para la amida I, $\Delta\nu \approx -2$ cm^{-1} para la amida I' y $\Delta\nu \approx -17$ cm^{-1} para la amida II. Para todas las longitudes, para la amida I el área del modo A representa el 86% y el del E el 14% del total. Para la amida I' el modo A representa el 83% del área y E el 17%. Finalmente para la amida II el modo A representa el 11% del área y E el 89%.

Torii y Tasumi (1992a) realizaron una simulación de la vibración amida I' de la mioglobina,[*] centrándose en las frecuencias situadas en hélices alfa. Por lo tanto representa una novedad, pues utilizan las estructuras de hélices que se dan en una proteína, y que no sólo no son infinitas, sino que tienen distorsiones y curvaturas. Las simulaciones generan una vibración del modo A centrada a 1652 cm^{-1} (representa el 70% del área) y una vibración del modo E a 1642-1636 cm^{-1} (30% del área). La separación de ambas es por lo tanto de $\Delta\nu = 16\text{-}10$ cm^{-1}. Los autores destacan que la vibración E_1 cae en la zona asignada habitualmente a láminas beta, y por lo tanto puede dar lugar a una asignación errónea. Posteriormente estudian la posición de los modos A y E_1 para una hélice regular en función del número de residuos. Para $n = 200$ (hélice infinita) el modo A aparece a 1644 cm^{-1} y el E_1 a 1640 cm^{-1} ($\Delta\nu_{A\text{-}E} = 4$ cm^{-1}), para $n = 25$ el modo A aparece a 1649 cm^{-1} y el E_1 a 1641 cm^{-1} ($\Delta\nu_{A\text{-}E} = 8$ cm^{-1}) y para $n = 10$ el modo A aparece a 1656 cm^{-1} y el E_1 a 1642 cm^{-1} ($\Delta\nu_{A\text{-}E} = 14$ cm^{-1}).

[*] En realidad la simulación la realizaron con átomos de H, pero el cálculo se optimizó buscando concordancia con los espectros experimentales de varias proteínas, obtenidos en D_2O.

6.1.2. Hélices 3_{10}

Las hélices 3_{10} difieren de las hélices α en que éstas tienen tres aminoácidos por giro y forman puentes de hidrógeno $i \rightarrow i+3$ en vez de $i \rightarrow i+4$. La distancia del puente de hidrógeno N-H···O de estas dos hélices es semejante, 0,18 nm para 3_{10} y 0,19 nm para α (para α_{II} es 0,21 nm) (Krimm y Bandekar, 1986). Estas estructuras suelen aparecer en los extremos C y N de las hélices alfa, con una longitud media de 3 aminoácidos (una vuelta) (Tonino y Benedetti, 1991).

El homopolipéptido poliaminoisobutírico (poli-Aib) es un candidato a formar esta estructura. Krimm y Bandekar (1986) han recopilado los cálculos para el poli-Aib adoptando una conformación 3_{10} estándar (la estructura cristalina existente no determina la conformación exacta). Para la amida I calculan 1665 (A) y 1661 cm^{-1} (E) ($\Delta\nu_{A\text{-}E}$ = 4 cm^{-1}), y para la amida II 1533 (A) y 1547 (E) ($\Delta\nu_{A\text{-}E}$ = -14 cm^{-1}). Para la amida I' se calcula 1655 (A) y 1655 cm^{-1} (E) ($\Delta\nu_{A\text{-}E}$ = 0 cm^{-1}), y para la amida II' 1478 (A) y 1484 (E) ($\Delta\nu_{A\text{-}E}$ = -6 cm^{-1}) (Dwivedi et al., 1984). Hay que comentar que en este caso el acuerdo las posiciones teóricas y las experimentales no es muy bueno.

6.1.3. Láminas beta antiparalelas

Esta estructura se forma por la disposición en el mismo plano de varias cadenas peptídicas extendidas, con sentido opuesto entre cadenas contiguas. Existen dos tipos de conformaciones principales para las láminas beta antiparalelas: La ondulada (*rippled*) y la plana (*pleated*). Para láminas beta antiparalelas planas infinitas (cadenas infinitas y infinito número de cadenas) hay cuatro modos de vibración A, B_1, B_2 y B_3. Todos son activos en Raman, y tres de ellos, B_1, B_2 y B_3 son activos en IR. En IR para la amida I el modo de mayor intensidad es el B_2 y en la amida II el B_1. En Raman para la amida I y amida II el modo de mayor intensidad es el A. Si la orientación de las vibraciones se representa respecto a la dirección de las cadenas de las láminas, tenemos A (⊥), B_1 (||), B_2 (⊥) y B_3 (⊥) Para láminas beta antiparalelas onduladas infinitas se deducen cuatro modos de vibración, A_g, A_u, B_g y B_u, dos de ellos (A_u y B_u) activos en el infrarrojo. En IR para la amida I el modo de mayor intensidad es el B_u y en la amida II el A_u. En Raman para la amida I y amida II el modo de mayor intensidad es el A_g (Krimm y Bandekar, 1986; Chirgadze y Nevskaya, 1976a)

Chirgadze y Neuskaya (1976a) realizaron estudios teóricos para la vibración amida I en láminas beta antiparalelas planas. Cálculos basados en dos modelos diferentes dieron valores de B_1 a 1697±4 cm^{-1} (8% de área), de B_2 a 1628±3 cm^{-1} (91% del área) y B_3 a 1705±10 cm^{-1} (<1% del área). Para las láminas beta antiparalelas finitas hay que tener en cuenta la longitud de las cadenas y el número de cadenas. Si el número de cadenas es constante y aumentamos la longitud de las cadenas la separación entre B_1 y B_2 se mantiene constante. Por lo contrario si mantenemos constante la longitud de la cadena pero aumenta su número la separación entre B_1 y B_2 aumenta.

Krimm y Bandekar (1986) realizaron y recopilaron estudios teóricos y experimentales de su grupo. Consideraron láminas beta antiparalelas infinitas onduladas y planas. Los estudios de las láminas beta

antiparalelas planas se basaron en la estructura de la poli-Ala y de la poli-Ala-Gly cuando adopta esta conformación. Para la estructura basada en la poli-Ala las bandas en la amida I se calculan a 1670 (A), 1695 (B_1), 1630 (B_2) y 1698 (B_3) cm^{-1}, y en la amida II a 1539 (A), 1528 (B_1), 1562 (B_2) y 1592 (B_3) cm^{-1}. La concordancia entre las posiciones teóricas y experimentos es buena. Por otra parte se determinó (y observó) que con la sustitución del N-H amida por N-D las bandas amida sufren una reducción de su frecuencia de vibración en unos 5 cm^{-1}. Para la estructura basada en la poli-Ala-Gly se predice bandas en la amida I a 1661 (A), 1704 (B_1), 1630 (B_2) y 1699 (B_3) cm^{-1}. La concordancia entre teoría y experimentos es nuevamente buena.

Los estudios de las láminas beta antiparalelas onduladas se basaron en la estructura de la poli-Gly cuando adopta esta conformación. En la amida I se calculan a 1677 (A_g), 1689 (A_u), 1695 (B_g) y 1643 cm^{-1} (B_u), y en la amida II a 1514 (A_g), 1515 (A_u), 1602 (B_g) y 1572 cm^{-1} (B_u). La concordancia entre teoría y experimentos también es buena.

Torii y Tasumi (1992b) comparan los espectros experimentales desconvulados de varias proteínas (mioglobina, ribonucleasa A, α-lactalbumina, lisozima, flavodoxina, carboxipeptidasa A, concanavalina A y β-tripsina) en D_2O con los obtenidos mediante sus simulaciones. La concordancia es buena y les permite realizar las simulaciones restringiéndose a diferentes tipos de estructuras. Obtienen el espectro para las láminas beta antiparalelas que se dan en la concanavalina A y β-tripsina. La banda más intensa aparece a 1630 cm^{-1}, y se extiende una contribución constante desde 1685 a 1650 cm^{-1}, pero de poco intensidad. Para las láminas beta de la concanavalina A se da, además de la banda a 1630 cm^{-1}, dos bandas de menor intensidad a 1640 y 1615 cm^{-1}.

6.1.4. Láminas beta paralelas

Las láminas beta paralelas se diferencian de las antiparalelas en que todas las cadenas tienen el mismo sentido. Existen dos conformaciones principales, la ondulada y la plana. Para láminas beta paralelas planas sólo habrá dos modos de vibración: A (||) y B (⊥), ambas activas en IR y Raman. Para la amida I, A será intensa en Raman y B en IR. Para la amida II A será la más intensa en IR (todos los modos amida II son generalmente muy débiles en Raman). Para las láminas beta onduladas existen cuatro modos de vibración, A_1, A_2, B_1 y B_2, todos activos en Raman, y A_1, B_1 y B_2 activos en IR (Chirgadze y Nevskaya, 1976b; Bandekar y Krimm, 1988).

Chirgadze y Neuskaya (1676b) realizaron estudios teóricos para láminas beta paralelas planas infinitas, utilizando la estructura modelo. Los cálculos teóricos sitúan en la amida I el modo A sobre 1651 cm^{-1} (< 10% del área) y el modo B a 1637 cm^{-1} (> 90% del área).

Bandekar y Krimm (1988) también realizaron estudios teóricos para láminas beta paralelas infinitas, tanto onduladas como planas. Para las láminas beta paralelas planas las estructuras utilizadas son las canónicas aplicadas a la poli-Ala. Se calculan los modos de vibración en la amida I a 1663 (A) y 1642 (B) cm^{-1} y en la amida II a 1553 (A) y 1586 (B) cm^{-1}. Cuando se aplicaron los cálculos al tripéptido Val-Gly-

Gly, que forma láminas beta paralelas, se predijeron vibraciones a 1654 (A) y 1644 (B) cm^{-1} en la amida I, y a 1541 (A) cm^{-1} en la amida II. La concordancia con las posiciones observadas fue buena.

Para las láminas beta paralelas onduladas las estructuras utilizadas son las canónicas aplicadas a la poli-Gly. Se predice frecuencias para la amida I a 1647 (A_1), 1776 (A_2), 1696 (B_1) y 1680 (B_2) cm^{-1}, y en la amida II a 1530 (A_1), 1535 (A_2), 1568 (B_1) y 1573 (B_2) cm^{-1}.

Torii y Tasumi (1992b) obtuvieron la contribución en la amida I' de las láminas beta paralelas de la flavodoxina. Aparecen tres bandas de intensidad semejante sobre 1640 cm^{-1}, 1635 cm^{-1} y 1630 cm^{-1}. Por encima de 1650 cm^{-1} su contribución es casi nula.

6.1.5. Giros reversos

Krimm y Bandekar (1986) consideran dos tipos de giros reversos. En los giros β, los más abundantes en proteínas, se ven implicados cuatro aminoácidos y en los giros γ, minoritarios, tres. Al no poseer simetría, aparecen tantos modos de vibración como aminoácidos implicados en el giro. Dentro de los giros β y γ existen variantes. Se basan en estructuras modelo para obtener las frecuencias.

Para los giros β en la amida I se predicen bandas desde 1705 a 1640 cm^{-1}, centradas principalmente entre 1685-1660 cm^{-1}, y en la amida II desde 1575 a 1515 cm^{-1}, centradas principalmente entre 1640 y 1660 cm^{-1}. Utilizando la estructura de la insulina determinan las vibraciones teóricas de diversos giros β de ésta. Para la amida I todas las vibraciones caen entre 1700 y 1645 cm^{-1} y la mayoría entre 1685 y 1655 cm^{-1} (Krimm y Bandekar, 1986; Bandekar, 1993).

Para los giros γ se predicen bandas desde 1685 a 1650 cm^{-1} en la amida I y desde 1550 a 1500 cm^{-1} para la amida II (Krimm y Bandekar, 1986; Bandekar, 1993).

6.1.5. Otras estructuras

Torii y Tasumi (1992b) obtuvieron la contribución en la amida I' de las estructuras que no son ni hélices alfa ni láminas beta para diversas proteínas (mioglobina, ribonucleasa A, α-lactalbumina, lisozima, flavodoxina, carboxipeptisasa A, concanavalina A y β-tripsina). Esta contribución puede considerarse formada principalmente por giros reversos y estructuras irregulares. La contribución en la amida I' de estas estructuras tiene forma de una banda ancha e irregular centrada sobre 1655 cm^{-1}, que se extiende desde 1685 a 1620 cm^{-1}. En algunos casos esta contribución parece consistir en dos bandas anchas centradas a 1665 y 1645 cm^{-1}. Según los autores la primera podría corresponder principalmente a los giros reversos y la segunda a las estructuras irregulares.

6.2. Estudios experimentales con polipéptidos y proteínas de estructura secundaria pura

Existen un numeroso grupo de polipéptidos que adoptan una estructura pura, normalmente hélices alfa o láminas beta antiparalelas. Además, algunos polipéptidos no se estructuran y adoptando una

conformación al azar. También existen proteínas fibrilares que adoptan una estructura pura. Estudiando estos polipéptidos y proteínas fibrilares obtenemos de manera experimental las contribuciones en la amida I y amida II de diferentes estructuras.

6.2.1. Hélices alfa

Neuskaya y Chirgadze (1976) recopilan valores obtenidos por IR y Raman para catorce polipéptidos que adoptan una conformación hélice alfa, en disolución o en sólidos. Para doce de los polipéptidos el valor medio del máximo para la amida I ocurre en IR a 1654±3 (A) cm^{-1} y en Raman a 1654±4 (E_1). Para la amida II se detectan dos bandas con posición a 1517±2 (A) cm^{-1} y 1548±4 (E_1) cm^{-1}. Dos de los polipéptidos, la poli-lisina y el poli-(glutamato) (excluidos del promedio), muestran posiciones en la amida I un tanto excepcionales cuando adoptan esta conformación en películas húmedas, 1645 y 1637 cm^{-1} respectivamente (los máximos de la amida II son normales). En películas secas o semihúmedas los máximos son más normales, pues se dan a 1655 y 1645 cm^{-1} respectivamente. Además, para el poli-(ácido glutámico) en conformación hélice alfa la amida I aparece a 1651 cm^{-1}. Todas estas observaciones apuntan a que la causa de valores de frecuencia en la amida I tan bajos para la poli-lisina y poli-glutamato se deben a su gran cantidad de cadenas laterales cargadas, que causa que interaccionen fuertemente con el agua. Los puentes de hidrógeno extras que se formarían con el C=O del enlace peptídico serían la causa de esta amida I anómala. Además, la repulsión entre las cadenas laterales puede afectar a la estabilidad de las hélices. Chirgadze et al. (1976) han mostrado que al disminuir la estabilidad de una hélice alfa (aumentando las cargas de las cadenas laterales mediante el pH) disminuye la frecuencia de la amida I. Por otra parte, estos polipéptidos muestran una amida II normal, coherente con esta interpretación.

Krimm y Bandekar (1986) recopilan que para el péptido poli-alanina en la conformación hélice alfa el máximo de la amida I se da a 1658 cm^{-1} (A), y en la amida II aparecen dos bandas a 1545 (E_1) y 1516 cm^{-1} (A), En Raman el máximo de la amida I aparece a 1655 cm^{-1} (E_1). Para la poli-alanina en D_2O, la amida I' aparece a 1650 cm^{-1} en IR (A), con un desplazamiento de –8 cm^{-1}, y a 1652 cm^{-1} en Raman (E_1), con un desplazamiento de –3 cm^{-1} (Krimm y Bandekar, 1986; Dwivedi y Krimm, 1984). Para la amida II' la banda más intensa en IR aparece a 1439 (E_1) cm^{-1} y una más débil a 1454 (A) cm^{-1} (Dwivedi y Krimm, 1984)

Para el péptido poli-(ácido glutámico) el máximo de la amida I lo encuentran en IR a 1653 cm^{-1} (A) y en Raman a 1652 cm^{-1} (E_1). En IR la amida II da dos bandas a 1550 y 1510 cm^{-1}. En D_2O el poli-(ácido glutámico) en conformación hélice alfa tiene un máximo en la amida I' a 1641 cm^{-1}, por lo tanto el intercambio H/D produce un desplazamiento en el máximo de la amida I de –10-12 cm^{-1} (Chirgadze et al., 1976; Susi et al., 1967). Para la poli-lisina en películas secas el desplazamiento se da desde 1645 cm^{-1} a 1638 cm^{-1}, y es de –7 cm^{-1} (Nevskaya y Chirgadze, 1976; Jackson et al., 1989).

Venyaminov y Kalnin (1990) estudiaron la absorción amida I y amida II de varios homopolipéptidos (poli-Ala, poli-Glu, poli-Lys) y proteínas fibrilares (*silk fibroin* y tropomiosina) en H_2O. Estos péptidos y

proteínas sirven como modelo para diversas estructuras, como hélices alfa infinitas, láminas beta antiparalelas infinitas y estructuras al azar. Los modelos para las hélices alfa infinitas mostraron las siguientes bandas. En la amida I una única banda centrada a 1647±3 cm^{-1}. En la amida II encontraron dos bandas, la primera representa el 75% del área y está centrada a 1551±3 cm^{-1}. La segunda banda representa el 25% del área, con máximo a 1520±3 cm^{-1}.

Marsh et al. (2000) estudiaron por polarización el homopéptido poli-glutamato, que forma hélices alfa. Experimentalmente obtiene las posiciones de las vibraciones A y E para la amida I y amida II en películas secas en H_2O. Para la amida I, el modo A aparece a 1657 cm^{-1} y el modo E a 1652 cm^{-1}, la separación es por lo tanto $\Delta\nu$ = 5 cm^{-1}. Se puede determinar que el modo A representa el 75% del área y el E el 25% para la amida I. Para la amida II, el modo A aparece a 1517 cm^{-1} y el modo E a 1549 cm^{-1}, la separación es por lo tanto $\Delta\nu$ = -32 cm^{-1}. El modo A representa el 16% del área y la E el 84% de la amida II.

La melitina es un péptido de 26 aminoácidos que forma parte del veneno de las abejas. Adopta una conformación hélice alfa. En H_2O, tanto en disolución como en DMPC, muestra un máximo en la amida I a 1653-1652 cm^{-1} (amida II a 1546 cm^{-1}) En D_2O, donde la ausencia de amida II es total (intercambio completo), el máximo de la amida I' se da a 1643 cm^{-1} (amida II' a 1458 cm^{-1}) correspondiendo a un desplazamiento de –10 cm^{-1} con la deuteración (Lavialle et al., 1982). En Raman, la amida I muestra en disolución un máximo a 1652 cm^{-1} (Bussian y Sander, 1989).

Zhang et al. (1992) estudiaron un péptido formado por una serie de leucinas con una lisina en cada extremo, lo cuales se consideran un buen modelo para hélices alfa transmembrana. Este péptido se acomoda bien a una bicapa lipídica en fase cristal líquido cuando el número de leucinas es de 24, L_{24}. En estas condiciones el máximo en la amida I aparece a 1655 cm^{-1}. Al inducir el cambio de fase un lípido de cristal líquido a fase gel el grosor de la bicapa aumenta. Al realizar este cambio de fase en presencia del polipéptido L_{24} su máximo en la amida I se desplaza de 1655 a 1658 cm^{-1}. Se concluye que el aumento del grosor de la bicapa estirará las hélices, aumentando la distancia del puente de hidrógeno $i \rightarrow i+4$ de las hélices (y como consecuencia debilitándolo). Esto producirá un aumento del número de onda de las hélices.

6.2.2. Hélices 3_{10}

El polipéptido poli-aminoisobutírico forma hélices 3_{10}. En películas con H_2O da un máximo en la amida I a 1656 cm^{-1} y en películas con D_2O a 1640 cm^{-1} (Dwivedi et al., 1984). Por lo tanto sufre un corrimiento de 16 cm^{-1} en la deuteración, mayor del habitualmente encontrado en hélices alfa. La amida II muestra un máximo a 1545 cm^{-1} y la amida II' a 1472 cm^{-1}.

El péptido alameticina (un antibiótico hidrofóbico de 19 aminoácidos) adopta predominantemente una estructura hélice alfa, pero con importantes segmentos en hélice 3_{10}, según la estructura cristalográfica de rayos-X (cristales obtenidos a partir de disolvente orgánico). Este péptido es rico en el aminoácido isobutírico (Aib), del que posee 8 residuos. El espectro de IR muestra en la amida I dos bandas a 1662 y

1640 cm^{-1}, y en la amida II una banda a 1545 cm^{-1}. Los estudios teóricos apuntan que la banda a 1662 correspondería a segmentos 3_{10}, pero experimentos realizados en proteínas concuerdan más con asignar a hélices 3_{10} la banda a 1640 cm^{-1} (Haris y Chapman, 1995).

Miick et al. (1992) comentan que las principales técnicas para determinar la estructura de péptidos cortos (RMN y DC) no son generalmente capaces de distinguir una hélice alfa y una 3_{10}. Para un péptido de 16 aminoácidos basado en la alanina, determinan mediante experimentos de resonancia electrónica de *spin* una estructura coherente con una hélice 3_{10}. Experimentos de IR en D_2O muestran una amida I' con un máximo a 1637 cm^{-1}, una posición no habitual para una hélice alfa deuterada, y la asignan a hélices 3_{10}.

Sin embargo, estudios posteriores de Martinez y Millhauser (1995) relativizan este hallazgo, pues otros péptidos de 21-16 aminoácidos basados en la alanina que adoptan una estructura totalmente o mayoritariamente hélice alfa muestran una amida I' a 1634-1632 cm^{-1}. Esto autores concluyen que no es posible diferenciar hélices alfa y 3_{10} por su máximo en la amida I'. Los autores consideran que para estos péptidos pequeños la interacción con el disolvente para aminoácidos estructurados es mucho mayor de lo normal, causando para hélices alfa un desplazamiento a números de onda menores de los valores habituales de la amida I'. Esta explicación ha sido utilizada para explicar el bajo número de onda de absorción de la poli-lisina y poli-glutamato en películas húmedas cuando adoptan esta conformación (amida I a 1645 y 1637 cm^{-1} mientras que el valor medio en polipéptidos en de 1654 cm^{-1}).

6.2.3. Láminas beta antiparalelas

Chirgadze y Neuskaya (1976a) recopilaron los resultados obtenidos para la amida I de un grupo de 28 modelos experimentales que adoptan láminas beta antiparalelas (casi infinitas), que incluye polipéptidos, homopéptidos y proteínas fibrilares. Se observan siempre dos bandas, con posiciones medias de 1696±5 cm^{-1} y 1629±5 cm^{-1}.

Krimm y Bandekar (1986) recopilan los siguientes resultados experimentales. El espectro experimental de la poli-Ala (láminas beta antiparalelas planas) muestra bandas a 1632 cm^{-1} (muy intensa) y 1694 cm^{-1} (débil) para la amida I ($\Delta\nu = 62$ cm^{-1}). Para la amida II a 1555 cm^{-1} (media-débil) y a 1524 cm^{-1} (intensa) ($\Delta\nu = -31$ cm^{-1}). Para la poli-Ala-Gly (láminas beta antiparalelas planas) se observan bandas en la amida I a 1636 cm^{-1} (muy intensa), 1693 cm^{-1} (débil) y 1702 cm^{-1} (débil). En la poli-Gly (que adopta una estructura lámina beta antiparalela ondulada) se observan bandas en la amida I a 1636 cm^{-1} (intensa) y 1685 cm^{-1} (media) ($\Delta\nu = 49$ cm^{-1}), y en la amida II a 1517 cm^{-1} (intensa).

Venyaminov y Kalnin (1990) estudiaron la absorción amida I y amida II de varios homopéptidos (poli-Ala, poli-Glu, poli-Lys) y proteínas fibrilares (silk fibroin y tropomiosina) en H_2O. Estos péptidos y proteínas sirven como modelo para diversas estructuras. Los modelos para las láminas beta antiparalelas infinitas mostraron las siguientes bandas. En la amida I aparecen dos bandas. La banda más intensa (90% del área) aparece a 1619±6 cm^{-1}. La segunda banda (10% del área) aparece sobre 1695±6 cm^{-1} y es más

estrecha. Para la amida II también aparecen dos bandas. La más intensa, que representa un 85% del área, aparece sobre 1533±4 cm^{-1}. La banda de menor intensidad aparece a 1563±3 cm^{-1}.

Se observó que para la poli-alanina en la sustitución del N-H amida por N-D, las bandas amida sufren una reducción de su frecuencia de vibración de unos 5 cm^{-1} (Krimm y Bandekar, 1986). La poli-Lys, en su conformación que da láminas beta antiparalelas, muestra un máximo en H_2O para la amida I a 1616 y 1690 cm^{-1}, y el D_2O a 1611 y 1680 cm^{-1} (amida I'), con un desplazamiento de –5 y –10 cm^{-1} respectivamente (Susi et al. 1967).

6.2.4. Láminas beta paralelas

Existen pocos péptidos que adopten esta conformación. Uno de ellos es el tripéptido Val-Gly-Gly. Muestra un máximo en la amida I para IR a 1645 cm^{-1} y en Raman a 1657 cm^{-1}. En la amida II el máximo se observa a 1543 cm^{-1} (Bandekar y Krimm, 1988).

6.2.5. Estructuras al azar

El poli-Glu en su conformación que adopta una estructura al azar, muestra un máximo en películas secas en H_2O a 1657 cm^{-1} y en D_2O a 1643 cm^{-1} ($\Delta\nu$ = -14 cm^{-1}) (Susi et al. 1967). Chirgadze et al. (1976) obtuvo para el poli-glutamato en conformación al azar una amida I a 1652 cm^{-1} (película seca) y una amida I' a 1646 cm^{-1} ($\Delta\nu$ = -6 cm^{-1}). La proteína *silk fibroin* en conformación al azar muestra una amida I a 1656 cm^{-1} (película seca) y una amida I' a 1650 cm^{-1} ($\Delta\nu$ = -6 cm^{-1})

Venyaminov y Kalnin (1990) estudiaron la absorción amida I y amida II de varios homopéptidos y proteínas fibrilares en H_2O como modelo para diversas estructuras. Los modelos para una estructura al azar dan una única banda en la amida I y otra en la amida II. La banda en la amida I aparece sobre 1651±2 cm^{-1}. En la amida II la banda aparece a 1550±3 cm^{-1}.

6.2.6 Giros reversos

Krimm y Bandekar (1986) recopilaron experimentos de IR y Raman realizados con pequeños péptidos que forma giros reversos: Gly-Pro-Leu-gly; Pro-Leu-Gly; Gly-Pro-Gly-Gly; ciclo(Ala-Gly-Aca); Phe-Pro-Gly-Ala-Pro. En total recopilan los resultados de cuatro péptidos que forma giros β y de uno que forma giros γ.

Para todos los giros β la amida I muestra bandas desde 1690 a 1640 cm^{-1}. Se observan las mismas bandas y con el mismo número de onda en IR que en Raman, con intensidades relativas semejantes pero no iguales. En la amida II se observan bandas sólo en IR, desde 1570 a 1535 cm^{-1}.

El péptido que forma un giro γ muestra una amida I con bandas asociadas al giro desde 1690 a 1660 cm^{-1}. Se observan las mismas bandas y con el mismo número de onda en IR y en Raman.

6.3. Estudios experimentales con proteínas de estructura conocida

Existen tres tipos de estudios de proteínas de estructura conocida que nos dan información para la asignación de bandas. Los más sencillos de estos estudios se basan es determinar los máximos en la amida I y amida II de proteínas en las que prevalece un tipo de estructura. Otro tipo de estudios se basa en la desconvolución de la amida I, amida I' o amida I-I' (supone un intercambio incompleto H/D) de una proteína y un posterior ajuste de bandas. Las bandas se asignan buscando la concordancia de los resultados de IR con los resultados cristalográficos o de otras espectroscopias. El último tipo de estudios se basa en la determinación de los espectros de estructuras secundarias puras, por técnicas relacionadas con reconocimiento de patrones. Suponen que los espectros de proteínas son el resultado de la combinación lineal de espectros de estructuras puras, que a su vez son constantes para todas las proteínas. Para un grupo de proteínas de estructura conocida se determinan los porcentajes de diferentes estructuras, y a partir de sus espectros de IR es posible (en la medida que todas estas suposiciones son correctas) obtener los espectros de diferentes tipos de estructuras en proteínas.

Antes de continuar, es importante poner atención sobre el problema de observar la amida I' en proteínas. En general, en los estudios realizados para proteínas en D_2O, sólo se conseguirá un intercambio parcial, y por lo tanto observaremos la amida I-I'. Hablaremos de amida I' cuando el intercambio es completo.

6.3.1 Máximos de proteínas con estructuras mayoritarias

6.3.1.1. Hélices alfa

Normalmente para proteínas solubles con alto contenido en hélices alfa el máximo de la amida I aparece entre 1655 y 1650 cm^{-1} (Haris y Chapman, 1996). La mioglobina, proteína globular que contiene un ≈75% de hélices alfa, muestra un máximo en la amida I a 1654-1652 cm^{-1} y en la amida II a 1548-1540 cm^{-1} (Susi et al., 1967; Dousseau y Pézolet, 1990; Goormaghtigh et al., 1994). La hemoglobina, con un ≈75% de hélices alfa muestra un máximo en la amida I a 1654 cm^{-1} (Sarver & Krueger, 1991; Dong et al., 1990). La triosa fosfato isomerasa (≈45% hélices) muestra un máximo a 1651 cm^{-1} (Sarver & Krueger, 1991).

En D_2O, la mioglobina muestra un máximo a 1650 cm^{-1}, con un desplazamiento de –2-4 cm^{-1} respecto al máximo en H_2O (Susi et al., 1967; Goormaghtigh et al., 1994). La posición del máximo de la mioglobina en D_2O es mayor de lo observado en polipéptidos deuterados y el desplazamiento que sufre con la deuteración es bastante menor. Sin embargo, estos valores son bastante comunes para las hélices de las proteínas en D_2O (Goormaghtigh et al., 1994). Este hecho podría deberse a una protección de las hélices respecto al intercambio, pues las hélices son estructuras que pueden ser resistentes al intercambio. El trabajo de Jackson et al. (1991) apoya esta interpretación.

Jackson et al. (1991) estudiaron la parvalbumina, la cual se compone en casi un 70% de hélices alfa. El principal motivo de estas proteínas es el motivo hélice-lazo-hélice, con las hélices consecutivas dispuestas de manera casi perpendicular. En este motivo las hélices se encuentran bastante expuestas al disolvente. En H_2O el máximo de la amida I se da a 1654 cm^{-1} (amida II a 1550 cm^{-1}), un valor típico para hélices alfa de proteínas globulares, pero tras 24 horas en D_2O el máximo de la amida I' aparece a 1644 cm^{-1} (la amida II está completamente ausente), un valor inusual para hélices alfa de proteínas en D_2O. Tras 15 minutos en contacto con D_2O el máximo se da a 1649 cm^{-1}, y hay presencia de amida II'. En presencia de Ca^{2+}, que es un ligando de éstas proteínas y aumenta su estabilidad térmica, el máximo en D_2O tras 24 horas se da a 1647 cm^{-1} y se observa cierta presencia de amida II. Estos resultados llevan a pensar que esta posición inusual para hélices alfa de proteínas en D_2O se debe al intercambio completo de éstas, que produce un desplazamiento de –10 cm^{-1} (similar al obtenido en homopolipéptidos). La estabilización por Ca^{2+} produce cierta protección ante el intercambio, con lo que el desplazamiento se reduce a –7 cm^{-1}. Hélices más estabilizadas mostrarán un desplazamiento menor aún.

Respecto a los resultados obtenidos en Raman, los cuales son interesantes para localizar el modo E de las hélices alfa, la hemeritrina (≈80% hélices alfa), muestra un máximo a 1653 cm^{-1}, y la proteína que une calcio (≈70% hélices alfa) muestra un máximo a 1655 cm^{-1} (Bussian & Sander, 1989).

Finalmente, las proteínas de membrana con un supuesto o demostrado alto contenido en hélices alfa, como la rodopsina, el citocromo c oxidasa, la H^+/K^+ ATPasa, la Na^+/K^+ ATPasa, la Ca^{2+} ATPasa, el transportador de glucosa, el transportador de melibiosa y el centro fotosintético, muestran un máximo para la amida I entre 1658 y 1656 cm^{-1} (Haris y Chapman 1989, 1992; Alvarez et al., 1989; Dave et al., 2000). Hay una proteína de membrana con un máximo fuera de este rango: la bacteriorodopsina, con un máximo en la amida I a 1662 cm^{-1}. Este máximo anómalo para la bacteriorodopsina se suele justificar por la presencia de hélices α_{II}. Este máximo es muy sensible a las condiciones de la proteína, pues cuando se pierden las interacciones proteínas-proteína (en estado nativo forma trímeros) su máximo en la amida I aparece a 1658 cm^{-1}, una posición más habitual para proteína de membrana (Torres et al., 1995).

6.3.1.2. Láminas beta

La concanavalina A, una proteína globular con ≈65% de láminas beta antiparalelas, muestra un máximo en la amida I a 1638-1635 cm^{-1}, y en la amida II a 1537-1532 cm^{-1} (Dousseau y Pézolet, 1990; Goormaghtigh et al., 1994; Dong et al., 1990). La inmunoglobulina G, ≈65% láminas beta, muestra un máximo en la amida I a 1640-1638 cm^{-1} (Sarver y Krueger, 1991)

El α-chimotripsinógeno posee un ≈50% de láminas beta (Dousseau y Pézolet, 1990) y tiene el máximo de la amida I a 1638 cm^{-1} y el de la amida II a 1527 cm^{-1} (Goormaghtigh et al., 1994). En D_2O el máximo de la amida I-I' aparece a 1634,5 cm^{-1} (desplazamiento –3,5 cm^{-1}) pero el intercambio no está totalmente completado, tal como se deduce por la presencia de amida II (Goormaghtigh et al., 1994).

La proteína de membrana porina, tiene como principal motivo estructural barriles beta, que se forman con láminas beta antiparalelas (Tamm & Tatulian, 1997). Muestra una amida I con máximo a 1628 cm^{-1}, y una amida II con máximo a 1530 cm^{-1} (Goormaghtigh et al., 1994; Haris y Chapman 1989, 1992)

6.3.1.3. Estructuras al azar

La α-caseína, una proteína carente de estructura (al azar), muestra un máximo en H_2O a 1655 cm^{-1} para la amida I y a 1551 cm^{-1} para la amida II. En D_2O la amida I' aparece a 1643 cm^{-1}, con un desplazamiento de –12 cm^{-1} (Susi et al., 1967; Susi y Byler 1986).

Surewiz y Mantsch (1987) al desnaturalizar térmicamente la azurina y la apoazurina en D_2O observan que la amida I' pierde todo detalle, incluso en espectros desconvulados, y la amida II desaparece totalmente. La amida I' muestra una única banda ancha con un máximo entre 1644 y 1640 cm^{-1}. Correspondería a una estructura completamente desordenada, o al azar.

La desnaturalización térmica de la Ribonucleasa T_1 también genera en la amida I' una banda ancha y sin detalle (asignada a estructura al azar), centrada a 1647 cm^{-1} (Fabian et al. 1994).

6.3.1.4. Estructuras irregulares

La ferrodoxina en una proteína estructurada, pero la mayor parte de sus aminoácidos, el ≈45%, adoptan estructuras que no corresponden ni a hélices (≈15%) ni a láminas (≈15%) ni a giros (≈25%), y son por lo tanto estructuras irregulares. Su amida I muestra un máximo a 1646 cm^{-1}. La azurina, el inhibidor de tripsina y la papaína muestran un 25-30% de otras estructuras, y porcentajes variables de hélices (10-25%), láminas (20-30%) y giros (25-35%), mostrando el máximo de la amida I entre 1650 y 1643 cm^{-1} (Sarver y Krueger, 1991).

La papaína, con un 30% de sus aminoácidos adoptando otras estructuras, muestra en H_2O un máximo a 1650 cm^{-1} y en D_2O (el intercambio no es completo), a 1645 cm^{-1} (Eckert et al., 1977).

6.3.2. Espectros de estructuras puras obtenidos por reconocimiento de patrones

Se han realizado numerosos estudios. Todos ellos están dirigidos a la predicción de estructura secundaria, pero en una parte de ellos también se ha calculado los espectros propios para diferentes tipos de estructuras. Estos espectros nos interesan para asignar bandas, ya que se obtienen sin utilizar ninguna idea preconcebida derivada de los estudios teóricos o con polipéptidos. A continuación repasaremos varios trabajos y sus resultados. En todos ellos, las proteínas utilizadas son globulares y, por lo tanto, los espectros propios determinados corresponden a la contribución en los espectros de IR de ciertas estructuras en proteínas (o dominios) globulares.

Eckert et al. (1977) obtuvieron los espectros de IR de ocho proteínas en D_2O, con valores de estructura secundaria conocidas. Obtuvieron los espectros propios de las hélices alfa, las láminas beta y del resto de

las estructuras. El nivel medio de intercambio determinado fue menor del 80%.* Al no poder asegurar un intercambio completo los datos corresponden a la amida I-I'. El espectro de las hélices alfa se compone de una banda con máximo a 1652 cm^{-1}; el de las láminas beta se compone de una banda principal a 1634 cm^{-1} y dos bandas/hombros menores a 1660 y 1680 cm^{-1}. Para el resto de las estructuras (giros y estructuras no ordenadas) el espectro se compone de una banda centrada a 1645 cm^{-1}.

Dousseau y Pézolet (1990) estudiaron la zona amida I y amida II de los espectros de IR de trece proteínas solubles disueltas en H_2O, cuya estructura se conoce por cristalografía de rayos-X. Las estructuras obtenidas por rayos-X las separan en porcentajes de hélices alfa, láminas beta y otras estructuras. Este conjunto contiene proteínas con contribuciones muy variadas, desde la mioglobina (con ≈75% de hélices alfa) pasando por la concanavalina A (con ≈65% de láminas beta) hasta la papaína (≈45% de otras estructuras). El espectro de las hélices alfa muestran en la amida I una banda simétrica centrada a 1653 cm^{-1}, y en la amida II a 1548 cm^{-1}. Para las láminas beta la banda de la amida I es asimétrica. El máximo se da a 1637 cm^{-1} pero otras dos contribuciones de menor intensidad aparecen sobre 1663 y 1684 cm^{-1} causando la asimetría. En la amida II el máximo se da a 1543 cm^{-1}. El resto de las estructuras (que principalmente serán giros reversos y estructuras irregulares) dan en la amida I y amida II una contribución que se extiende desde 1700 a 1500 cm^{-1}. En la amida I se centra entre 1690-1640 cm^{-1}, con máximos a 1670 y 1660 cm^{-1}. En la amida II la contribución se centra entre 1580-1530 cm^{-1}, con máximo a 1560 cm^{-1}.

En un trabajo similar Lee et al. (1990) obtuvieron espectros de IR en H_2O para 18 proteínas solubles, con estructura conocida por difracción de rayos-X. Los espectros derivados para las estructuras hélices alfa, láminas beta y giros reversos para la amida I (no los muestran) tienen los siguientes componentes: para las hélices alfa 1695, 1659 (el más intenso) y 1641 cm^{-1}, para las láminas beta 1682 y 1634 cm^{-1} (el más intenso) y para los giros reversos 1684 (el más intenso), 1654 y 1633 cm^{-1}.

Kalnin et al. (1990) obtuvieron espectro de IR en H_2O para 13 proteínas y 3 polipéptidos (solubles) de estructuras de rayos-X conocida. Utilizando estos espectros, así como los que Venyaminov y Kalnin (1990) habían derivado para las estructuras láminas beta antiparalelas, hélices alfa y estructuras al azar, son capaces de obtener los espectros puros de una serie de estructuras secundarias: hélices y láminas beta ordenadas y desordenadas, giros reversos y otros. Las estructuras hélices desordenadas corresponden a los extremos de estas estructuras en proteínas. Las láminas beta desordenadas corresponden a aminoácidos que se encuentran formando esta estructura pero con un patrón de puentes de hidrógeno no clásico. Las hélices ordenadas dan en la amida I una banda principal a 1652 cm^{-1} y un hombro sobre 1630 cm^{-1}, y en la amida II una banda a 1547 cm^{-1}. La contribución de las hélices desordenadas tiene la forma de una primera derivada de una banda. En la amida I muestra un máximo a 1663 y un mínimo a 1630 cm^{-1}. Su

* Al no restar la contribución de las cadenas laterales de los aminoácidos deuterados, el nivel de intercambio se sobreestima, por lo que el real será menor del 60-70%.

efecto es aumentar la posición del máximo de la amida I de las hélices a medida que la proporción de hélices desordenadas respecto a las ordenadas aumenta (desde 1652 a 1663 cm^{-1}). En la amida II ocurre algo parecido y el desplazamiento se da desde 1547 a 1540 cm^{-1}. La contribución de las láminas beta ordenadas corresponde a dos bandas claras en la amida I, una ancha e intensa a 1637 cm^{-1} y otra débil y estrecha a 1695 cm^{-1}. Aparte de estas dos bandas, aparecen otras dos bandas menos claras sobre 1660 y 1620 cm^{-1} de intensidad menor que la banda a 1637 cm^{-1}. En la amida II el máximo se da a 1527 cm^{-1}. Las láminas beta desordenadas muestran dos bandas y un hombro en la amida I. La banda más intensa se da a 1632 cm^{-1}, la banda de menor intensidad (y más estrecha) se da a 1688 cm^{-1}, y el hombro a 1643 cm^{-1}. En la amida II aparecen dos bandas anchas con un alto grado de solapamiento entre ellas, situadas a 1567 y 1555 cm^{-1}. Los giros reversos dan una amida I con forma de dos bandas muy solapadas con máximos a 1670 y 1660 cm^{-1}, que se extiende desde 1690 a 1630 cm^{-1}. Su amida II aparece centrada a 1545 cm^{-1}. Las estructuras denominadas otras estructuras (corresponderán principalmente a estructuras irregulares), muestran en la amida I una banda asimétrica centrada a 1639 cm^{-1}, que se extiende principalmente hacia números de onda mayores. En la amida II aparecen dos bandas a 1560 y 1520 cm^{-1}.

Saber y Kruger (1991) adquirieron espectros de IR en H_2O para diecisiete proteínas solubles y analizaron la zona de la amida I. Obtuvieron la contribución en la amida I de las estructuras hélices (incluye alfa, 3_{10} y π), láminas beta, giros reversos y otras estructuras. Para las hélices aparece una banda simétrica centrada a 1652 cm^{-1}. La contribución de las láminas beta se compone de una banda principal (a 1636 cm^{-1}) y otra banda secundaria de mucha menor intensidad (1685-1660 cm^{-1}). Los giros reversos dan dos bandas. La más intensa aparece entre 1700-1650 cm^{-1}, centrada a 1670 cm^{-1}. La de menor intensidad se extiende de 1650-1600 cm^{-1}, centrada a 1630 cm^{-1}. Finalmente el resto de las estructuras da una banda relativamente simétrica centrada a 1642 cm^{-1}.

Príbic et al. (1993) analizaron el espectro de IR obtenido en H_2O de 21 proteínas solubles de estructura conocida por rayos-X. Obtuvieron los espectros propios para la amida I de las estructuras hélices, láminas beta paralelas, láminas beta antiparalelas, giros reversos y otros. La contribución de las hélices muestra un máximo a 1655 cm^{-1}, la de las láminas beta paralelas a 1639 cm^{-1}, la de las antiparalelas a 1634 cm^{-1}, la de los giros a 1658 cm^{-1} y la del resto de las estructuras a 1637 cm^{-1}.

Sane et al. (1999) estudiaron 19 proteínas solubles por Raman en H_2O. Obtuvieron los espectros puros de algunas conformaciones. Así, la hélice ordenada da un máximo en la amida I a 1655 cm^{-1}. Las hélices desordenadas y láminas beta dan dos contribuciones, una intensa a 1670 cm^{-1} (75% del área) y otra débil a 1650 cm^{-1} (25% del área). Los giros dan dos contribuciones. La primera, que representa un 75% del área, se da entre 1710-1670 cm^{-1}, centrada a 1685 cm^{-1}. La segunda, que representa el 25% del área, aparece entre 1660-1645 cm^{-1}, centrada a 1655 cm^{-1}. El resto de las estructuras también dan dos contribuciones principales. La primera (70% del área) se extiende entre 1650-1625 cm^{-1}, centrada sobre 1640 cm^{-1}, y la segunda (30% del área) aparece entre 1680-1660 cm^{-1}, centrada a 1665 cm^{-1}. Recordemos que para láminas beta antiparalelas y paralelas el modo más activo en Raman es el A, que se predice entre 1680-

1660 cm^{-1} (según el tipo de lámina). Recordemos también que en Raman el modo más activo para hélices alfa es el E_1.

6.3.3. Desconvolución y ajuste

En esta fuente de asignación de bandas podemos diferenciar dos tipos de trabajos. El primero de ellos es el que se basa en desconvular y ajustar cierto número representativo de proteínas de estructura conocida. Se definen intervalos para asignar las bandas ajustadas de tal manera que se logre una buena concordancia entre la estimación secundaria obtenida por IR y la que se deriva de la estructura tridimensional. El segundo tipo de trabajo se realiza sobre alguna proteína con alguna estructura no estándar o poco común, o que sufre algún cambio conformacional que afecta a un tipo de estructura concreta. Normalmente se intenta relacionar esta estructura con alguna de las bandas ajustadas. Los métodos de reconocimiento de patrones son incapaces de funcionar en estos casos si esta estructura no es compartida con otras muchas más proteínas, pues sólo son capaces de identificar contribuciones de estructuras comunes, y las contribuciones singulares son ignoradas.

6.3.3.1. Intervalos de asignación para estructuras comunes

Byler y Susi (1986) obtuvieron espectros en disolución de D_2O para 21 proteínas globulares. Equilibran las proteínas en D_2O hasta que la amida II haya desaparecido, hasta un máximo de 24 horas. Desconvulan los espectros con $\gamma' = 13$ cm^{-1} y $k = 2{,}4$. Ajustan el espectro desconvulado con bandas Gausianas incluyendo una línea base entre 1700 y 1600 cm^{-1}. El número de bandas y posiciones se obtienen a partir de la segunda derivada del espectro original. Si durante el ajuste se cree necesario, se añade alguna otra banda. Para la mayoría de los ajustes acaban utilizando nueve bandas en la amida I-I'. Realizan las siguientes asignaciones: 1640-1620 cm^{-1} y 1680-1670 cm^{-1} láminas beta, 1658-1650 cm^{-1} hélices alfa, 1700-1680 cm^{-1} y 1670-1659 cm^{-1} giros reversos, y 1648-1640 cm^{-1} estructuras desordenadas. Con estas asignaciones obtienen una predicción para hélices alfa y láminas beta con un error estándar del 2-3%, extraordinariamente pequeño. Posteriormente Susi y Byler (1987) desconvularon y ajustaron espectros obtenidos en D_2O de cuatro proteínas ricas en láminas beta, con presencia variable de láminas beta paralelas y antiparalelas. Concluyen que las láminas beta paralelas y antiparalelas comparten el mismo intervalo de asignación, y son por lo tanto no distinguibles por IR.

Goormaghtigh et al. (1990) realizaron un estudio con catorce proteínas globulares de estructura conocida difracción de rayos-X y tres proteínas de membrana para las que existe una estimación de estructura secundaria por otras técnicas. Prepararon películas secas sobre un cristal de RTA, pusieron la muestra en contacto con una atmósfera saturada de D_2O durante cuatro horas, volvieron a secar y a continuación adquirieron el espectro. Asumen que principalmente sólo las estructuras desordenadas se intercambian, desplazándose de $\approx$ 1655 cm^{-1} a $\approx$ 1640 cm^{-1}. Los espectros los desconvulan con $\gamma' = 30$ cm^{-1} y un filtro Gausiano. Antes del ajuste de bandas realizaron una corrección de línea base entre 1700 y 1600 cm^{-1}. El ajuste se realiza con bandas Lorentzianas y una línea base sin pendiente. El primer ajuste se

realiza sobre un espectro desconvulado con k = 2-2,8, utilizando diez bandas Lorentzianas en la zona de la amida I-I' con posiciones iniciales que se repiten en espectros desconvulados de varias proteínas (1695, 1683, 1678, 1672, 1664, 1657, 1648, 1640, 1632 y 1624 cm^{-1}). El ajuste se vuelve a realizar en espectros desconvulados con una k menor, hasta ajustar un espectro con k = 1.* En estos nuevos ajustes utilizan los parámetros obtenidos en el ajuste anterior, excepto para la posición, para la que se reinicia su valor. Los rangos de asignación de bandas son: 1662-1645 cm^{-1} hélices alfa, 1689-1682 cm^{-1} y 1637-1613 cm^{-1} láminas beta, 1644,5-1637 cm^{-1} estructuras al azar, y 1682-1662,5 cm^{-1} giros beta. Con esta asignación obtienen una predicción para hélices alfa y láminas beta con un error estándar del 9%.

Kumosinski y Unruh (1996) estudiaron, en H_2O, 14 proteínas globulares y dos polipéptidos sintéticos de estructura conocida por rayos X. Desconvularon los espectros con γ' = 9 cm^{-1} y k = 2,3, y los ajustaron desde 1700 a 1500 cm^{-1} (la amida I y amida II) con bandas Lorentzianas/Gausianas mezcladas. El número de bandas utilizadas en el ajuste se decide mediante el criterio estadístico de la F de Fisher, y normalmente se utiliza un máximo de 28 bandas. Los resultados obtenidos los utilizan para realizar un ajuste en el espectro original. Tanto en el ajuste del espectro desconvulado, como en el original, obtienen que las bandas ajustadas sólo tienen carácter Gausiano. Realizan las siguientes asignaciones: 1660-1650 cm^{-1} hélices alfa, 1648-1642 cm^{-1} estructuras desordenadas o irregulares, 1638-1624 cm^{-1} láminas beta o estructuras extendidas y 1695-1670 cm^{-1} giros. Con estas asignaciones las estructuras secundarias estimadas tienen un error medio de 3-4%.

La corrección de los intervalos utilizados en estos trabajos descansará en parte en el ajuste de bandas. Este proceso nunca ha sido realizo de manera estrictamente correcta lo cual puede generar dudas sobre los resultados obtenidos. Es, sin embargo, curioso, como tanto en trabajos realizados en H_2O o D_2O, donde los espectros son desconvulados con parámetros muy diferentes (y arbitrarios), donde generalmente se realiza una corrección de línea base entre los extremos del intervalo ajustado, y en los que se ajusta los espectros desconvulados con bandas erróneas y muy diferentes entre sí (Gausianas y Lorentzianas), todos los trabajos obtienen una buena estimación de la estructura secundaria y, además, utilizando unos intervalos de asignación muy semejantes. Teniendo en cuenta la sensibilidad del ajuste obtenido al modelo utilizado, este hecho es extremadamente sorprendente y para nosotros de difícil explicación. Un ejemplo más extremo se puede observar en el trabajo de Dong et al. (1990). Estudian 12 proteínas globulares en H_2O. Utilizan como intervalo de aparición de las hélices alfa 1664-1652 cm^{-1}, para estructuras al azar 1652-1645 cm^{-1}, para láminas beta 1645-1620 cm^{-1} y para giros 1690-1664 cm^{-1}. Calculan la segunda derivada del espectro, y hacen el cero en el valor más positivo. Para obtener la estimación de la estructura secundaria integran este espectro entre los intervalos de número de onda correspondientes. Obtienen un error en la estimación de estructura secundaria del 5%. Sin embargo, la relación que pueda tener la integral de la segunda derivada con una corrección de la línea base de una

* Suponen que la desconvolución introduce distorsiones y que estas distorsiones serán menores para k=1, pues consideran que el espectro estará menos desconvulado. Confunden desconvolución con estrechamiento.

banda, con su contribución en el área de un espectro, es realmente débil, y su uso para estimar su contribución sólo se sostiene porque aparentemente funciona, pues la estimación de estructura secundaria es correcta.

Finalmente, cabe comentar que con los años se ha ido acumulando en la literatura asignaciones de bandas realizadas sobre proteínas concretas (a veces de estructura de rayos X conocida, o de estructura secundaria estimada por otra técnica espectroscópica y a veces no). Goormaghtigh et al. (1994) realizaron una recopilación más o menos extensiva de estas asignaciones. La recopilación muestra que en H_2O se han asignado bandas a estructuras hélices alfa desde 1658 a 1648 cm^{-1} (excluida la bacteriorodopsina), a estructuras desordenadas entre 1658 y 1642 cm^{-1}, a láminas beta desde 1695-1674 cm^{-1} y 1641-1622 cm^{-1} y a giros reversos desde 1686 a 1662 cm^{-1}. Curiosamente las asignaciones utilizadas en la literatura para D_2O no parecen variar mucho, pues se han asignado bandas a estructuras hélices alfa desde 1660 a 1642 cm^{-1} (excluida la bacteriorodopsina), a estructuras desordenadas desde 1654 y 1639 cm^{-1}, a láminas beta desde 1694-1672 cm^{-1} y 1638-1615 cm^{-1} y a giros reversos desde 1692 a 1653 cm^{-1}

6.3.3.1. Intervalos de asignación para estructuras no comunes

Holloway y Mantsch (1989) estudiaron el dominio polar del citocromo b_5 en H_2O y D_2O. Su estructura se conoce por difracción de rayos-X, y muestra una inusual abundancia de estructura hélice 3_{10} (≈30%), y carece prácticamente de estructuras no ordenadas. En el espectro de IR en H_2O desconvulado aparece una banda a 1643 cm^{-1}, que representa el 35% del área de la amida I. Sumada con la banda asignada a hélices alfa (25%) tenemos que el 60% de la proteína se predice en hélices, en concordancia con el valor de 50% obtenido en CD. En D_2O se obtiene un espectro que al desconvularlo es prácticamente idéntico al de H_2O, pero desplazado 5 cm^{-1} a número de onda menores. Esto indica intercambio semejante para todas las estructuras, pero no completo, pues la presencia de amida II en D_2O, aunque pequeña, es evidente. La banda asignada a 3_{10} aparece a 1639 cm^{-1} (35% área).

Prestrelski et al. (1991b) obtuvieron espectros de IR de la tripsina bovina en D_2O. Esta proteína puede sufrir cambios de conformación en partes localizadas, sin efecto en la mayor parte de la proteína. Estos cambios están bien caracterizados. Estudiaron como repercuten los cambios conformacionales de la proteína en las bandas ajustadas de un espectro desconvulado. Un cambio que afecta a un lazo de la proteína hace decrecer una banda a 1655 cm^{-1}. Otros cambios que aumentan la proporción de segmentos desordenados aumentan el área y la anchura de una banda a 1645 cm^{-1}. Diferencian estructuras irregulares (no repetitivas) y desordenadas (móviles). Según ellos, ambas aparecen en D_2O a la misma frecuencia (1645 cm^{-1}) y sólo son distinguibles por que la segunda dará bandas más anchas.

Prestrelski et al. (1991a,c) realizaron un estudio de IR de la α-lactalbumina. Su estructura por rayos-X revela que contiene un ≈30% de hélices alfa y menos de ≈15% de estructuras no asignables a una estructura secundaria concreta. El espectro de la proteína, obtenido en D_2O, muestra tras su desconvolución dos bandas a 1659 cm^{-1} (≈15% del área) y 1651 cm^{-1} (≈25%). Estas dos bandas se

asignan dos tipos de hélice diferentes, y no a un posible intercambio incompleto H/D de una sola hélice, pues los autores estiman que el intercambio H/D es completo. Estas hélices tendrían una geometría diferente y/o mostrarían diferencias en la fuerza de sus puentes de hidrógeno. La α-lactalbumina contiene, además, un ≈30% de hélices 3_{10}, lo cual se correlaciona bien con la banda resuelta a 1639 cm^{-1} (≈30%).

Wilder et al. (1992) estudiaron por IR dos interleuquinas recombinantes (1α y 1β). Por CD no se detecta presencia de hélices. Además, la estructura de las interleuquinas 1α y 1β humanas se conoce por difracción de rayos X y RMN. Prácticamente carecen de hélices, y un ≈25% de los aminoácidos están implicados en lazos conectando láminas beta, las cuales representan el ≈55% de la estructura. Estas proteínas tienen una homología de secuencia del 80% con las estudiadas por IR. Por IR detectan, en D_2O, una banda a 1656 cm^{-1} que corresponde al ≈20 % del área, y la asignan a los lazos.

Tatulian et al. (1997) estudiaron una fosfolipasa libre en solución y unida a bicapas lipídicas. La forma en solución muestra una banda a 1651 cm^{-1}, asignada a hélices alfa. Cuando se une a una bicapa lipídica, aparece una banda adicional a 1658 cm^{-1}, que también se asigna a hélices alfa. Se concluye que en la unión a la membrana algunas de las hélices sufren una transformación en la que aumenta su flexibilidad y se debilitan los puentes de hidrógeno $i \rightarrow i+4$ de las hélices alfa. La presencia de dos tipos de hélices en proteínas ya había sido descrita por Prestrelski et al. (1991c). Más recientemente Dave et al. (2000), estudiando el transportador de melibiosa, asignaron dos bandas en la amida I a hélices transmembrana, con posiciones a 1660 y 1653 cm^{-1}.

Khurana y Fink (2000) estudiaron, en H_2O, tres proteínas que contienen láminas beta paralelas, concluyendo que esta estructura da una banda a 1640-1638 cm^{-1}. Dos de estas proteínas tienen muy pocas estructuras hélices, pero abundantes lazos conectando las láminas betas. Asignan bandas entre 1665-1660 cm^{-1} a estos lazos.

6.4. Resumen de los intervalos de asignación en la amida I

6.4.1. Hélices alfa

En IR esta estructura tiene dos modos activos, el A, orientado a lo largo de la hélice, y el E, orientado perpendicularmente a la hélice. El modo A, tres veces más intenso que el E, determina en la práctica la posición del máximo. Éste se suele dar entre 1660 y 1650 cm^{-1}.

Como la posición de las hélices alfa viene determinada por el modo A, es interesante conocer los factores que afectan su frecuencia. Así, se ha determinado que la posición del modo A aumenta al reducirse la longitud de la hélice, diminuye con la distorsión o irregularidades de las hélices,[*] aumenta al

[*] Consideramos una hélice distorsionada cuando los ángulos ϕ y φ del enlace peptídico varían aleatóriamente respecto a los valores estándares de residuo a residuo.

aumentar la longitud del puente de hidrógeno $i \rightarrow i+4$ (al pasar de α_I a α_{II} o por un estiramiento de la estructura) y se reduce cuando la hidratación de las hélices aumenta.

Respecto a la separación de los modos A y E, para hélices suficientemente largas ésta es menor de 4 cm^{-1}. Para hélices con la longitud encontradas en proteínas solubles los resultados teóricos apuntan hacia una separación próxima a 15 cm^{-1}, haciendo que el modo E aparezca alrededor de 1640 cm^{-1}. Esta predicción estaría apoyada por la observación de una banda sobre 1640 cm^{-1} en la mioglobina, que normalmente se ha asignado a láminas beta, a pesar de que la mioglobina carece de ellas. Sin embargo, en espectroscopia Raman, donde el modo más intenso es el E, el máximo de las hélices alfa en proteínas solubles se encuentra sobre 1655 cm^{-1}. Este hecho indica que la separación entre ambos modos es en la práctica nula.

Finalmente, tras una sustitución completa H/D las posiciones sufren un desplazamiento de entre –7 y -12 cm^{-1}. En la práctica la sustitución H/D será incompleta, observándose tanto la hélice hidrogenada como la deuterada. La separación entre ambas será insuficiente para resolverlas y aparentemente se observará una sola banda que sufre un desplazamiento menor del real. Si estas bandas se estrechan lo suficiente se podrán resolver ambas.

6.4.2. Hélices 3_{10}

Los resultados en H_2O son contradictorios. Se han observado y predicho hélices 3_{10} entre 1665-1655 cm^{-1}, pero también entre 1645-1640 cm^{-1}. Curiosamente, en D_2O todos los trabajos las sitúan entre 1640-1635 cm^{-1}.

6.4.3. Láminas beta

Las láminas beta antiparalelas tienen dos modos activos en IR.* El modo B_2 es perpendicular a la dirección de la cadena peptídica, y es unas diez veces más intenso que el modo B_1, con una dirección paralela a la cadena peptídica. Para láminas planas, el modo B_2 suele encontrarse entre 1635 y 1625 cm^{-1} y el B_1 entre 1700 y 1690 cm^{-1}. Para láminas onduladas el modo B_2 suele encontrase entre 1640 y 1635 cm^{-1} y el B_1 entre 1690 y 1685 cm^{-1}. La separación entre los modos B_1 y B_2 es algo mayor en láminas planas (≈ 65 cm^{-1}) que en onduladas (≈ 50 cm^{-1}). La longitud de las cadenas no afecta a esta separación, pero sí el número de cadenas. La hidratación de las láminas hace disminuir la frecuencia del modo B_2 y aumenta la separación entre B_1 y B_2. En Raman el modo más intenso es el A, que aparece entre 1670-1660 cm^{-1} para láminas planas, y alrededor de 1680 cm^{-1} en onduladas.

Las láminas beta paralelas tienen dos modos activos en IR, el A y el B. El modo B es más intenso, y se encuentra entre 1645-1640 cm^{-1}, mientras que el modo A, diez veces menor que el B, aparece entre 1665-1655 cm^{-1}. El modo A es, además, el más intenso en Raman.

* En realidad hay tres modos de vibración activos, pero uno de ellos es de intensidad muy débil.

Respecto a lo observado en proteínas globulares, las láminas beta antiparalelas tiene un máximo a ≈ 1634 cm^{-1}, mientras que las paralelas lo muestran a ≈ 1639 cm^{-1}. Esta diferencia es pequeña y por ello suelen estudiarse las dos en conjunto, sin intención de diferenciarlas. Así, en IR las láminas beta muestran varios máximos u hombros en la amida I. El más intenso se da entre 1637 y 1634 cm^{-1}, y los menores entre 1695-1680 cm^{-1} (correspondería al modo B_1 de láminas antiparalelas) y alrededor de 1660 cm^{-1} (correspondería al modo A de láminas paralelas). En los espectros desconvulados obtenidos en H_2O, se asignan bandas a esta estructura desde 1640 a 1620 cm^{-1} y desde 1695 a 1675 cm^{-1}.

Respecto al intercambio H/D, para las láminas beta antiparalelas se predice y observa en polipéptidos un corrimiento de –5 cm^{-1} para el modo B_2 y de –10 cm^{-1} para el B_1. Para proteínas los corrimientos aparentes pueden ser menores, a causa de un intercambio incompleto.

6.4.4. Giros reversos

Su contribución se extiende desde 1700 a 1640 cm^{-1}. En la práctica se pueden diferenciar dos zonas de máxima contribución. La más intensa, con un máximo entre 1685 y 1670 cm^{-1}, representa sobre el 70% del área, y el resto muestra un máximo entre 1660 y 1650 cm^{-1}. En algún trabajo se ha asignado cierta contribución sobre 1630 cm^{-1}. En D_2O su contribución más intensa se situará alrededor de 1665 cm^{-1}.

6.4.5. Estructuras al azar

Estas estructuras corresponden a segmentos que estrictamente no están estructurados, es decir, los enlaces peptídicos muestras valores de ϕ y φ que varían con el tiempo y entre enlaces contiguos de una manera al azar. Estos segmentos con tan gran dinamismo se caracterizan por ser *invisibles* por difracción de rayos X y RMN. En las estructuras transitorias que se forman, el C=O y el N-H del grupo amida interaccionará principalmente con el agua. En la clasificación en estructuras secundarias, las estructuras al azar se incluyen en el resto de las estructuras (ni hélices, ni láminas ni giros). En IR darán una banda ancha (más de 35 cm^{-1}) con forma principalmente Gausiana, situada entre 1658 y 1652 cm^{-1}. Serán las estructuras que sufran un intercambio H/D más rápido, tras el cual aparecerán entre 1650 y 1640 cm^{-1}.

6.4.6. Estructuras irregulares y lazos

Estas estructuras tienen un patrón de ángulos ϕ y φ constante con el tiempo, pero que varían entre enlaces contiguos de una manera irregular. Esta situación se dará habitualmente en la transición entre las estructuras secundarias regulares, correspondiendo a segmentos cortos necesarios para esta transición. Las estructuras irregulares no sufrirán necesariamente un intercambio H/D rápido, pues son estructuras estables y pueden estar escondidas del disolvente.

En la clasificación de estructuras secundarias las estructuras irregulares se incluyen en el resto de las estructuras (ni hélices, ni láminas ni giros), que incluirán por lo tanto estructuras al azar y estructuras irregulares. Podemos esperar que las irregulares sean las más abundantes de éstas. Esto concordaría con los resultados obtenidos por reconocimiento de patrones de proteínas en H_2O para el resto de las

estructuras, que se compone de una banda entre 1645 y 1637 cm^{-1} (recordemos que en H_2O las estructuras al azar tendrán un máximo entre 1658 y 1652 cm^{-1}).

Un tipo de estructura irregular especial que nos interesa son los lazos largos. Estos se pueden considerar estructuras irregulares. Tienen como peculiaridad su longitud, que hará que su conformación no esté condicionada por su función de unir segmentos. Se ha observado que los lazos contribuyen en H_2O entre 1665 y 1660 cm^{-1} y en D_2O alrededor de 1655 cm^{-1}. En algún trabajo se ha observado que el resto de las estructuras, además de una contribución principal sobre 1640 cm^{-1} en H_2O, muestran otra menor sobre 1665 cm^{-1}.

Referencias

Alvarez, J., Lee, D. C., Baldwin, S. A., and Chapman (1987) Fourier transform infrared spectroscopic study of the structure and conformational changes of the human erythrocyte glucose transporter. *J. Biol. Chem.* 262, 3502-3509

Bandekar, J. (1993) Amide modes of reverse turns. *V. Spectrosc.* 5, 143-173

Bandekar, J., and Krimm, S. (1988) Normal mode spectrum of the parallel-chain β-sheet. *Biopolymers*. 27, 909-921

Bussian, B. M., and Sander, C. (1989) How to determine protein secondary structure in solution by Raman spectroscopy: Practical guide and test case Dnase I. *Biochemistry* 28, 4271-4277

Byler, M., and Susi, H. (1986) Examination of the secondary structure of proteins by deconvolved FTIR spectra. *Biopolymers* 25, 469-487

Chirgadze, Yu. N., and Nevskaya, N. A. (1976a) Infrared spectra and resonance interaction of amide-I vibration of the antiparallel-chain pleated sheet. *Biopolymers* 15, 607-625

Chirgadze, Yu. N., and Nevskaya, N. A. (1976b) Infrared spectra and resonance interaction of amide-I vibration of the parallel-chain pleated sheet. *Biopolymers* 15, 627-636

Chirgadze, Yu, N., Brazhnikov, E. V., and Nevskaya, N. A. (1976) Intramolecular distortion of the α-helical structure of polypeptides. *J. Mol. Biol.* 102, 781-792

Dave, N., Troullier, A., Mus-Veteau, I., Duñach, M., Lablanc, G., and Padrós, E. (2000) Secondary structure components and properties of the melibiose permease from *Escherichia coli*: A Fourier transform infrared spectroscopy analysis. *Biophys. J.* 79, 747-755

Dong, A., Huang, P., and Caughey, W. S. (1990) Protein secondary structure in water from second-derivative amide I infrared spectra. *Biochemistry* 29, 3303-3308

Dousseau, F., and Pézolet, M. (1990) Determination of the secondary structure content of proteins in aqueous solutions from their amide I and amide II infrared bands. Comparison between classical and partial least-squares methods. *Biochemistry* 29, 8771-8779

Dwivedi, A. M., and Krimm, S. (1984) Vibrational analysis of peptides, polypeptides, and proteins. XVIII. Conformational sensitivity of the α-helix spectrum: α_I- and α_{II}-poly(L-alanine). *Biopolymers* 23, 923-943

Dwivedi, A. M., Krimm, S., and Malcolm, B. R. (1984) Vibrational analysis of peptides, polypeptides, and proteins. XVIII. Conformation of poly(α-aminoisobutyric acid). *Biopolymers* 23, 2025-2065

Eckert, K., Grosse, R., Malur, J., and Repke, K. R. H. (1977) Calculation and use of protein-derived conformation-related spectra for the estimate of the secondary structure of proteins from their infrared spectra. *Biopolymers* 16, 2549-2563

Fabian, H., Schultz, C., Backmann, J., Hahn, U., Saenger, W., Mantsch, H. H., and Naumann, D. (1994) Impact of point mutations on the structure and thermal stability of ribonuclease T1 in aqueous solution probed by Fourier transform infrared spectroscopy. *Biochemistry* 33, 10725-10730

Goormaghtigh, E., Cabiaux, V., and Ruysschaert, J-M. (1990) Secondary structure and dosage of soluble and membrane proteins by attenuated total reflection Fourier-transform infrared spectroscopy on hydrated films. *Eur. J. Biochem.* 193, 409-420

Goormaghtigh, E., Cabiaux, V. and Ruysschaert, J.-M. (1994) Determination of soluble and membrane protein structure by Fourier transform infrared spectroscopy. III. Secondary structures. *Subcell. Biochem.* 23, 405-450

Haris, P. I., and Chapman, D. (1989) Membrane protein conformation as determined by Fourier transform-infrared spectroscopy. *Biochem. Soc. Trans.* 17, 161-162

Haris, P. I., and Chapman, D. (1992) Does Fourier-transform infrared spectroscopy provide useful information on protein structures? *TIBS* 17, 328-333

Haris, P. I., and Chapman, D. (1995) The conformational analysis of peptides using Fourier transform IR spectroscopy. *Biopolymers* 37, 251-263

Haris, P. I., and Chapman, D. (1996) Fourier transform infrared spectroscopic studies of biomembrane systems. *In* Infrared spectroscopy of Biomolecules. Wiley-Liss. 239-278

Holloway, P. W., and Mantsch, H. H. (1989) Structure of cytochrome b_5 in solution by Fourier-transform infrared spectroscopy. *Biochemistry* 28, 931-935

Jackson, M., Haris, P. I., and Chapman, D. (1989) Conformational transitions in poly(L-lysine): studies using Fourier transform infrared spectroscopy. *Biochim. Biphys. Acta.* 998, 75-79

Jackson, M., Haris, P. I., and Chapman, D. (1991) Fourier transform infrared spectroscopy studies of Ca^{2+}-binding proteins. *Biochemistry* 30, 9681-9686

Kalnin, N. N., Baikalov, I. A., and Venyaminov, S. Yu. (1990) Quantitative IR spectroscopy of peptide compounds in water (H_2O) solutions. III. Estimation of the protein secondary structure. *Biopolymers* 30, 1273-1280

Khurana, R., and Fink, A. L. (2000) Do parallel β-helix proteins have a unique Fourier transform infrared spectrum? *Biophys. J.* 78, 994-1000

Krimm, S. and Bandekar, J. (1986) Vibrational spectroscopy and conformation of peptides, polypeptides, and proteins. *Adv. Protein Chem.* 3, 181-364

Kumosinski, T. F., and Unruh, J. J. (1996) Quantitation of the global secondary structure of globular proteins by FTIR spectroscopy: comparison with X-ray crystallographic structure. *Talanta.* 43, 199-219

Lavialle, F., Adams, R. G., and Levin, I. W. (1982) Infrared spectroscopic study of the secondary structure of melittin in water, 2-chloroethanol, and phospholipid bilayer dispersions. *Biochemistry* 21, 2305-2312

Lee, D. C., Haris, P. I., Chapman, D., and Mitchell, R. C. (1990) Determination of protein secondary structure using factor analysis of infrared spectra. *Biochemistry* 29, 9185-9193

Marsh, D., Müller, M., and Schmitt, F-J. (2000) Orientation of the infrared transition moments for an α-helix. *Biophys. J.* 78, 2499-2510

Martinez, G., and Millhauser, G. (1995) FTIR spectroscopy of alanine-based peptides: assignment of the amide I' modes for random coil and helix. *J. Struct. Biol.* 114, 23-27

Miick, S. M., Martinez, G. V., Fiori, W. R., Todd, A. P., and Millhauser G. L. (1992) Short alanine-based peptides may form 3_{10}-helices and not α-helices in aqueous solution. *Nature* 359, 653-655

Nevskaya, N. A., and Chirgadze, Yu. N. (1976) Infrared spectra and resonance interactions of amide-I and II vibrations of a α-helix. *Biopolymers* 15, 637-648

Pelton, J. T., and McLean, L. R. (2000) Spectroscopic methods for analysis of protein secondary structure. *Anal. Biochem.* 277, 167-176

Prestrelski, S. J., Byler, D. M., and Thompson, M. P. (1991a) Effect of metal ion binding on the secondary structure of bovine α-lactalbumin as examined by infrared spectroscopy. *Biochemistry* 30, 8797-8804

Prestrelski, S. J., Byler, D. M., and Liebman, M. N. (1991b) Comparison of various molecular forms of bovine trypsin: correlation of infrared spectra with X-ray crystal structures. *Biochemistry* 30, 133-143

Prestrelski, S. J., Byler, D. M., and Thompson, M. P. (1991c) Infrared spectroscopic discrimination between α- and 3_{10}-helices in globular proteins. *Int. J. Peptide Protein Res.* 37, 508-512

Pribić, R., van Stokkum, I. H. M., Chapman, D., Haris, P. I., and Bloemendal, M. (1993) Protein secondary structure from Fourier transform infrared and/or circular dichroism spectra. *Anal. Biochem.* 214, 366-378

Reisdorf, W. C., and Krimm, S. (1995) Infrared dichroism of amide I and amide II modes of α_I- and α_{II}-helix segments in membrane proteins. *Biophys. J.* 69, 271-273

Sane, S. U., Cramer, S. M., and Przybycien, T. M. (1999) A holistic approach to protein secondary structure characterization using amide I band Raman spectroscopy. *Anal. Biochem.* 269, 255-272

Sarver, R. W. Jr., and Krueger, W. C. (1991) Protein secondary structure from Fourier transform infrared spectroscopy: a data base analysis. *Anal. Biochem.* 194, 89-100

Sengupta, P. K., and Krimm, S. (1985) Vibrational analysis of peptides, polypeptides, and proteins. XXXII. α-Poly(L-glutamic acid). *Biopolymers* 24, 1479-1491

Surewicz, W. K., and Mantsch, H. H. (1987) Conformational properties of azurin in solution as determined from resolution enhanced Fourier-transform infrared spectra. *Eur. J. Biochem.* 167, 519-523

Susi, H., Timasheff, S. N., and Stevens, L. (1967) Infrared spectra and protein conformations in aqueous solutions. *J. Biol. Chem.* 242, 5460-5466

Susi, H., and Byler, D. M. (1986) Resolution-enhanced Fourier transform infrared spectroscopy of enzymes. *Methods Enzymol.* 130, 290-311

Susi, H., and Byler, D. M. (1987) Fourier transform infrared study of proteins with parallel β-chains. *Arch. Biochem. Biophys.* 258, 465-469

Tamm, L. K. and Tatulian, S. A. (1997) Infrared spectroscopy of proteins and peptides in lipid bilayers. *Q. Rev. Biophys.* 30, 365-429

Tatulian, S. A., Biltonen, R., and Tamm, L. K. (1997) Structural changes in a secretory phospholipase A_2 induces by membrane binding: A clue to interfacial activation? *J. Mol. Biol.* 268, 809-815

Toniolo, C., and Benedetti, E. (1991) The polypeptide 3_{10}-helix. *TIBS*. 16, 350-353

Torii, H, and Tasumi, M. (1992b) Model calculations on the amide-I infrared bands of globular proteins. *J. Chem. Phys.* 96, 3379-3387

Torii, H, and Tasumi, M. (1992a) Application of the three-dimensional doorway-state theory to analysis of the amide-I infrared bands of globular proteins. *J. Chem. Phys.* 97, 92-98

Torres, J., Sepulcre, F., and Padrós, E. (1995) Conformational changes in bacteriorhodopsine associated with protein – protein interactions: A functional α_I - α_{II} switch? *Biochemistry* 34, 16320-16326

Venyaminov, S. Yu., and Kalnin, N. N. (1990) Quantitative IR spectrophotometry of peptide compounds in water (H_2O) solutions. II. Amide absorption bands of polypeptides and fibrous proteins in α-, β-, and random coil conformations. *Biopolymers* 30, 1259-1271

Wilder, C. L., Friedrich, A. D., Potts, R. O., Daumy, G., O., and Francoeur, M. L. (1992) Secondary structural analysis of two recombinant murine proteins, interleukins 1α and 1β: is infrared spectroscopy sufficient to assign structure? *Biochemistry* 31,27-31

Zhang, Y.-P., Lewis, R. N. A. H., Hodges, R. S., and McElhaney, R. N. (1992) Interaction of a peptide model of a hydrophobic transmembrane α-helical segment of a membrane protein with phosphatidylcholine bilayers: Differential scanning calorimetric and FTIR spectroscopic studies. *Biochemistry* 31, 11579-11588

7. Coeficientes de absorción molar integrados absolutos y relativos para la vibración amida I de las diferentes estructuras secundarias de proteínas

Normalmente se asume que todas las estructuras tienen el mismo coeficiente de absorción molar integrado, y por lo tanto los porcentajes de las bandas asignadas a cada estructura nos dan directamente su presencia en la proteína.

Si esta asunción de coeficientes de absorción iguales no es correcta, las estructuras con un coeficiente de absorción mayor se sobreestiman y las de menor se infraestiman. Para evitar este error, una vez asignadas las bandas en la amida I, hemos de ponderarlas por su coeficiente de absorción molar integral relativo. A lo largo de los años han aparecido diferentes trabajos realizados en homopolipéptidos y proteínas fibrilares (estructuras puras), pero también otros realizados en proteínas globulares con diferentes tipos de estructuras, que obtienen coeficientes de absorción molar integrados absolutos o relativos para las diferentes estructuras. La conclusión general de estos estudios es que los coeficientes de absorción integrados varían de estructura a estructura, aunque difieren en la magnitud de las diferencias.

7.1. Polipéptidos

Chirgadze et al. (1973, 1974) obtienen para polipéptidos en D_2O un coeficiente de absorción molar integrado para láminas beta antiparalelas de $6{,}0\times10^4$ M^{-1} cm^{-2}, para hélices alfa de $4{,}6\times10^4$ M^{-1} cm^{-2} y para estructura al azar de $3{,}5\times10^4$ M^{-1} cm^{-2}. La relación entre el coeficiente de estas estructuras es 1 / 0,77 / 0,58.

Jackson et al. (1989) estudiaron la poli-Lys en D_2O para diferentes pD, en los cuales adopta una estructura de láminas beta antiparalelas, de hélices alfa o una estructura desordenada. Encuentran que el coeficiente de absorción integrado sigue la relación 1 / 0,86±0,09 / 0,76±0,06.

Venyaminov y Kalnin (1990) estudiaron la absorción amida I y amida II de varios homopéptidos (poli-Ala, poli-Glu, poli-Lys) y proteínas fibrilares (*silk fibroin* y tropomiosina) en H_2O. Estos péptidos y proteínas sirven como modelo para diversas estructuras, como hélices alfa infinitas, láminas beta antiparalelas infinitas y estructuras al azar. Respecto a los coeficientes de absorción integrado del enlace peptídico en estas tres diferentes conformaciones, obtuvieron para las láminas beta, las hélices alfa, y estructuras al azar valores de $7{,}4\pm1{,}2\times10^4$, $7{,}6\pm1{,}1\times10^4$ y $4{,}6\pm0{,}4\times10^4$ M^{-1} cm^{-2}, respectivamente (relación 1 / 1,03±0,27 / 0,62±0,13). Para la amida II los coeficientes obtenidos son $3{,}5\pm0{,}7\times10^4$, $4{,}0\pm0{,}8\times10^4$, $3{,}5\pm0{,}7\times10^4$ M^{-1} cm^{-2} respectivamente. La relación que mantienen es 1 / 1,14±0,38 / 1,00±0,33, y difiere de la obtenida en la amida I. Como consecuencia, la relación ai/aii en área depende del tipo de estructura, y vale 2,1±0,6 para láminas beta, 1,8±0,5 para hélices alfa, y 1,3±0,3 para estructuras al azar.

7.2. Proteínas

Eckert et al. (1977) obtuvieron los espectros de IR de ocho proteínas en D_2O, con valores de estructura secundaria conocidas. Obtuvieron los espectros propios de las hélices alfa, las láminas beta y del resto de las estructuras. Como utilizaron concentraciones y pasos ópticos conocidos se puede determinar el coeficiente de absorción molar integrado para la amida I-I' en estas tres conformaciones: $7{,}0\times10^4$ M^{-1} cm^{-2} para láminas beta, $5{,}2\times10^4$ M^{-1} cm^{-2} para hélices alfa y $2{,}0\times10^4$ M^{-1} cm^{-2} para el resto de las estructuras. La relación es de 1 / 0,74 / 0,29.

Los espectros de estructuras puras de proteínas obtenidos por Kalnin et al. (1990) permiten obtener el coeficiente de absorción molar integrado para la amida I de las diferentes estructuras. Este coeficiente vale para las láminas betas, hélices, giros y el resto de las estructuras $5{,}0\times10^4$, $4{,}1\times10^4$, $6{,}3\times10^4$ y $2{,}8\times10^4$ M^{-1} cm^{-2}. La relación entre ellos es de 1 / 0,82 / 1,26 / 0.56.

de Jongh et al. (1996) realizaron un estudio para obtener los coeficientes de absorción molar relativos para las estructuras láminas beta, hélices alfa, giros reversos y desordenado. Obtuvieron espectros de películas secas (0,25 g H_2O / g proteína) de quince proteínas solubles mediante RTA. Para poder comparar absorciones introdujeron un estándar interno, que da una banda a 835 cm^{-1}. Los valores obtenidos dependen del modo de definir los porcentajes de estructuras secundarias de cada proteína. Utilizando los porcentajes de estructura secundaria obtenidos según la definición de Kabsch y Sander (1983) la relación entre los coeficientes para las láminas beta, las hélices, los giros reversos y otras estructuras es de 1 / 0,64±0,14 / 0,48±0,32 / 0,37±0,07. Utilizando otros porcentajes de la literatura obtienen una relación de 1 / 0,69±0,09 / 0,33±0,20 / 0,38±0,03.

7.3. Elección de los coeficientes de absorción aplicados

Prácticamente todos los datos apuntan a que el coeficiente de absorción de las láminas beta es el mayor, y lo utilizaremos como referencia para el coeficiente de otras estructuras.

Respecto a las hélices, el coeficiente relativo para polipéptidos es cercano a 0,9, y para proteínas globulares próximo a 0,75. A falta de datos para hélices transmembrana, este último valor es el que asumiremos.

Respecto al de las estructuras al azar su coeficiente relativo es de aproximadamente 0,65. Las estructuras irregulares tendrán un coeficiente relativo alrededor de 0,45.

Para los giros, hay pocas fuentes de información y son contradictorias. El coeficiente relativo medio es de 0,69, pero considerando el trabajo de de Jong et al. (1996) más fiable, utilizaremos el valor más alto coherente con sus resultados, es decir, 0,55.

Todos estos valores están sujetos a errores y podrían variar en el futuro cuando exista más información al respecto, pero probablemente la tendencia se mantendrá. Hemos de recordar que en estos valores mantenemos la asunción que los diferentes tipos de hélices (globulares, membrana, alfa, 3_{10}, más largas,

más curvas, etc.) o de láminas beta (paralelas, antiparalelas, planas, onduladas, más largas, con más cadenas, etc.) mostrarán coeficientes de absorción semejantes.

Por lo tanto, la relación entre los coeficientes para las láminas beta, hélices alfa, giros reversos, estructuras irregulares y estructuras al azar que utilizaremos para obtener la estimación de la estructura secundaria del transportador ADP/ATP es 1 / 0,75 / 0,55 / 0,45 / 0,65.

Referencias

Chirgadze, Yu. N., Shestopalov, B. V., and Venyaminov, S. Yu. (1973) Intensities and other spectral parameters of infrared amide bands of polypeptides in the β- and random forms. *Biopolymers* 12, 1337-1351

Chirgadze, Yu, N., and Brazhnikov, E. V. (1974) Intensities and other spectral parameters of infrared amide bands of polypeptides in the α-helical form. *Biopolymers* 13, 1701-1712

De Jongh, H. H. J., Goormaghtigh, E., and Ruysschaert, J-M. (1996) The different molar absorptivities of the secondary structure types in the amide I region: An attenuated total reflection infrared study on globular proteins. *Anal. Biochem.* 242, 95-103

Eckert, K., Grosse, R., Malur, J., and Repke, K. R. H. (1977) Calculation and use of protein-derived conformation-related spectra for the estimate of the secondary structure of proteins from their infrared spectra. *Biopolymers* 16, 2549-2563

Jackson, M., Haris, P. I., and Chapman, D. (1989) Conformational transitions in poly(L-lysine): studies using Fourier transform infrared spectroscopy. *Biochim. Biphys. Acta.* 998, 75-79

Kabsch, W., and Sander, C. (1983) Dictionary of protein secondary structure: Pattern recognition of hydrogen-bonded and geometrical features. *Biopolymers* 22, 2577-2637

Kalnin, N. N., Baikalov, I. A., and Venyaminov, S. Yu. (1990) Quantitative IR spectroscopy of peptide compounds in water (H_2O) solutions. III. Estimation of the protein secondary structure. *Biopolymers* 30, 1273-1280

Venyaminov, S. Yu., and Kalnin, N. N. (1990) Quantitative IR spectrophotometry of peptide compounds in water (H_2O) solutions. II. Amide absorption bands of polypeptides and fibrous proteins in α-, β-, and random coil conformations. *Biopolymers* 30, 1259-1271

8. Comparación de los resultados obtenidos con los publicados

En el año 2001 se publicó un artículo analizando los espectros de IR del transportador ADP/ATP inhibido con catr (Lórenz et al., 2001). En este artículo se realizaron estudios semejantes a los aquí presentados, en los que se desconvulan, ajustan y asignan bandas a espectros del Anc2pHis inhibido con catr para la forma solubilizado con DM y la reconstituida en liposomas PC/PA. También se determina el nivel de intercambio H/D.

Existe una diferencia en la proteína reconstituida que es importante comentar. En el artículo la reconstitución se realizó en PC/PA con una relación en peso 1/1, mientras que en este trabajo la relación en peso utilizada ha sido de 9/1. Ya que el PA posee carga neta negativa la diferencia puede ser importante.

8.1. Información estructural

Respecto al análisis realizado en el artículo y el aquí presentado hay importantes diferencias.

Por un lado, se ha mejorado la relación señal/ruido de algunos espectros de la proteína. Esto junto con la introducción de la desconvolución por máxima entropía sin restricción de signo, la cual permite estrechamientos bastante superiores a los obtenidos con la desconvolución de Fourier, ha permitido la resolución de nuevas bandas en los espectros.

Estado	Hélices+Otras	Láminas	Giros	
Solubilizada	62-52	19-12	29-26	Este trabajo
	59	15	26	Lórenz et la. (2001)
Reconstituida	59-51	17-11	32-30	Este trabajo
	63	9	28	Lórenz et al. (2001)

Tabla 6.1. Porcentajes de estructura secundaria estimadas para el transportador Anc2pHis inhibido para este trabajo y uno anterior.

Conjuntamente el método de ajuste de bandas ha sido perfeccionado. En el artículo se ajustaban los espectros desconvulados con bandas Voigtianas con una anchura Lorentziana restringida a valores positivos. Aunque este tipo de bandas es una buena aproximación, para bandas Lorentzianas desconvuladas no es perfecta, e introduce errores en el ajuste, especialmente para bandas sobredesconvuladas. En este trabajo se han utilizado las bandas exactas en el ajuste, permitiendo además considerar que las bandas del espectro original no son Lorentzianas puras y contienen carácter Gausiano.

Existen además ciertas diferencias en el análisis, como la utilización de unos coeficientes de absorción para las estructuras diferentes de los aquí utilizados.

A pesar de tantas diferencias, las estimaciones de estructura secundaria entre estos dos trabajos son muy semejantes, tal como se muestra en la tabla 6.1.

8.2. Información del nivel de intercambio H/D

En el artículo de Lórenz et al. (2001) se determina que sólo un 15% de los hidrógenos amida son resistentes al intercambio, mientras que en este trabajo hemos determinado que lo son el 40%. Estas diferencias son sustanciales y requieren una explicación.

Por un lado en el artículo el experimento de intercambio se realizó a 26 ^{o}C midiendo a las 15 horas (en realizad se midió toda la cinética). En este trabajo el intercambio se realizó a 20 ^{o}C midiendo a las 14 horas. Dada la dependencia de la velocidad de intercambio con la temperatura, trabajar a 20 ^{o}C midiendo a las 14 horas es aproximadamente equivalente a trabajar a 26 ^{o}C midiendo a las 7 horas (420 minutos). El intercambio a las 7 horas del experimento presentado en el artículo es de un 80% (20% de las estructuras resistentes al intercambio). Por lo tanto la diferencia no se debe a la diferencia de temperaturas, pues todavía hay una diferencia del 20% (en valor absoluto).

De las seis purificaciones / reconstituciones del transportador para las que se han realizado experimentos de intercambio H/D, tres dan una proteína con un intercambio muy constante, del 39±2% (dos experimentos por purificación / reconstitución). Las otras tres purificaciones dan una proteína con un intercambio variable de experimento a experimento, desde el 15% (30% de los experimentos), al 40% (20% de los experimentos) pasando por el 25% (50% de los experimentos), con un valor medio del 24±10%. Los espectros de absorbancia del transportador obtenido en estas purificaciones son aparentemente normales, pero los espectros de dicroísmo parecen algo diferentes. Esto nos lleva a pensar que en estas tres purificaciones / reconstituciones, el transportador, aunque se incorpora en los liposomas, no lo hace una manera totalmente correcta, y la estructura es quizás menos estable, dando un mayor nivel de intercambio.

Referencias

Lórenz, V. A., Villaverde, J., Trézéguet, V., Lauquin, G. J-M., Brandolin, G., and Padrós, E. (2001) The secondary structure of the inhibited mitochondrial ADP/ATP transporter from yeast analyzed by FTIR spectroscopy. *Biochemistry* 40, 8821-8833.

publicaciones

The Secondary Structure of the Inhibited Mitochondrial ADP/ATP Transporter from Yeast Analyzed by FTIR Spectroscopy[†]

Víctor A. Lórenz,[‡] Joaquim Villaverde,[‡] Véronique Trézéguet,[§] Guy J.-M. Lauquin,[§] Gérard Brandolin,[||] and Esteve Padrós*,[‡]

Unitat de Biofisica, Departament de Bioquímica i de Biologia Molecular, Facultat de Medicina, Universitat Autònoma de Barcelona, 08193 Bellaterra, Barcelona, Spain, Laboratoire de Physiologie Moléculaire et Cellulaire, Institut de Biochimie Cellulaire du CNRS, 1 rue Camille Saint Saëns, 33077 Bordeaux Cedex, France, and Laboratoire de Biochimie et Biophysique des Systèmes Intégrés, UMR 5092 CEA-CNRS-UJF, Département de Biologie Moléculaire et Structurale, CEA/Grenoble, 17 rue des Martyrs, 38054 Grenoble Cedex 9, France

Received January 16, 2001; Revised Manuscript Received April 10, 2001

ABSTRACT: Fourier transform infrared spectroscopy has been applied to the study of the carboxyatractyloside-inhibited mitochondrial ADP/ATP transporter from the yeast *Saccharomyces cerevisiae*, either solubilized in dodecyl maltoside or reconstituted in phosphatidylcholine liposomes. Its secondary structure has been estimated by means of Fourier self-deconvolution followed by curve fit. A Voigt function was used to fit the components of the deconvoluted spectrum, aiming to account for any distortions introduced by deconvolution. For any of the states analyzed, reconstituted or solubilized, in solution or in dry films, 60−70% of the amino acids are found to adopt α-helix plus unordered structures, coherent with the six transmembrane spanning helix model. Moreover, the problem of structure preservation on drying was addressed, and several observations pointed to a maintenance of the protein structure in dry films. Comparison of reconstituted and solubilized samples indicated the presence of both lipid-induced changes in the protein (decrease of the β-sheets and increase of unordered structures) and protein-induced changes in the lipids (strong hydrogen bonding of lipid C═O groups). To obtain a better discrimination of α-helix and unordered structure contributions for the reconstituted form, H/D exchange experiments were performed. Between 35% and 45% of the amino acids were finally assigned to α-helix structures, compatible with the existence of five or six transmembrane spanning helices in the transporter. The level of H/D exchange was determined after 15 h of exposure to D_2O vapor to be 85%, reflecting a high accessibility of the amide hydrogens even for the carboxyatractyloside-inhibited state.

The ADP/ATP carrier is a protein of the inner mitochondrial membrane, which exclusively catalyzes the 1-to-1 exchange of cytosolic ADP, imported into mitochondria, for ATP generated in the matrix space by oxidative phosphorylation. The ADP/ATP transport system can be blocked by very specific inhibitors, which bind to the carrier with high affinity. They belong to two families: atractyloside and carboxyatractyloside on one hand, which bind to the transporter in the so-called CATR conformation, and bongkrekic acid and isobongkrekic acid on the other hand, able to bind to the transporter in the so-called BA conformation. Binding of the inhibitors to the carrier results in carboxyatractyloside− and bongkrekic acid−carrier complexes, which exhibit different chemical, immunochemical, and enzymatic reactivities. It has been suggested that the transition between the CATR and BA conformations is involved in the ADP/ATP transport process (for a review see ref *1*). Therefore, structural analysis of these complexes would be invaluable in understanding the nucleotide transport mechanism at the molecular level.

In the yeast *Saccharomyces cerevisiae*, three highly similar genes encoding the ADP/ATP carrier have been isolated (*2*−*4*). Only the ANC2 isoform is required for the cells to grow on a nonfermentable carbon source, such as glycerol or lactate (*5*, *6*). In this study we used the yeast mitochondrial ADP/ATP carrier isolated from a genetically modified strain of *S. cerevisiae*, which produces the His-tagged Anc2p[1] isoform of the carrier (Anc2pHis).

Infrared spectroscopy, through the study of the protein amide I and amide II bands, has been proven to be a valuable tool for the protein secondary structure estimation (*7*−*9*).

[†] This work was supported by Grants Bio4-CT97-2119 from the European Commission (to G.B., G.J.-M.L., and E.P.) and 1999SGR00102 from the Direcció General de Recerca (Generalitat de Catalunya) and Fellowship 1998-FI-00215 from the DGR (Generalitat de Catalunya) (to V.A.L.). J.V. is a fellow of the European Commission (Bio4-CT97-2119).

* Corresponding author. Tel: +34-935811870. Fax: +34-935811907. E-mail: esteve.padros@uab.es.

[‡] Universitat Autònoma de Barcelona.

[§] Institut de Biochimie Cellulaire du CNRS.

[||] CEA/Grenoble.

[1] Abbreviations: Anc2p, mitochondrial ADP/ATP transporter; Anc2pHis, 6 histidine tagged mitochondrial ADP/ATP transporter; ATR, attenuated total reflection; DM, dodecyl maltoside; FTIR, Fourier transform infrared; FWHH, full width at half-height; FSD, Fourier self-deconvolution; IR, infrared; *k*, narrowing factor; n_1, n_2, and n_3, refractive index of the ATR crystal, sample, and air; γ, FWHH of a band before FSD; γ', FWHH used in FSD; ϵ, absorption coefficient; *B*, integrated absorption coefficient; *p*, order parameter of the dipole transition moment; E_x, E_y, and E_z, time averaged electric fields; θ, angle between the IR beam and the crystal surface normal; egg PC/PA, egg phosphatidylcholine and phosphatidic acid; S/N, signal-to-noise standard deviation ratio.

10.1021/bi010091s CCC: $20.00
Published on Web 06/30/2001

The correlation between amide I and amide II band position and secondary structure has been demonstrated from both experimental studies on homopeptides of known secondary structures (*10*, *11*) and theoretical studies on homopeptides with pure secondary structure (*10*, *12*). Spectra deconvolution followed by curve fitting has been used to resolve the contributions of the different secondary structures in the amide I (*13*, *14*). Gaussian, Lorentzian, and mixed Gaussian−Lorentzian bands have been used to fit deconvoluted spectra, although without a clear justification. In the present work Voigt functions have been used to curve fit deconvoluted spectra. When this band profile is used, reliable estimates for position, width, and area of the components bands are obtained, increasing the reliability of the final fit to this spectrum (results to be published).

Infrared spectroscopy also provides the opportunity to study the H/D exchange by following the decrease in the amide II band area. Upon exchange of the hydrogen of the amide groups by deuterium, the amide II band disappears, being reconverted in two new bands; one of them, called amide II′, appears 100 cm^{-1} down from the amide II, and the second one appears around 1000 cm^{-1} (*8*, *9*). Although major information comes from the analysis of the kinetics of exchange (*15*), the total exchange at an appropriated long time of exchange can give some clues to the accessibility of the amide hydrogen atoms to the solvent and provides a way to compare the Anc2p with other membrane proteins.

These spectroscopic techniques were used in the present work to get an approach to the secondary structure of the adenine nucleotide carrier Anc2p from yeast. Unfortunately, the free form of the Anc2p has been shown to be very labile when isolated from mitochondria (*16*). After an exhaustive purification at least half of the binding sites are commonly lost (*17*, *18*). Attempts have been done to shorten the time the protein spends solubilized in detergent, aiming to reduce lose of protein binding sites. Regrettably, after this fast purification procedure the protein purity decreased dramatically to half of the total protein (*19*). As a consequence the present studies were restricted to the carboxyatractyloside-inhibited transporter in order to have pure protein blocked in a well-defined conformational state. It is important to realize that carboxyatractyloside binds tightly to the protein in one of the conformations involved in the ATP/ADP transport (the CATR conformation), and although not active, the resultant complex should display a structure very similar to that of the free protein in the CATR conformation and thus should be considered as a good model for this conformation. As a conclusion, the presence of the inhibitor, although avoiding the achievement of any functional studies, should not affect structural studies to be done.

Two forms of inhibited Anc2pHis sample preparations were used, solubilized in the nondenaturing detergent dodecyl maltoside or reconstituted in negatively charged liposomes, to test the influence of the hydrophobic environment surrounding the carrier, either micellar or membrane bilayer, respectively. Moreover, the suitability of studying the Anc2pHis preparations in the form of dry films was tested.

MATERIALS AND METHODS

Yeast Strains and Media. We used the genetically modified JL1-3-ANC2(His6) *S. cerevisiae* yeast strain, which produced a modified isoform of Anc2p containing the extra sequence GSRSHHHHHH at its C-terminal end (Anc2pHis) (*20*). JL1-3-ANC2(His6) yeast cells were grown as described (*17*).

Preparation of Yeast Mitochondria. Yeast cells were harvested during exponential growth phase when the OD 540 nm reached a value of 5.0. Mitochondria were prepared as described (*21*). Briefly, protoplasts obtained by enzymatic digestion of the cell wall with Zymolyase 20T (Seikagaku Corp.) were disrupted with a Dounce homogenizer in a medium made of 0.6 M mannitol, 0.1 mM EDTA, 10 mM Tris-HCl, 0.1% BSA. and 1 mM phenylmethanesulfonyl fluoride (PMSF), pH 7.4. Mitochondria were isolated by differential centrifugation, washed with the same medium but devoid of BSA and PMSF, and stored in liquid nitrogen.

Purification of the Carboxyatractyloside-Inhibited Anc2pHis. All purification steps were carried out at 4 °C. Isolated yeast mitochondria were preincubated with carboxyatractyloside, suspended at 10 mg of protein/mL in 0.1 M Na_2SO_4, 1 mM EDTA, 1 mM diisopropyl fluorophosphate, and 10 mM Tris-HCl, pH 7.3, and solubilized by addition of 1% DM and 1% Emulphogen BC720. The soluble extract was submitted to hydroxylapatite (HTP) chromatography (*22*) with modifications (*17*). Partially purified Anc2p and Anc2pHis were recovered in the flow-through fraction. Anc2pHis was further purified by immobilized metal ion affinity chromatography (IMAC) using the Ni−NTA resin, following the experimental conditions previously established (*20*). Briefly, Anc2pHis was bound to the resin in the presence of 5 mM $MgSO_4$, 50 mM NaP_i, pH 7.3, and 0.1% DM. After extensive washing of the resin, it was eluted by 500 mM imidazole in 50 mM NaCl and 10 mM Mes, pH 6.8, with 0.02% DM. Pure Anc2pHis was then subjected to a overnight dialysis at 4 °C in front of 50 mM NaCl and 10 mM Mes, pH 6.8, with 0.015% DM. In these conditions the carboxyatractyloside-inhibited Anc2pHis was obtained at a concentration of about 0.04 mg/mL. The presence and purity of protein from the HTP chromatography and the Ni−NTA batch eluates were determined from a 12% SDS−PAGE stained with Coomassie Blue (see Figure 1). For IR studies, solubilized Anc2pHis was concentrated using Centriprep YM30 (Amicon). Final concentration was measured by UV−vis absorbance at 280 nm using ϵ_{280}(Anc2p) = 0.9 $(g/mL)^{-1}$ cm^{-1} [from ϵ_{280}(Trp) = 4500 M^{-1} cm^{-1} and ϵ_{280}(Tyr) = 1500 M^{-1} cm^{-1}], and by the bicinchoninic acid method (*23*), giving similar results.

Reconstitution of the Carboxyatractyloside-Inhibited Anc2pHis. To the purified Anc2pHis was added egg PC/PA (1:1 w/w) presolubilized with DM to a final lipid-to-protein ratio of 3:1 (w/w) and final DM-to-lipid ratio of 2:1 (w/w). After 1−2 h of incubation at 4 °C, Bio-Beads were added to a final ratio to DM of 33:1 (w/w). After 6 h of soft stirring at 4 °C the proteoliposomes obtained were centrifuged at 90000*g* for 90 min. The pellet was resuspended to the final concentration used in the experiments.

FTIR Transmission Experiments. (A) Sample Preparation. For IR transmission experiments of solubilized samples in solution, the carboxyatractyloside-inhibited Anc2pHis was dissolved at a concentration of 10 mg/mL, in 9.2% DM, 10 mM Mes, and 50 mM NaCl (pH 6.8), and was placed between two CaF_2 windows using a 6 μm tin spacer. For transmission spectra of dry fims of solubilized protein, 0.2

mg of protein was spread over a CaF_2 window and dried under vacuum.

(B) Spectra Acquisition. A total of 1000 scans were coadded in blocks of 40 reference scans and 40 sample scans using a shuttle accessory, with an instrumental resolution of 2 cm^{-1} on a Mattson Polaris FTIR equipped with an MCT detector. The resulting interferogram was apodized with a triangle function and processed to give an absorption spectra at 0.5 cm^{-1} digital resolution. The sample was placed in a circulating water holder connected to a thermostatic bath. An external probe fitted to the sample holder was used to keep the temperature at 25.0 ± 0.05 °C. The spectrometer compartment was purged with dry air, having finally a dew point lower than −50 °C. This low water vapor concentration, together with the spectra acquisition in blocks, usually gave absorption spectra free from water vapor bands.

(C) Buffer Subtraction. For transmission experiments in solution a buffer spectrum was collected and subtracted to eliminate the contribution of water, detergent, and salts. The subtraction factor was chosen as that leaving a flat baseline between 2000 and 1800 cm^{-1}.

FTIR Attenuated Total Reflection Experiments. (A) Sample Preparation. Eighty micrograms of the carboxyatractyloside-inhibited protein at a concentration of 4 mg/mL, in 12 mg/mL egg PC/PA (1:1 w/w), 10 mM Mes, and 50 mM NaCl (pH 6.8), was spread on a 45° trapezoid ATR germanium crystal of 50 × 20 × 10 mm. The sample was dried at the atmospheric humidity first and under a dry nitrogen flow later.

(B) Exchange Experiments. A dry film of the reconstituted protein was exposed to a continuous flow of dry nitrogen (150 mL/min) saturated of D_2O at 26 °C. The amide I area was measured from 1690 to 1615 cm^{-1}. For the amide II two intervals were used, 1580−1520 cm^{-1} and 1560−1530 cm^{-1}. When the broader interval was used, a slightly higher exchange level was measured.

(C) Spectra Acquisition. A total of 2000 scans were coadded at an instrumental resolution of 2 cm^{-1} on a Bio-Rad FTS 6000 spectrometer equipped with an MCT detector. The resulting interferogram was apodized with a triangle function and processed to give an absorption spectrum at 0.5 cm^{-1} digital resolution. A cover jacket was placed over the ATR crystal and connected to a circulating thermostatic bath at 26 °C. The spectrometer compartment was purged with dry air, having finally a dew point lower than −40 °C. No block averaging was used; under these conditions the presence of residual water vapor peaks in the absorption spectra cannot be fully prevented, so water vapor was collected and subtracted when needed.

(D) Characterization of the Films Used in ATR-FTIR. It is necessary to determine if the films studied by ATR are described by the thin film hypothesis (film thickness infinitesimally small compared to the IR light penetration depth) or by the thick film hypothesis (thickness much bigger that the penetration depth). In the thin film case the effective path length, and therefore the measured absorbance, is proportional to the film thickness, resembling the transmittance spectra. In contrast, in the thick film case the effective path length is independent of the actual film thickness but decreases as the wavenumber increases. Then, comparison between the area ratios of two separated bands obtained from both transmittance and ATR allows the discrimination between thick and thin film hypotheses. For a thin film the area ratio of two bands A_1/A_2 is the same as in transmittance, but for a thick film it becomes $(A_1/A_2)_{trans} = (\nu_1/\nu_2)(A_1/A_2)_{ATR}$, where ν_1 and ν_2 are the positions of the two bands (*15*).

Spectral Corrections and Determination of Experimental Errors. (A) Amino Acid Side Chain Absorption Subtraction. A synthetic amino acid side chain absorption spectrum was constructed from the data of Venyaminov and Kalnin (*24*) for H_2O spectra and Chirgadze et al. (*25*) for D_2O spectra, taking into account the primary sequence of the Anc2pHis (*18*). The subtraction factor was calculated from the protein concentration and path length.

(B) Phospholipid and DM Absorption. The phospholipids used have no significant absorption in the amide I or II, neither between 4000 and 3150 cm^{-1}, so amide A (with maximum around 3290 cm^{-1}) and remaining water (maximum around 3400 cm^{-1}) are directly observed in reconstituted samples. DM shows no absorption in the amide I or II, but it does between 3500 and 3100 cm^{-1}, preventing the direct observation of amide A and remaining water in DM solubilized samples.

(C) Determination of Absorption Coefficients (ϵ) and Integrated Absorption Coefficients (B) by Transmittance. For H_2O solutions, the path length was calculated essentially as described (*26*). However, due to the baseline uncertainty when using MCT detectors (*27*) the difference absorption coefficients between 2125 and 1880 cm^{-1} for H_2O at 25 °C was preferred: $(\epsilon_{2125} - \epsilon_{1880}) = 1.55\ M^{-1}\ cm^{-1}$. Water concentration was calculated assuming a volumetric mass for solutes equal to 1 g/L. For dry films it was assumed that the integrated absorption coefficients for acyl bands of DM and egg PC (3100−2800 cm^{-1}) are independent of the humidity. The following coefficients were determined: DM acyl stretching, $B_{3000-2800} = (187 \pm 14) \times 10^3\ g^{-1}\ cm$; egg PC acyl stretching, $B_{2975-2775} = (212 \pm 14) \times 10^3\ g^{-1}\ cm$; egg PC C═O stretching, $B_{1760-1700} = (18.0 \pm 1.6) \times 10^3\ mmol^{-1}\ cm^{-2}$; and dry film egg PC C═O stretching, $B_{1760-1700} = (22 \pm 4) \times 10^3\ mmol^{-1}\ cm^{-2}$.

(D) Determination of the Signal-to-Noise Ratio. Using an interval free of sample bands (usually between 1800 and 1850 cm^{-1}) a straight line was fitted. The standard deviation of the residual was taken as the noise standard deviation at 1825 cm^{-1} (SD_1). The noise standard deviation at the amide I maximum (SD_2) was calculated as described (*28*) using

$$SD_2 = SD_1 \times 10^{Abs_2 - Abs_1}$$

where Abs_2 is the absorption in the original nonsubtracted spectrum at the amide I maximum and Abs_1 the absorption at 1825 cm^{-1}. Then the signal-to-noise ratio was calculated, taking as signal the absorbance at amide I maximum and as noise the calculated value of SD_2.

(E) Determination of the Error Due to Orientation of the Sample. For a globally oriented protein with axial symmetry relative to the ATR crystal, or to the windows in transmittance setup, even using unpolarized light the absorbance depends on the orientation, leading to errors in quantitative analysis and thus in the estimation of secondary structure of proteins (*29*). The absorbance using unpolarized light is for most interferometers approximately equal to the addition of

the absorbance using parallel and perpendicular polarized light (*15*) according to

$$\mathrm{Abs}_{\mathrm{unpol}} = 0.5\mathrm{Abs}_{90} + 0.5\mathrm{Abs}_{0}$$

We define the relative error of the absorbance of one band corresponding to a globally oriented protein with respect to the same protein with nonglobal orientation as

$$\text{error} = \frac{\mathrm{Abs}_{90}(p) + \mathrm{Abs}_{0}(p)}{\mathrm{Abs}_{90}(p=0) + \mathrm{Abs}_{0}(p=0)} - 1$$

where p is the order parameter of the transition dipole moment of the considered band with respect the surface normal (p is equal to 0 for a nonoriented protein). For ATR, the absorbance depends on optical parameters (see ref *15* for expressions of E_x, E_y, E_z dependency on n_1, n_2, n_3, and θ), and the relative error becomes

$$\text{error} = \frac{(1-p)(E_x^2 + E_y^2) + (2p+1)E_z^2}{E_x^2 + E_y^2 + E_z^2} - 1$$

Taking the thin film hypothesis and using the values for a proteolipid film on a germanium plate ($n_1 = 4.0$, $n_2 = 1.5$, $n_3 = 1.0$, and $\theta = 45°$), the relative error becomes er $= -0.705p$ and goes from -70.5% for $p = 1$ (reduction of absorbance in globally oriented proteins for bands with the transition dipole moment parallel to the crystal surface normal) to $+35\%$ for $p = -0.5$ (enhancement in perpendicular orientation). For the thick film hypothesis in the same conditions the relative error becomes er $= 0.164p$, and it goes from $+16\%$ for $p = 1$ to -8% for $p = -0.5$.

For transmission spectra the relative error is expressed as

$$\text{error} = \frac{2\cos^2\theta(1-p) + \sin^2\theta(2p+1)}{2\cos^2\theta + \sin^2\theta} - 1$$

where θ stands for the angle between the beam and the window normal. In the standard disposition $\theta = 0°$, and the error becomes er $= 1 - p$, going from -100% for $p = 1$ (no band absorption) to $+50\%$ for p $= -0.5$ (absorption enhancement).

Quantitative Analysis of the Spectral Components of Protein Amide I. (A) Fourier Self-Deconvolution and Maximum Likelihood Restoration. These procedures were performed using the programs supplied by Spectrum Square Associates, Inc., implemented in the GRAMS software (Galactic Industries). For Fourier self-deconvolution (referred to in the following as deconvolution) a Lorentzian profile was used, with full width at half-height (FWHH) of γ', filtered with a Bessel function and a narrowing factor of k as defined by Kauppinen et al. (*30*). For maximum likelihood restoration a Lorentzian profile with FWHH of γ', no smooth, 0.2% of uncertainty and 10 000 iterations were used.

(B) Curve Fitting Procedures. Curve fitting was carried out using the program CURVEFIT supplied by Spectrum Square Associates, Inc., which uses the Levenberg−Marquardt method to find the parameters that yield a minimum χ^2. The program does not allow negative values for any parameter; when a parameter hits this limit, it was fixed to zero. Iterations were performed until a minimum was found or the χ^2 changed less than 1 in 10^5 in one iteration (our criteria of convergence) to a maximum of 1000 iterations.

(C) Curve Fit of Deconvoluted Spectra. To obtain accurate results on curve fitting overlapped bands, the shape of the component bands should be well characterized. The deconvolution procedure introduces changes in the band shapes. For an infrared spectrum composed by n pure Lorentzian bands with FWHH of γ_i, deconvolution will give a sum of bands with the following shape: a residual Lorentzian character with FWHH of $\gamma_i' = (\gamma_i - \gamma')$ convoluted with the Fourier transform of a Bessel function of FWHH equal to γ'/k (*31*). As the Fourier transform of a Bessel function resembles a Gaussian band, the new bands can be closely described as Voigt functions (convolution of a Lorentzian band and a Gaussian band). Therefore, the Voigt function was used to curve fit the deconvoluted spectra (suitability of this approach is shown in a paper being prepared for publication). A Voigt function contains four parameters: area, position, Lorentzian width, and Gaussian width. During the curve fitting procedure the Gaussian width (γ_G) is fixed to $0.94\gamma'/k$, and the rest of parameters are set free. After convergence, the fit gives the area (A_i), position (v_i), and Lorentzian FWHH (γ_i') of bands in the deconvoluted spectrum. Since the fitting algorithm does not allow negative values for γ_i', when this parameter reaches zero for any band, it cannot be distinguished if the band has been properly Fourier self-deconvoluted ($\gamma_i = \gamma'$) or overdeconvoluted ($\gamma_i < \gamma'$); in that case, γ_G was allowed to be adjusted during the curve fitting but constrained to be equal or lower than $0.94\gamma'/k$. Usually less than 200 iterations were needed to fulfill our criteria of convergence. No baseline was introduced in the curve fit (if baseline correction was needed, an offset was previously subtracted before the iterations were started). The number of bands introduced in the fit was determined as those visually observable at the spectrum, as clearly resolved maxima, or well-defined shoulders. The number of bands was limited by the following restriction: the residual at the amide I should be similar in amplitude to the noise observed after deconvolution in a near zone free of bands (around 1800 cm^{-1}). If the residual is too low, overfitting was concluded; on the other hand, the need of an extra band was detected when systematic deviations in the residual, higher than the noise, were observed. Also, as in deconvolution the interferogram is cut at $0.95k/\gamma'$ cm (*13*, *30*), the nominal resolution in the deconvoluted spectra becomes $1.05\gamma'/k$ cm^{-1}, putting a final limit to the number of bands possibly resolved after deconvolution (*13*).

(D) Curve Fit of Original Spectra. Since deconvolution does not distort the area or position of a individual band but reduces the Lorentzian width (*32*), all of the parameters can be directly translated from the deconvoluted to the original spectra, except for the Lorentzian width, that should be calculated using the expression $\gamma_i = (\gamma_i' + \gamma')$. For overdeconvoluted bands, original widths can roughly be estimated as $\gamma_i = k\gamma_G$. The curve fit of original spectra was done between 1850 and 1480 cm^{-1}. Voigt functions were introduced, keeping fixed the position and the Lorentzian width previously determined from the curve fit to a deconvoluted spectrum. The Gaussian width was fixed to zero, and only the band heights and a zero slope baseline were set free. Under these conditions the fit becomes a linear one. After convergence, all of the parameters of bands above 1700

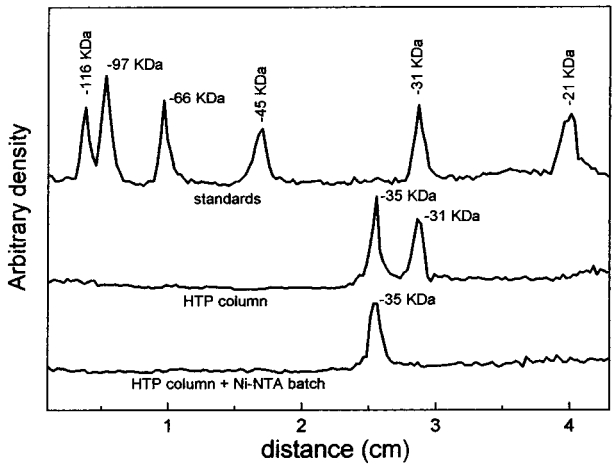

FIGURE 1: SDS−PAGE densitogram for the molecular mass standards (top), HTP column elution (middle), and HTP column elution further purified with a Ni−NTA resin (bottom). For the HTP and HTP + Ni−NTA lanes the molecular masses of the bands were obtained by interpolation from the standards. From band integration, the Ancp2His purity was estimated to be better than 95%.

cm^{-1} and below 1600 cm^{-1} (including the Gaussian width) were set free, and a minimum of 200 iterations were performed. Then, all of the parameters, except positions of bands between 1700 and 1600 cm^{-1}, were set free, and 1000 iterations were performed. Finally, all of the parameters were set free and 1000 iterations were performed.

RESULTS

As described in Materials and Methods, the carboxyatractyloside-inhibited Anc2pHis was purified from mitochondria in a two-step procedure: a hydroxylapatite (HTP) chromatography followed by affinity chromatography using a Ni−NTA resin. In Figure 1 the densitogram of different lanes obtained from a SDS−PAGE is displayed. The lane corresponding to the HTP column eluate shows only two bands: a 35 kDa band assigned to Ancp2His and a 31 kDa band assigned to the mitochondrial phosphate transporter (*20*). At this step of purification the Anc2pHis showed 60% purity. After the second step of purification (Ni−NTA batch), only one single band was evident, assigned to the Anc2pHis. The purity at this step was higher than 95% and thus was suitable for FTIR studies.

FTIR Characterization of Solubilized Anc2pHis. Figure 2A presents the spectrum of the carboxyatractyloside-inhibited Anc2pHis solubilized in DM, after buffer subtraction. A buffer subtraction factor of 0.971 was considered to be optimum, but factors from 0.975 to 0.967 gave also acceptable results. The amide I maximum was located at 1655.2 cm^{-1}, the amide II at 1546.7 cm^{-1}, and the tyrosine (from the fourth derivative) at 1517.1 cm^{-1}. The amide I/amide II ratio intensity was determined to be 1.44 ± 0.14, and the absorption coefficient was 192 ± 8 M^{-1} cm^{-1} for the amide II and 280 ± 40 M^{-1} cm^{-1} for the amide I, where the errors arise from the uncertainty in the factor of buffer subtraction. Figure 2A also shows the side chain amino acid absorption and the Anc2pHis spectrum once the amino acid side chain contribution was subtracted. To determine the scaling factor, protein concentration was taken as 10 mg/mL and the path length as 8.4 μm. It was calculated that 15.5% of the area

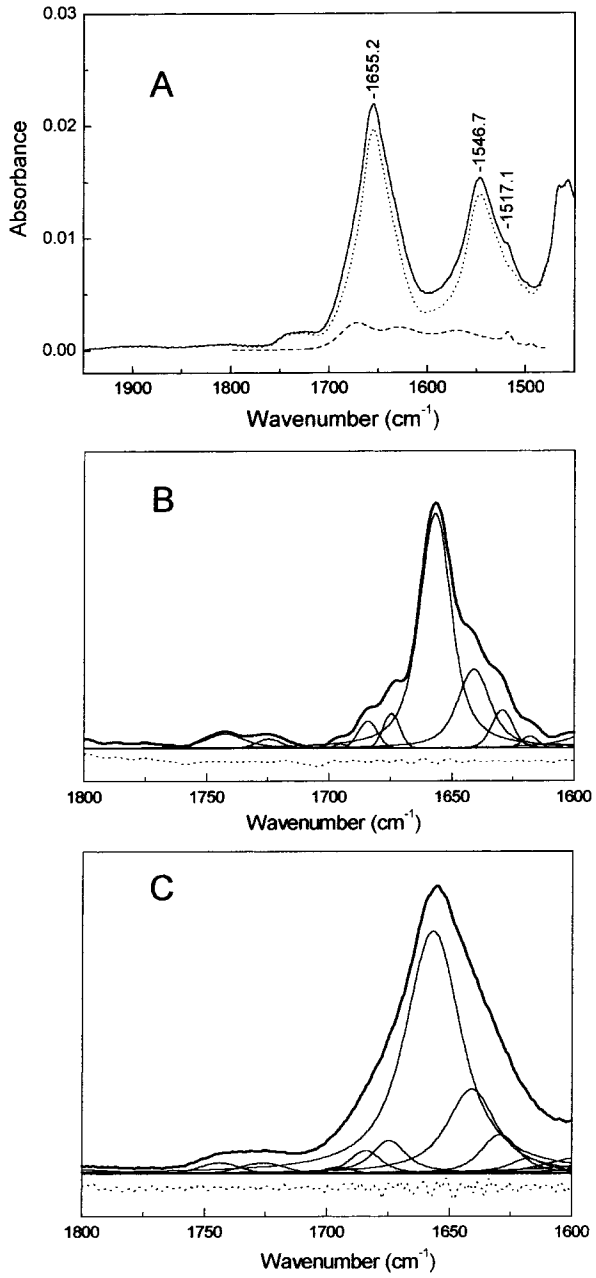

FIGURE 2: (A) (—) Transmission absorption spectrum of the solubilized carboxyatractyloside-inhibited Anc2pHis in H_2O at 25 °C once contributions arising from buffer have been subtracted. Before subtraction, the spectrum had a 0.88 AU in the amide I maximum (1655 cm^{-1}). The noise standard deviation (at 1825 cm^{-1}) was 2.2 × 10^{-5} AU. The noise standard deviation at the amide I maximum was calculated to be 1.4 × 10^{-4} AU, giving a S/N for the amide I equal to 150. (- - -) Synthetic amino acid side chain spectrum from the data reported by Venyaminov et al. (*24*). (•••) Anc2pHis spectrum once the amino acid contribution has been subtracted. (B) (—) Deconvolution and curve fit of the spectrum shown in (A) once the amino acid chain contribution (except that of tyrosine) has been removed. For the deconvolution the following parameters have been used: a Lorentzian band shape of $\gamma' = 18$ cm^{-1}, a $k = 2.0$, and a Bessel apodization, giving a new nominal resolution of 9.5 cm^{-1}. The results of the fit are presented in Table 1. (•••) Curve fit residual, at the same scale, shifted down for a clear display. (C) (—) Curve fit of the original spectrum shown in (A). The amino acid side chain contribution (except that of tyrosine) has been removed. The curve fit was performed as described in Materials and Methods, but the positions determined from the deconvoluted spectrum were fixed for bands assigned to amide I. Fit results are presented in Table 1. (•••) Curve fit residual multiplied by 5 and shifted down for a clear display.

Table 1: Summary of the Curve Fit to the Deconvoluted Spectrum of Solubilized Carboxyatractyloside-Inhibited Anc2pHis (Figure 2B) and the Curve Fit to the Original Spectrum Shown in Figure 2C, Together with the Proposed Assignments for the Bands

deconvoluted		original				
position[a]	% area	position[a]	FWHH[b]	% *L*[b]	% area	assignments
1742.4		1743.7	19	0		phospholipid C═O
1724.6		1726.2	22	0		phospholipid C═O
1695.3	0.4	1695.3	13	0	0.6	β-sheets
1684.2	3.5	1684.2	15	55	3.2	reverse turns
1674.6	4.0	1674.6	17	85	5.5	reverse turns
1656.6	64.2	1656.6	27	75	63.9	α-helix + unordered
1641.0	21.9	1641.0	24	85	20.2	β-sheets
1629.4	6.0	1629.4	18	55	6.5	β-sheets
1617.8		1617.8	16	100		tyrosine

[a] In cm^{-1}. [b] The Voigt function used to fit the original spectrum, described by the parameters Lorentzian width and Gaussian width, is presented as its equivalent mixed Gaussian−Lorentzian profile with two parameters: FWHH in cm^{-1} and the percentage in height of the Lorentzian character (% *L*).

from 1700 to 1480 cm^{-1} (baseline at 1850 cm^{-1}) corresponds to the side chain amino acid absorption. This is in good agreement with the value calculated following the procedure reported by Rahmelow et al. (*33*), which predicts a 16.7% from the primary sequence of Anc2pHis. When path length or protein concentration was unknown, data from Rahmelow et al. (*33*) were used to determine the subtraction factor for the amino acid side chain spectrum.

Secondary Structure Analysis: Curve Fit and Deconvolution. Figure 2B shows the deconvolution of the spectrum presented in Figure 2A (once the amino acid side chain contribution, except tyrosine, was subtracted). In the same figure the component bands obtained by curve fitting are also presented. Three bands were found to be overdeconvoluted as reported by the curve fit: 1695, 1675, and 1618 cm^{-1} bands. A curve fitting of the original spectrum was also performed (shown in Figure 2C). In this case, the data derived from the curve fit to the deconvoluted spectrum (number of bands, position, width) were used as the starting point of the curve fitting procedure. The fitting was carried out as described in Materials and Methods, but the last fitting step was omitted and band positions were kept fixed. This was done because the standard deviation of the residual was 7×10^{-5} AU, already lower than the noise standard deviation calculated at 1660−1630 cm^{-1} (1.5×10^{-4} AU), and therefore further reduction of the residual was meaningless.

Table 1 presents the parameters obtained from the curve fit to the deconvoluted as well as to the original spectra, together with the proposed assignments. The 1744 and 1726 cm^{-1} bands were assigned to the C═O stretching from the ester group of phospholipids. Using the integrated absorption coefficient of C═O phospholipid vibration (for egg PC) and the protein concentration, it was concluded than 15 ± 2 molecules of phospholipid kept bound per Anc2pHis dimer in the presence of DM. The 1618 cm^{-1} band was assigned to tyrosine. The rest of the bands were assigned according to reviewed data (*7, 34*).

The estimated secondary structure composition for the solubilized Anc2pHis−carboxyatractyloside complex in aqueous buffer (H_2O) averaged for two independent samples is presented in Table 4. The calculation was performed considering that the different secondary structures have different integrated absorption coefficients (*35*). This calculation was applied to the data derived from the curve fit to the deconvoluted spectrum and to the original spectrum; these estimations agreed within 4%. Different structure estimation could also be obtained from data in Table 1, assuming that the area is just directly proportional to the amount of the assigned structure. Obviously, it will lead to overestimation of β-sheets and underestimation of turns, compared to the determination using the coefficients of de Jong et al. (*35*). Which solution is more exact is a matter of debate, since the relative integrated absorption coefficient for turns with respect to β-sheets determined by de Jong et al. (*35*) is very imprecise (0.3 ± 0.2).

It can be concluded that the carboxyatractyloside-inhibited Anc2pHis in the solubilized state has mainly α-helix plus unordered structures (about 60%), compatible with the predicted 40% of the amino acids forming six transmembrane α-helices for the Anc2p (*36*). Later on, the problem of discriminating the α-helix and unordered contributions will be assessed for the reconstituted state.

Dry Film of Solubilized Anc2pHis. The interest in studying a dry film of a protein by FTIR comes mainly from the difficulties, when working with protein aqueous solutions (H_2O), to obtain an amide I profile with sufficient S/N for the analysis requirements. This low S/N in solution comes from the strong water absorption at 1645 cm^{-1}. Moreover, buffer subtraction, an unavoidable step prior to any analysis, is prone to errors and personal bias (*26*). In contrast, when proteins are studied in dry films, high S/N is commonly achieved, and water subtraction is not necessary for analysis. Artifacts may appear in this case, however, from protein structural changes upon dehydration, although several studies (*15, 37*) suggest that these effects are not common, even for soluble proteins.

Figure 3A shows a transmission absorption spectrum of a dry film of the solubilized carboxyatractyloside-inhibited Anc2pHis. Amide I maximum is shifted upward 2.3 cm^{-1} and the amide II maximum downward 0.7 cm^{-1} with respect to that of solution. These shifts are in agreement with differences generally observed between solution samples and film samples (*15*). The amide I/amide II intensity ratio was 1.68, suggesting that some water may be present in the dry film. This could not be directly checked at 3400 cm^{-1} as DM absorbs between 3500 and 3200 cm^{-1} (sugar O−H stretching). Taking into account the DM acyl integrated absorption coefficient and the DM-to-protein ratio (9:1 w/w), it was possible to determine the amount of protein (0.084 ± 0.004 mg cm^{-2}) and the peptide bond absorption coefficient for the amide I (370 ± 30 M^{-1} cm^{-1}) and the amide II (220 ± 20 M^{-1} cm^{-1}) bands. The amide II coefficient is in agreement with that of solution, but the amide I coefficient is significantly higher, indicating that remaining water is present in the film. The amino acid side chain absorption spectrum was subtracted with a factor derived from the calculated amount of protein.

Figure 3B shows the deconvoluted spectrum of Figure 3A. Since under the optimal conditions of deconvolution the spectrum appears less defined than the spectrum of the liquid sample, two different sets of deconvolution parameters were used; one (top trace) was used to determine the number of

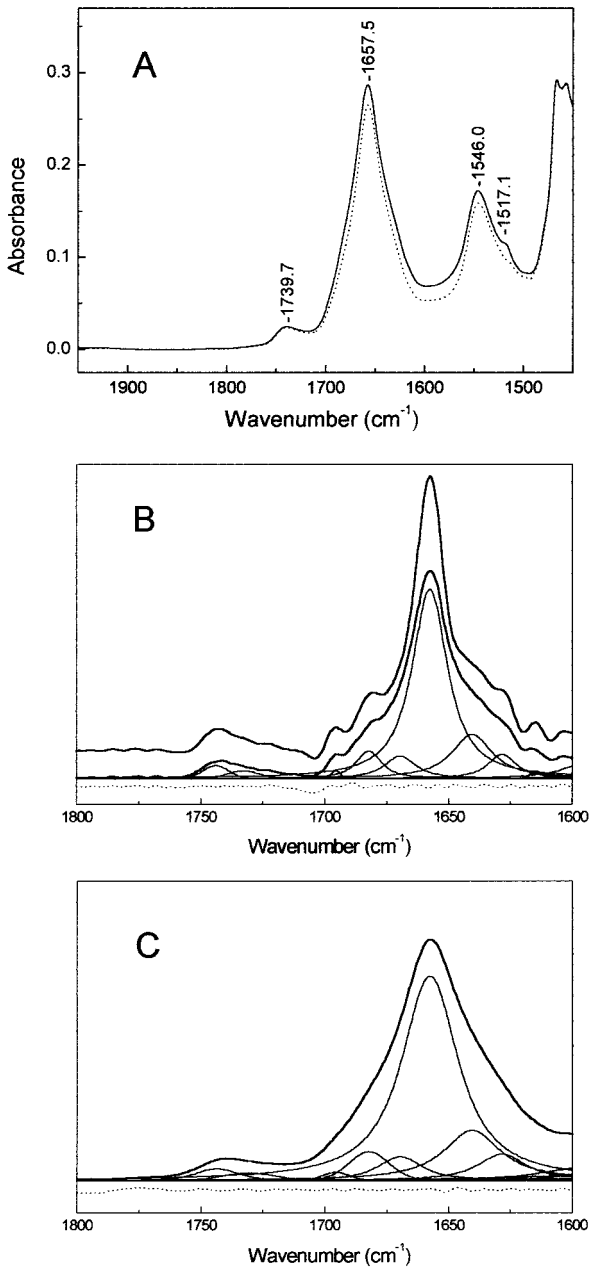

FIGURE 3: (A) (—) Transmission absorption spectrum of a dry film of the solubilized carboxyatractyloside-inhibited Anc2pHis at 25 °C. No buffer subtraction was performed. The noise standard deviation was 2×10^{-5} AU at 1850 cm^{-1}. At the amide I maximum (0.3 AU in the recorded spectrum) the calculated noise standard deviation was 4×10^{-5} AU, and the S/N was 7000. (···) Same spectrum after the synthetic amino acid side chain absorption spectrum was subtracted. (B) (—) Deconvolution of the spectra shown in (A) once the amino acid chain contribution, except that of tyrosine, has been removed. Top trace (shifted up for clarity): $\gamma' = 18$ cm^{-1}, $k = 2.5$, and Bessel apodization, giving a nominal resolution of 7.6 cm^{-1}. This spectrum was used to determine the number of bands. Down trace: $\gamma' = 12$ cm^{-1}, $k = 2.5$, and Bessel apodization, giving a nominal resolution of 5.0 cm^{-1}. This spectrum was curve fitted as described in Materials and Methods. The results of the fit are presented in Table 2. (···) Curve fit residual shifted down for a clearer display (at the same scale). (C) (—) Curve fit of the original spectrum shown in (A) once the amino acid side chain contribution (except that of tyrosine) has been removed. The fit was performed as described in Materials and Methods, giving as initial values the parameters from the spectra showed in (B). The results are presented in Table 2. (···) Curve fit residual multiplied by 20 and shifted down for a clearer display.

Table 2: Summary of the Curve Fit to the Deconvoluted Spectrum of a Dry Film of the Solubilized Carboxyatractyloside-Inhibited Anc2pHis (Figure 3B) and the Curve Fit to the Original Spectrum Shown in Figure 3C, Together with the Proposed Assignments for the Bands

deconvoluted		original				
position[a]	% area	position[a]	FWHH[b]	% L[b]	% area	assignment
1743.9		1743.7	19.1	40		phospholipid C═O
1732.8		1731.6	27.2	35		phospholipid C═O
1695.5	0.5	1696.1	12.2	10	0.8	β-sheets
1682.2	6.5	1682.5	19.7	10	5.2	reverse turns
1669.6	6.6	1669.6	20.5	75	5.3	reverse turns
1657.6	63.4	1657.7	27.1	95	64.6	α-helix + unordered
1640.5	16.7	1641.1	27.9	90	16.5	β-sheets
1628.4	6.3	1628.4	23.8	85	7.4	β-sheets
1614.8		1614.8	11.7	100		tyrosine

[a] In cm^{-1}. [b] The Voigt function used to fit the original spectrum, described by the parameters Lorentzian width and Gaussian width, is presented as its equivalent mixed Gaussian−Lorentzian profile with two parameters: FWHH in cm^{-1} and the percentage in height of the Lorentzian character (% L).

bands, while the other (down trace) was curve fitted. The best fitted bands are displayed in the same figure, and their parameters are presented in Table 2. Figure 3C presents the curve fit to the original spectrum, using as initial values those obtained from Figure 3B. Table 2 presents the results of the curve fit, together with the proposed assignments. The 1744 and 1732 cm^{-1} bands were assigned again to phospholipid. From the integrated absorption coefficient of the C═O group from egg PC, it was calculated that 18 ± 6 molecules of phospholipid remained bound per Anc2pHis dimer. The band at 1615 cm^{-1} was assigned to tyrosine following the results of Rahmelow et al. (*25*) and Chirgadze et al. (*33*). These authors reported an integrated absorption coefficient of 5×10^3 $mmol^{-1}$ cm^{-2}, whereas using the area of the curve fit in Figure 3C and taking into account 11 tyrosines per monomer, an integrated absorption coefficient of 6×10^3 $mmol^{-1}$ cm^{-2} was calculated. This good agreement for such a small band, although it is not fundamental in our study, shows the accuracy gained on working with dry film.

Table 4 collects the secondary structure estimation for the dry Anc2pHis film derived from curve fit of the deconvoluted spectra and curve fit of the original spectra. These data closely compare with the data from the sample in solution, presented in Table 4 as well. The estimation based on the original spectra agrees within 2−3%, whereas the estimation based on the deconvoluted spectra agrees within 3−8%. Furthermore, when individual bands are compared (Tables 1 and 2), the similitude is still remarkably good. It can be concluded that the structure of the carboxyatractyloside-inhibited Anc2pHis is well preserved in the film state. This is not surprising since some water always remains bound to the protein, even in a dry film. Moreover, DM has a sugar moiety, and sugars are often used to protect proteins against dryness (*38*).

Dry Film of the Reconstituted Anc2pHis. The good conservation of the secondary structure in the dry film of the solubilized Anc2pHis encouraged the extension of the work to dry films of the carrier reconstituted in phospholipids (egg PC/PA). The dry film of the reconstituted protein was

measured by FTIR-ATR spectroscopy, which facilitates sample preparation and H/D exchange experiments. However, FTIR-ATR can complicate the quantitative analysis of the spectra, since the spectra depend on film thickness (*15*) and sample orientation (*29*). First, we investigated if the film of the reconstituted Anc2pHis follows the thin or the thick film hypothesis. The ratio of the lipid C═O band (area over 1770−1710 cm^{-1}) to the acyl band (area over 3000−2800 cm^{-1}) obtained from the ATR spectrum was compared with a transmittance one. The resulting proportion, close to 1.0, indicates that the film follows the thin film hypothesis. Moreover, from the lipid-to-protein ratio and the integrated absorption coefficients of the egg PC acyl and carbonyl groups, the effective path length was calculated to be 0.5 μm for both bands. In contrast, the thick film hypothesis predicts a different path length for both bands (2.5 and 4.2 μm, respectively), supporting the conclusion that the sample is described by the thin film hypothesis.

Figure 4A shows the absorption spectrum of a dry film of the reconstituted carboxyatractyloside-inhibited Anc2pHis. This spectrum presents some differences with respect to that of Figure 3A, as the amide I and II maxima are shifted 1 cm^{-1} up and 0.3 cm^{-1} down, respectively, and the amide I/amide II intensity ratio is 1.81, higher than in the presence of detergent. These differences could be assigned to a different structure in the solubilized and reconstituted state, and/or a higher amount of residual water. It should be pointed out that an orientation effect, due to the alignment of the phospholipid bilayers parallel to the ATR crystal surface, with the roughly perpendicular orientation of the transmembrane α-helices, cannot explain the higher amide I/amide II intensity ratio for a thin film, as is the case (see Materials and Methods). Then, the contribution of remaining water to the spectrum was carefully examined. The amide A (3295 cm^{-1}) and remaining water (at 3550 cm^{-1}) can be observed without interferences. A wet film of egg PC was used to obtain the absorption from water molecules that remain bound in a film sample, concluding that the water band at 3400 cm^{-1} displayed the same width as in solution, and therefore the same absorption coefficient at the maximum can be expected (100 M^{-1} cm^{-1}). From this, an approximated absorption coefficient for water at 3550 cm^{-1} of 60 M^{-1} cm^{-1} was used. Taking $\epsilon_{amideI} = 370 \pm 30$ M^{-1} cm^{-1} and $\epsilon_{amideII} = 220 \pm 20$ M^{-1} cm^{-1}, 400−600 molecules of water were calculated to remain bound per Anc2pHis dimer (0.15 g of H_2O/g of Anc2pHis) in the dry film. This amount is enough to ensure hydration, even for many soluble proteins (*15*). The water band at 1645 cm^{-1} was estimated to have a height of only 0.006 AU (5% of amide I maximum) with an 80 cm^{-1} FWHH. After this correction the amide I/amide II intensity ratio became 1.73, suggesting structure differences with respect to the solubilized form.

Lipid−Protein Interactions in the Reconstituted Protein. Several spectroscopic tests were carried out to determine whether the reconstitution was successfully performed. The starting reconstitution mixture was prepared at a lipid-to-protein ratio (w/w) of 3.0. From the lipid C═O band area and the amide I and amide II height, it was determined that the lipid-to-protein ratio was between 3.0 and 2.5 (300−240 phospholipids per Anc2pHis dimer) so no significant amount of protein was lost during the purification, as this would give rise to an increase of the lipid-to-protein ratio.

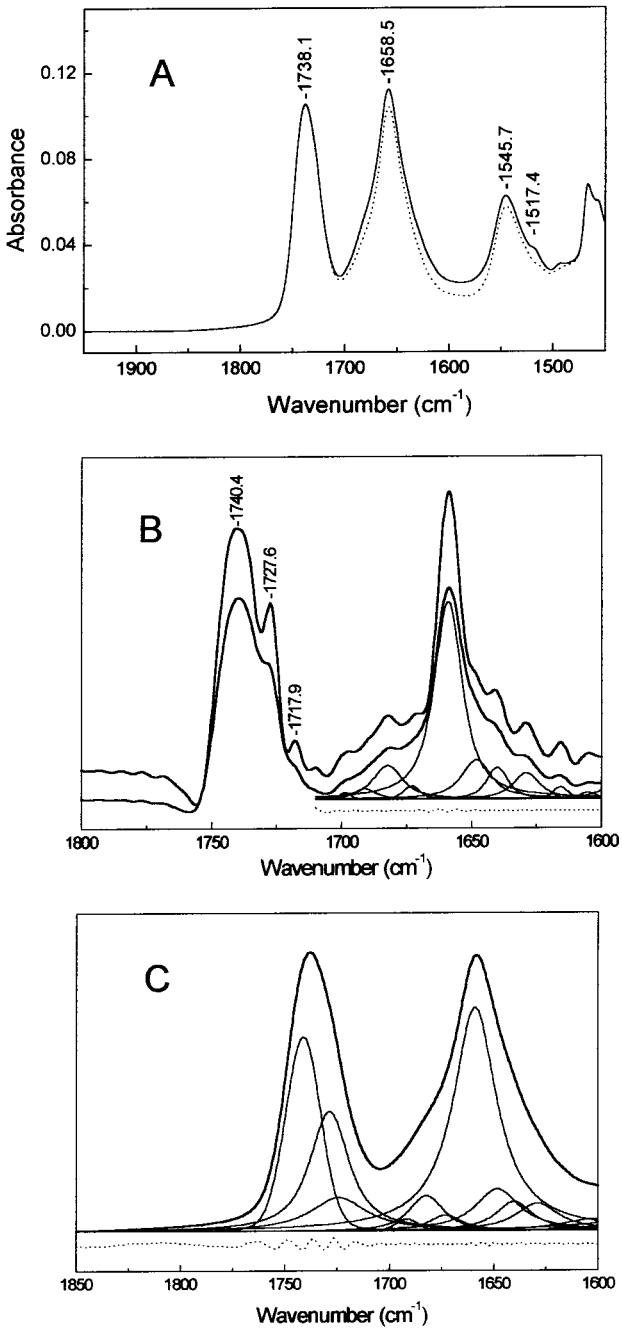

FIGURE 4: (A) (—) ATR spectrum of a dry film at 26 °C of the carboxyatractyloside-inhibited Anc2pHis reconstituted in egg PC/PA. The S/N at the amide I band maximum was 17 000. (···) Same spectrum after the synthetic amino acid side chain absorption spectra was subtracted. (B) (—) Deconvolution and curve fit of the spectra shown in (A) once the amino acid side chain contribution (except that of tyrosine) has been removed. Top trace (shifted for clarity): $\gamma' = 18$ cm^{-1}, $k = 3.0$, and Bessel apodization, giving a nominal resolution of 6.3 cm^{-1}. This spectrum was used to determine the number of bands. Down trace: $\gamma' = 14$ cm^{-1}, $k = 2.5$, and Bessel apodization, giving a nominal resolution of 5.9 cm^{-1}. This spectrum was curve fitted as described in Materials and Methods. The results of the fit are presented in Table 3. (···) Curve fit residual shifted down for clarity (at the same scale). (C) (—) Curve fit of the spectrum shown in Figure 3A once the amino acid side chain contribution (except that of tyrosine) has been removed. The fit was performed giving as initial values parameters derived from (B). Fit results are presented in Table 3. (···) Curve fit residual multiplied by 10 and shifted down for a clearer display.

We can also conclude that the protein−lipid mixture was preserved in the film attached to the ATR germanium surface.

To know if the protein was interacting with the lipids, we studied how the presence of the protein affects the phospholipid IR bands. Two phospholipid regions were investigated: the phospholipid antisymmetric and symmetric CH_2 stretching, which are sensitive to the gel-to-liquid crystal phase transition of the lipid, and the C═O stretching, sensitive to the hydrogen bonding and thus to the hydration state. Pure egg PC/PA in aqueous suspension is (at room temperature) in the liquid crystal phase, but it shifts to the gel phase when dried (gel-to-liquid transition in dry films occurs around 42 °C). We observed that, although the sample was dry, the CH_2 stretching bands corresponding to the sample in Figure 4A appear at 2923.4 and 2853.2 cm^{-1}, which are similar to those found for pure egg PC/PA in solution at room temperature: 2923.3 and 2853.1 cm^{-1} (spectra not shown). This can be explained considering that the interaction with the protein is driving the phospholipid to the liquid crystal phase, even in a dry film at room temperature. On the other hand, the phospholipid C═O stretching appears at 1738.1 cm^{-1}, similar to the value found for pure egg PC/PA in the dry state. However, deconvolution of this band (see Figure 4B) reveals at least three components, at 1740.4, 1727.6, and 1717.9 cm^{-1}. When deconvolution with the same parameters was applied to a dry film of pure egg PC/PA, only one band (1738.9 cm^{-1}) and a shoulder ($\approx$1730 cm^{-1}) were apparent, while a wet film gave two broad bands (1741.9 and 1730.2 cm^{-1}) (not shown). It can be concluded than the 1727.6 and 1717.9 cm^{-1} bands appearing in the reconstituted Anc2pHis film came from hydrogen bonding of the lipid C═O, probably to amino acid side chain residues of the protein, since some of these interactions (those giving rise to the 1717.9 cm^{-1} band) were very strong.

Secondary Structure Analysis of Dry Reconstituted Film: Curve Fit and Deconvolution. Figure 4B shows the results of the deconvolution of the spectrum in Figure 4A using two different sets of deconvolution parameters; the top trace was used to determine the number of bands, and the down trace was curve fitted (fitted bands are also presented). Figure 4C shows the curve fitting of the original spectrum. The results of both curve fittings are presented in Table 3, whereas the secondary structure estimation is presented in Table 4. Two effects could reduce the quality of secondary structure estimation: the remaining water and sample orientation. The effect of the remaining water in the curve fit results was analyzed for the deconvoluted spectrum shown in Figure 4B (down trace) by introducing in the fit a synthetic band representing the water contribution with all parameters fixed (see above). Only minor differences were observed when area results are compared band to band to those in Table 3. The secondary structure estimation changes to the following: reverse turns = 26.2%; β-sheets = 8.6%; α-helix + unordered = 65.2% (see Table 4 for a comparison). With respect to the orientation effect on the secondary structure estimation, only transmembrane α-helices are prone to be significantly oriented in dry film. From the literature, the order parameter for the amide I dipole transition moment of transmembrane α-helices of proteins with respect to the crystal surface normal usually obtained for an oriented sample ranges from $p = 0.35$ to $p = 0.2$ (*34*, *39*−*42*). If this orientation is accepted for the transmembrane helices of Anc2p, considering that they are predicted to account for 40% of the secondary structure, the results presented in Table 4 for the secondary structure estimation from the original spectrum should change to the following: reverse turns = 21%; β-sheets = 8.5%; α-helix + unordered = 70.5%; that means only slight differences.

Table 3: Summary of the Curve Fit to the Deconvoluted Spectrum of a Dry Film of the Reconstituted Carboxyatractyloside-Inhibited Anc2pHis (Figure 4B) and the Curve Fit to the Original Spectrum Shown in Figure 4C, Together with the Proposed Assignments for the Bands

deconvoluted		original				
position[a]	% area	position[a]	FWHH[b]	% L[b]	% area	assignments
1698.5	0.6	1699.4	9.8	0	0.4	β-sheet
1691.0	2.4	1691.7	12.9	0	1.2	reverse turns
1682.2	10.3	1682.3	19.5	80	7.2	reverse turns
1673.0	2.1	1673.1	19.0	100	3.3	reverse turns
1659.0	58.6	1659.1	25.2	100	61.7	α-helix + unordered
1648.1	12.3	1648.3	25.7	100	11.8	α-helix + unordered
1640.1	6.8	1640.3	21.1	100	6.8	β-sheets
1628.9	7.0	1629.1	25.0	100	7.6	β-sheets
1615.8		1616.1	12.3	90		tyrosine

[a] In cm^{-1}. [b] The Voigt function used to fit the original spectrum, described by the parameters Lorentzian width and Gaussian width, is presented as its equivalent mixed Gaussian−Lorentzian profile with two parameters: FWHH in cm^{-1} and the percentage in height of the Lorentzian character (% L).

Table 4: Estimated Secondary Structure Composition for the Carboxyatractyloside-Inhibited Anc2pHis in Three Different Physical States: Solubilized, Solubilized in Dry Film, and Reconstituted in Dry Film

	solubilized (%)[a]		solubilized (dry) (%)		reconstituted (dry) (%)	
secondary structure[b]	deconvoluted	original	deconvoluted	original	deconvoluted	original
reverse turns	17 ± 2	18.7 ± 1.3	25.6	21.4	27.7	22.6
β-sheets	18 ± 4	19.7 ± 0.6	15.2	16.4	8.9	9.5
α-helix + unordered	65 ± 2	61.6 ± 0.7	59.2	62.2	63.4	67.9

[a] For the solubilized form the data refer to two independent samples with its standard deviation. [b] It was considered that the different structures have different integrated absorption coefficients in the amide I region, following the relation reported by de Jong et al. (*35*) (β:α:turns 1:0.69:0.33), where unordered structures were included with α-helix structures. Results are presented from two data sources: deconvoluted and original spectrum (see Tables 1−3).

Two important changes are visible in the dry film of the reconstituted carboxyatractyloside-inhibited Anc2pHis, compared to the dry film of the solubilized protein: a shift of the main band from 1657.7 cm^{-1} in the solubilized to 1659.1 cm^{-1} in the reconstituted form and a new band at 1648 cm^{-1}, with the 1640 cm^{-1} band reducing significantly its area and its width. The secondary structure estimation (Table 4) also reflects these differences, with reduction of β-sheet structures and increase of α-helix and/or unordered structures. The reconstituted spectrum showed a much higher S/N, allowing a higher narrowing factor (and final nominal resolution) than that used for the solubilized sample ($k = 3$ vs $k = 2.5$). These differences in the deconvolution parameters might be the reason for resolving a new band at 1648 cm^{-1}. When applying to the reconstituted sample the narrowing factor

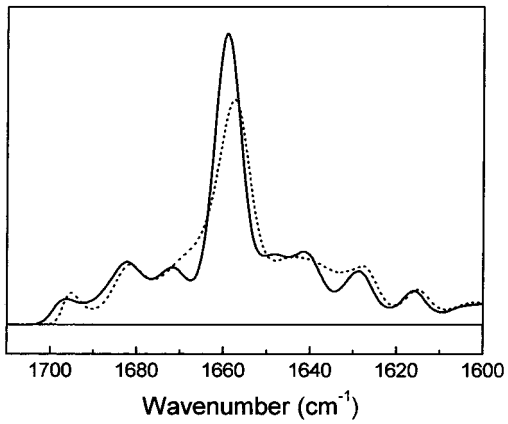

FIGURE 5: Amide I of the carboxyatractyloside-inhibited Anc2pHis in (···) dry solubilized form and (—) dry reconstituted form, after nonlinear deconvolution using a maximum likelihood algorithm with $\gamma' = 20$ cm^{-1} (Lorentzian). Both spectral areas were normalized between 1710 and 1600 cm^{-1}.

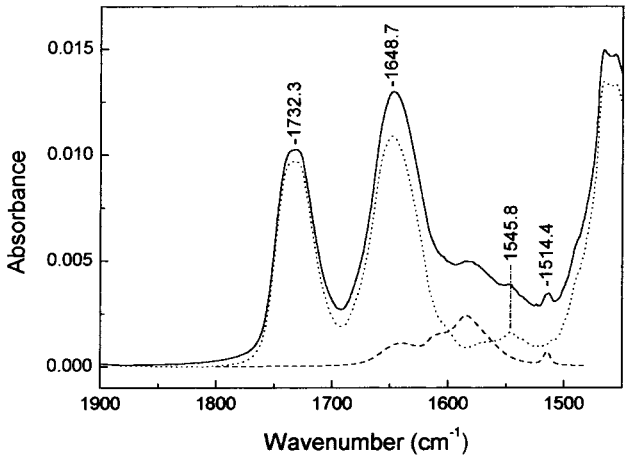

FIGURE 6: (—) ATR spectrum of a wet film of reconstituted carboxyatractyloside-inhibited Anc2pHis after 15 h of H/D exchange. The S/N at the amide I maximum was 2200. (···) Same spectrum after the amino acid side chain spectrum and the D_2O contribution were subtracted. (- - -) Synthetic deuterated amino acid side chain absorption calculated from the data reported by Chirgadze et al. (*25*).

originally used with the solubilized one, the 1648 cm^{-1} band was not completely resolved, appearing only as a faint shoulder. To solve this problem, both spectra were deconvoluted with a nonlinear deconvolution algorithm (maximum likelihood restoration) in which the differences in S/N are not as critical as in Fourier self-deconvolution and identical parameters for both spectra could be used. Both deconvoluted spectra are presented in Figure 5, where it can be confirmed that the appearance of a new band at 1648 cm^{-1} is not a noise-induced difference, thus confirming the structural differences between reconstituted and solubilized samples.

Hydrogen−Deuterium Exchange of Reconstituted Anc2pHis in Wet Film. Figure 6 shows the ATR spectrum of a wet film of the reconstituted carboxyatractyloside-inhibited Anc2pHis after 15 h of H/D exchange. The water concentration in the D_2O wet film and the path length can be calculated from the 2500 cm^{-1} D_2O band ($\epsilon_{2500} = 74.5$ M^{-1} cm^{-1}) and the C═O lipid band (see above). The effective path length was 1.2 μm at 1740 cm^{-1}, water concentration 40 M, and Anc2pHis concentration in the film around 80 mg/mL. These values show that the film is well hydrated.

Table 5: Summary of the Curve Fit to the Deconvoluted Spectrum and to the Original Spectrum of the Deuterated Reconstituted Carboxyatractyloside-Inhibited Anc2pHis Shown in Figure 6

deconvoluted		original		
position[a]	% area	position[a]	% area	assignments[b]
1680.0	1.6	1679.9	2.9	2.5% D-reverse turns + 0.4% D-β-sheets
1669.0	8.4	1668.6	7.3	7.3% D-reverse turns
1659.2	13.5	1659.1	13.7	11.8% H-α-helix + 1.9% D-reverse turns
1650.3	30.3	1650.3	30.9	30.9% D-α-helix (from 1659)
1640.7	21.2	1640.7	20.7	19% D-unordered (from 1659) + 1.7% H-β-sheets
1632.5	17.3	1632.5	17.4	11.8% D-unordered (from 1648) + 5.6% D-β-sheets
1623.4	7.7	1623.3	7.1	7.1% D-β-sheets
1612.5		1612.7		tyrosine

[a] In cm^{-1}. [b] The D prefix refers to a deuterated structure and the H prefix to a hydrogenated one (nonexchanged). For more information about how the assignments were performed, see the text.

In the exchanged spectrum the amide I′ maximum was shifted 10 cm^{-1} down, and the amide II intensity was strongly reduced, showing extensive exchange of the amide hydrogen atoms. The synthetic deuterated amino acid side chain spectrum was subtracted, being the scaling factor that needed to eliminate the tyrosine band (highly resolved in the deuterated form). After this operation the residual amide II became apparent. The maximum of residual II (1546 cm^{-1}) suggests that nonexchanged amide hydrogens are in α-helix structures. The percentage of nonexchanged amide hydrogens was determined from the relation between the amide II to amide I area ratio after and before deuteration, once the amino acid side chain contribution was subtracted. Notice that as both amide II and amide I bands come from the same chemical group and are close together in the spectrum, the amide II to amide I ratio corrects itself for any swelling of the film (*15*). It was determined (testing two different integration intervals for the amide II) that 13−20% of the amide hydrogens remained not exchanged after 15 h in the presence of D_2O vapor. We want to stress that amino acid side chain absorption was previously subtracted before the level of exchange was determined; otherwise, nonsense results would be obtained, since the area integrated under the amide II interval would gave negative values, leading to apparently more that 100% exchange.

The amide I of this corrected spectrum was analyzed by deconvolution and curve fit, as those spectra of Figure 3A and 4A (not shown). First, bands were identified in a spectrum deconvolved with $\gamma' = 18$ cm^{-1} and $k = 2.6$, and these bands where fitted in a spectrum deconvolved with $\gamma' = 14$ cm^{-1} and $k = 2.2$. The obtained results about number, position, and width of bands were used as initial values for a curve fit in the original amide I. Table 5 shows the curve fit results. The assignments were done following four premises: when completely deuterated, amide I bands should be shifted down about 5 cm^{-1} for β-sheets (*10*), about 10 cm^{-1} for α-helices (*10*), and between 15 and 20 cm^{-1} for unordered structures (*7*); the secondary structure assignments must show coherence to those in H_2O; about 15% of the amide I area should not be shifted (as is not exchanged) being this area mainly in α-helix bands; and unordered structures and reverse turns should be completely exchanged.

The assignments in Table 5 fulfill the criteria we imposed: the areas assigned to α-helix + unordered, to β-sheets, and to reverse turn structures are the same as in H_2O; the area assigned to nonexchanged structures represents 14% of the amide I area; 90% of the nonexchanged structures belongs to α-helix; and the exchanged α-helix shifted about 9 cm^{-1}, the exchanged β-sheets shifted 7.5−5.5 cm^{-1}, and unordered structures shifted between 18.5 and 15.5 cm^{-1}. Reverse turns showed an exchange-induced shift between 14 and 11 cm^{-1}. Table 5 assignments allow discriminating between α-helix and unordered contributions; thus the amide I area assigned to the different secondary structures becomes 44.4% α-helix, 29.1% unordered, 14.8% β-sheets, and 11.7% reverse turns. When the extinction coefficients proposed for the different secondary structures are used (*35*), the secondary structure estimation becomes 33.1% α-helix, 39.3% unordered, 7.6% β-sheets, and 20.0% reverse turns. The α-helix percentage is in this case lower than expected for the proposed 6 spanning membrane α-helices. A 44.4% percentage is consistent with up to 6.5 spanning membrane α-helices, but 33.1% is consistent with a maximum of 5 spanning membrane α-helices. This last value could be increased if an orientation of the transmembrane α-helix similar to that described in the literature was considered, to a final percentage ranging between 40% and 36%, and thus approaching the proposed 6 spanning membrane α-helices.

The structure assignment done with the D_2O-exchanged film allows discriminating between both bands assigned to α-helix + unordered structures in Table 3. Thus, most likely the 1648 cm^{-1} band comes completely from unordered structures and the 1659 cm^{-1} comes mainly from α-helix, although with an important unordered contribution.

DISCUSSION

We present in this paper an infrared spectroscopy study of the carboxyatractyloside-inhibited mitochondrial ADP/ATP transporter purified from the yeast *S. cerevisiae*. The carboxyatractyloside is noncovalently bound to the transporter with very high affinity, blocking it into a defined and probably functionally important conformation of the transporting cycle (*1*). Indirect evidence of an actual binding of the inhibitor to the protein was obtained from intrinsic fluorescence and FTIR studies (data not shown). When the solubilized inhibited form was heated, an intrinsic fluorescence transition was observed in which the fluorescence strongly increased. Because binding of the inhibitor to the solubilized protein decreases the intrinsic fluorescence (*17*), we interpreted that the fluorescence transition is caused by the release of the inhibitor from the protein. More importantly, this transition was not present when the Anc2pHis was isolated in the absence of inhibitor. Moreover, the free protein showed in the FTIR spectra very intense aggregation bands, not evident in the inhibited form.

The carboxyatractyloside-inhibited Anc2pHis has been studied in three states: solubilized in solution and in dry film and reconstituted in dry film. For all of these states, a minimum of 60% and a maximum of 70% of the protein are predicted to be in a helix conformation and/or adopting unordered structures. This percentage is consistent with the predicted six transmembrane helices that would account for 40% of the secondary structure (*36*) and allow between one-third and one-half of the topological loops to adopt helix and/or unordered structures. For the reconstituted protein, spectra deconvolution after H/D exchange experiments allows discriminating between α-helix and unordered structures. Thus, it can be concluded that the band at 1659 cm^{-1} accounts for 5−6.5 transmembrane helices. Although this result does not indicate exactly the number of helices, it is in keeping with the predicted six transmembrane helices.

Starting from the solubilized state (studied by transmittance), we found very small changes in the amount of secondary components on drying the protein. Moreover, the individual bands determined by deconvolution showed only small differences. This suggested to us to work with dry films for the reconstituted sample. The possible sources of errors on working with films, such as changes of structure upon dehydration, remaining water contribution to the amide I, and sample orientation, were carefully analyzed. It can be concluded that these errors do not significantly alter the secondary structure estimation. The preservation of the essential secondary structure of the Anc2p carrier in dry films is an important observation. This finding supports the extension of the structural studies to film preparations and controlled dry systems to investigate more subtle interactions, like H/D exchange, substrate binding, or the role of lipid environment.

When the amide I band for the reconstituted and the solubilized carboxyatractyloside-inhibited Anc2pHis is compared, some differences can be observed: first, some changes in the bands assigned to turns, second, the main band appears at different positions (1659.1 and 1657.7 cm^{-1}, respectively), and third, the main difference is the appearance of one band at 1648 cm^{-1}, with the concomitant decrease of the band at 1640 cm^{-1}. Using a nonlinear deconvolution algorithm to confirm these observations, we were able to discard any fictitious origin of these changes that could be due to differences in the parameters used in deconvolution. Assigning the 1648 cm^{-1} band to unordered structures, then the structural differences caused by the change from a detergent to a lipid environment are a decrease of β-sheets with an increase of unordered structures. This change involves 6−10% of the amino acids (20−30 residues). It can be concluded that the presence of phospholipids around the Anc2p polypeptide modulates the secondary conformation of the carrier, at least as compared with the conformation found in the detergent-solubilized form. Moreover, the lipid-induced changes were accompanied by protein-induced changes into the lipid environment. On one hand, the lipids present in the dry film of reconstituted Anc2pHis were in the gel state, whereas those of a dry film of pure egg PC/PA mixture were in the liquid crystal state. Additionally, the lipids in the reconstituted sample showed a stronger hydrogen bonding in the C═O groups, probably to some residues of the protein. These findings indicate that, after reconstitution and film preparation, an extensive contact between the transporter and the lipid molecules is achieved. Moreover, it can be suggested that the phospholipid environment has some role in the maintenance of the native conformation of the carrier in the mitochondrial membrane.

Hydrogen/deuterium exchange experiments were carried out in the reconstituted carboxyatractyloside-inhibited Anc2pHis. Most of the amide hydrogens were exchanged in 15 h (85%), and the remaining (about 50 amino acids)

were in α-helix structures, probably in transmembrane helices. This high percentage of exchange is roughly similar to the observed exchange of other α-helical transmembrane carriers of hydrophilic substrates such as the glucose erythrocyte carrier (85%) (*43*), the lactose permease from *E. coli* (100%) (*44*), or the melibiose permease from *E. coli* (80%) (*45*). These values are in clear contrast with those reported for aqueous channels as the *β*-structured porin from *E. coli* (35%) (*46*), the transmembrane α-helix aquaporin-1 from human erythrocyte (40%) (*47*), and the aerolysin from *Aeromonas hydrophila* (30%) (*48*), and for the transmembrane α-helix retinal proteins, which show less than 33% exchange (*47*, *49*). However, it should be mentioned that for the Anc2pHis the percentage of exchange has been calculated after correction for a full exchange of side chain protons, and many of the cited papers did not do so. For the Anc2pHis, this correction reduced the apparent observed exchange from about 100% to 85% and should be taken into account when comparing the degree of accessibility of different proteins. Assuming that the six transmembrane helical model is correct, the 85% exchange means that, in the carboxyatractyloside-inhibited form of Anc2p, not only the loops going out of the membrane but most of transmembrane helix peptide bonds (about 60% of them) are exchanged. This result implies that, even in that functionally blocked conformation of the carrier, most of the transmembrane helices are readily accessible to water molecules and show enough conformational flexibility to allow the observed amount of exchange.

Finally, it should be noted that, to carry out the secondary structure estimation, we introduced for the first time to our knowledge the use of Voigt bands to fit the deconvoluted spectra. This provides a close approximation to any band shape distortion caused by deconvolution. Tests made with synthetic amide I composed of pure Lorentzian bands showed the suitability of this approach to recover close estimations of area, position, and original width of the underlying bands (to be published). For synthetic amide I composed of bands with Lorentzian−Gaussian character, good results were obtained by performing a final fit to the original spectrum, starting from the parameters obtained by fitting a deconvolved spectrum.

REFERENCES

1. Fiore, C., Trézéguet, V., Le Saux, A., Roux, P., Schwimmer, C., Dianoux, A. C., Noël, F., Lauquin, G. J.-M., Brandolin, G., and Vignais, P. V. (1998) *Biochimie 80*, 137−150.
2. Adrian, G. S., McCammon, M. T., Montgomery, D. L., and Douglas, M. G. (1986) *Mol. Cell. Biol. 6*, 626−634.
3. Lawson, J. E., and Douglas, M. G. (1988) *J. Biol. Chem. 263*, 14812−14818.
4. Kolarov, J., Kolarova, N., and Nelson, N. (1990) *J. Biol. Chem. 265*, 12711−12716.
5. O'Malley, K., Pratt, P., Robertson, J., Lilly, M., and Douglas, M. G. (1982) *J. Biol. Chem. 257*, 2097−2103.
6. Drgon, T., Sabova, L., Nelson, N., and Kolarov, J. (1991) *FEBS Lett. 289*, 159−162.
7. Arrondo, J. L., Muga, A., Castresana, J., and Goñi, F. M. (1993) *Prog. Biophys. Mol. Biol. 59*, 23−56.
8. Goormaghtigh, E., Cabiaux, V., and Ruysschaert, J. M. (1994) *Subcell. Biochem. 23*, 329−362.
9. Goormaghtigh, E., Cabiaux, V., and Ruysschaert, J. M. (1994) *Subcell. Biochem. 23*, 405−450.
10. Krimm, S., and Bandekar, J. (1986) *Adv. Protein Chem. 3*, 181−364.
11. Venyaminov, S. Y., and Kalnin, N. N. (1990) *Biopolymers 30*, 1259−1271.
12. Bandekar, J. (1992) *Biochim. Biophys. Acta 1120*, 123−143.
13. Kauppinen, J. K., Moffatt, D. J., Mantsch, H. H., and Cameron, D. G. (1981) *Appl. Spectrosc. 35*, 271−276.
14. Byler, D. M., and Susi, H. (1986) *Biopolymers 25*, 469−487.
15. Goormaghtigh, E., Raussens, V., and Ruysschaert, J. M. (1999) *Biochim. Biophys. Acta 1422*, 105−185.
16. Klingenberg, M., Winkler, E., and Huang, S. (1995) *Methods Enzymol. 260*, 369−389.
17. Brandolin, G., Le Saux, A., Trézéguet, V., Vignais, P. V., and Lauquin, G. J.-M. (1993) *Biochem. Biophys. Res. Commun. 192*, 143−150.
18. Le Saux, A., Roux, P., Trézéguet, V., Fiore, C., Schwimmer, C., Dianoux, A.-C., Vignais, P.-V., Brandolin, G., and Lauquin, G.-J.-M. (1996) *Biochemistry 35*, 16116−16124.
19. Heidkämper, D., Müller, V., Nelson, D. R., and Klingenberg, M. (1996) *Biochemistry 35*, 16144−16152.
20. Fiore, C., Trézéguet, V., Roux, P., Le Saux, A., Noël, F., Schwimmer, C., Arlot, D., Dianoux, A.-C., Lauquin, G. J.-M., and Brandolin, G. (2000) *Protein Expression Purif. 19*, 57−65.
21. Daum, G., Bohni, P. C., and Schatz, G. (1982) *J. Biol. Chem. 257*, 13028−13033.
22. Krämer, R., and Klingenberg, M. (1979) *Biochemistry 18*, 4209−4215.
23. Smith, P. K., Krohn, R. I., Hermanson, G. T., Mallia, A. K., Gartner, F. H., Provenzano, M. D., Fujimoto, E. K., Goake, N. M., Olson, B. J., and Klenk, D. C. (1985) *Anal. Biochem. 150*, 76−85.
24. Venyaminov, S. Y., and Kalnin, N. N. (1990) *Biopolymers 30*, 1243−1257.
25. Chirgadze, Y. N., Fedorov, O. V., and Trushina, N. P. (1975) *Biopolymers 14*, 679−694.
26. Rahmelow, K., and Hübner, W. (1997) *Appl. Spectrosc. 51*, 160−170.
27. Carter, R. O., III, Lindsay, N. E., and Beduhn, D. (1990) *Appl. Spectrosc. 44*, 1147−1151.
28. Venyaminov, S. Y., and Prendergast, F. G. (1997) *Anal. Biochem. 248*, 234−245.
29. March, D. (1999) *Biophys. J. 77*, 2630−2637.
30. Kauppinen, J. K., Moffatt, D. J., Mantsch, H. H., and Cameron, D. G. (1981) *Anal. Chem. 53*, 1545−1457.
31. Griffihs, P. R., Pierce, J. A., and Hongin, G. (1987) in *Computer-Enhanced Analytical Spectroscopy* (Meuzelaar, H. L. C., and Isenhovic, T. L., Eds.) pp 29−54, Plenum Press, New York.
32. Cameron, D. G., and Moffat, D. J. (1984) *J. Test. Eval. 12*, 78−85.
33. Rahmelow, K., Hübner, W., and Ackermann, T. (1998) *Anal. Biochem. 257*, 1−11.
34. Tamm, L. K., and Tatulian, S. A. (1997) *Q. Rev. Biophys. 30*, 365−429.
35. de Jongh, H. H. J., Goormaghtigh, E., and Ruysschaert, J. M. (1996) *Anal. Biochem. 242*, 95−103.
36. Müller, V., Basset, G., Nelson, D. R., and Klingenberg, M. (1996) *Biochemistry 35*, 16132−16143.
37. Forato, L. A., Bernardes-Filho, R., and Colnago, L. A. (1998) *Anal. Biochem. 259*, 136−141.
38. Carpenter, J. F., and Crowe, J. H. (1989) *Biochemistry 28*, 3916−3922.
39. Earnest, T. N., Herzfeld, J., and Rothschild, K. J. (1990) *Biophys. J. 58*, 1539−1546.
40. Nabedryk, E., Tiede, D. M., Dutton, P. L., and Breton, J. (1982) *Biochim. Biophys. Acta 682*, 273−280.
41. Bazzi, M., and Woody, R. W. (1985) *Biophys. J. 48*, 957−966.
42. LeCoutre, J., Narasimhan, L. R., Patel, H. R., and Kaback, H. R. (1997) *Proc. Natl. Acad. Sci. U.S.A. 94*, 10167−10171.
43. Alvarez, J., Lee, D. C., Baldwin, D., and Chapman, D. (1987) *J. Biol. Chem. 262*, 3502−3509.
44. Patzlaff, J. S., Moeller, J. A., Barry, B. A., and Brooker, R. J. (1998) *Biochemistry 37*, 15363−15375.

45. Dave, N., Troullier, A., Mus-Veteau, I., Duñach, M., Leblanc, G., and Padrós, E. (2000) *Biophys. J. 79*, 747−755.
46. Kleffel, B., Garavito, R. M., Baumeinster, W., and Rosenbusch, J. P. (1985) *EMBO J. 4*, 1589−1592.
47. Cabiaux, V., Oberg, K. A., Pancoska, P., Walz, T., Agre, P., and Engel, A. (1997) *Biophys. J. 73*, 406−417.
48. Cabiaux, V., Buckley, J. T., Wattiez, R., Ruysschaert, J.-M., Parker, M. W., and van der Goot, F. (1997) *Biochemistry 36*, 15224−15232.
49. Rath, P., DeGrip, W. J., and Rothschild, K. J. (1998) *Biophys. J. 74*, 192−198.

BI010091S

Fourier Deconvolution in Non-self-deconvolving Conditions. Effective Narrowing, Signal-to-Noise Degradation, and Curve Fitting

VÍCTOR A. LÓRENZ-FONFRÍA, JOAQUIM VILLAVERDE, and ESTEVE PADRÓS*

Unitat de Biofísica, Departament de Bioquímica i de Biologia Molecular, Facultat de Medicina, Universitat Autònoma de Barcelona, 08193 Bellaterra, Barcelona, Spain

The effect of Fourier deconvolution on band narrowing and on the decrease of signal-to-noise ratio has been studied for a generalized case in which the width used in the deconvolution does not match the actual bandwidth. For the identification of underlying component bands, our results show that application of infra-deconvolution (i.e., the bandwidth used for deconvolution is lower than the actual bandwidth) produces a high degradation of the signal-to-noise ratio and poor band narrowing. On the contrary, self- or over-deconvolution, with lower signal-to-noise degradation and higher band narrowing, seem more suitable for this purpose. Relative to quantitative analysis, we rely on both theoretical and practical aspects to propose the generalized use of Voigt band shapes as a fairly correct general model to be used in the curve fitting of deconvoluted bands. With its use, the curve fitting of noise-free deconvoluted bands retrieved the original band parameters with high accuracy. The noise effect on the parameter precision obtained by curve fitting a deconvoluted noisy Lorentzian band was also studied. Finally, the existence of optimum deconvolution parameters for curve fitting complex spectra is considered, and a general recommendation for approaching this optimum is given.

Index Headings: **Resolution enhancement; Deconvolution; Curve fitting; Infrared; Band shape; Spectral quantification; Voigt bands.**

INTRODUCTION

Fourier deconvolution (FD) was introduced in the mathematical treatment of infrared (IR) spectra in the early eighties by the Ottawa group,[1–3] and since then it has become a standard tool in IR spectroscopy, allowing the resolution of overlapped bands. The band-narrowing effect of FD has proved to be of great utility when proteins are studied by IR spectroscopy.[4] This narrowing effect is not exclusive to FD but is shared by other methods.[5–11]

Important information about protein structure can be obtained through the analysis of the amide I band (1700–1610 cm^{-1}), coming mainly from the C=O stretching of the peptide bond (amide group).[12] Both experimental and theoretical studies have shown the existence of a correlation between amide I band position and secondary structure,[12–14] and several guides to assign secondary structure from the position of the amide I components have been published.[15,16]

For a peptide with pure repetitive structure, the amide I will be composed of as many bands as amide groups, with maxima showing slight differences caused by small heterogeneities, and therefore behaving as a single band. This band will often appear split due to transition dipole coupling; this split is only important for antiparallel β-sheets.[12]

For proteins, where more than one pure structure is always present, only bands coming from similar structures will be centered around the same position. This will give rise to a more important band heterogeneity, based not only on subtle environmental differences but also on structural differences. Although this heterogeneity can account for several tenths of cm^{-1}, it is only visible as an asymmetry on the amide I envelope band due to the intrinsic linewidth of amide I bands and the number of structures present in proteins.

The usefulness of FD in IR conformational studies of proteins is twofold. First, by its use we aim to narrow the amide I bands enough, not to resolve all of them, but to the main position where they are centered. Generally, these main positions will correlate with types of secondary structures. Its success will depend on the narrowing effect of FD and on how the signal-to-noise ratio is degraded in this process. This topic has been studied for the self-deconvolution case (i.e., when bands are deconvoluted by their precise bandwidth and band shape).[2] In general, and especially working with proteins, it is not possible to match the self-deconvolution case, and therefore, we have extended previous theoretical work[2] to include infra-deconvolution and over-deconvolution (i.e., when a band is deconvoluted by its band shape, but with lower or higher bandwidth).

The second utility of FD comes from the need for quantitative analysis of the amide I bands in order to estimate protein secondary structure. For this use, deconvoluted spectra have to be used as a starting point for another mathematical tool, such as curve fitting. Curve fitting is not a trivial process, and several conditions are necessary for its success. One of these is the use of the correct type of bands. The use of Gaussian bands to fit deconvoluted spectra, together with Lorentzian and mixed Gaussian–Lorentzian bands (with an arbitrary weight) has become the rule up to the moment,[4,17,18] although it was early stated that after deconvolution, a Lorentzian band should be expressed as the convolution of some Lorentzian band with the apodization used in the deconvolution.[19] Recently, analytical expression for this convolution has been presented for several apodization functions,[20] although its practical use has been mostly prevented by its complexity. We will show that Voigt bands, included in most commercial fitting programs for spectroscopy, can be a good approximation to deconvoluted bands, and thus, their use can be valuable.

Received 9 May 2001; accepted 28 September 2001.
* Author to whom correspondence should be sent.

0003-7028/02/5602-0232$2.00/0

METHODS

Fourier deconvolution was performed using the program supplied by Spectrum Square Associates, Inc., implemented in the GRAMS software (Galactic Industries). The deconvoluted interval was chosen broad enough to avoid any distortions in the obtained spectra.[20] Curve fitting was performed by a least-squares minimization using the Levenberg–Marquard algorithm.[21] White normal noise was obtained from the pseudo-normal random generator included in the ORIGIN software (Microcal Software, Inc.).

THEORETICAL BACKGROUND

Fourier Self-Deconvolution. Let us consider an infrared spectrum $E(\nu)$ that for simplicity contains one single band centered at a wavenumber ν_0, with area A. This spectrum can be represented as the convolution of a narrow band (Dirac δ as a limit, centered at ν_0, with amplitude equal to the area) with the line shape function of the band $L(\nu)$ and with the line shape function of the instrument $R(\nu)$, i.e.,

$$E(\nu) = A\delta(\nu - \nu_0) \otimes L(\nu) \otimes R(\nu) \quad (1)$$

where $\otimes$ represents convolution. $L(\nu)$ sum the homogeneous and inhomogeneous broadening,[22] and $R(\nu)$ the instrumental broadening. If both types of spectrum broadening could be removed, a band without width (perfectly narrow) would be obtained. In IR spectroscopy of solid and liquid phases, the instrumental broadening is often of low significance compared with the homogeneous and inhomogeneous broadenings; thus, a band can be notably narrowed by means of just inverting the $L(\nu)$ convolution, i.e., $L(\nu)$ deconvolution. Deconvolution of $L(\nu)$ can be obtained in the Fourier domain, where convolution is simply a multiplication and deconvolution simply a division. The Fourier pairs of a function X will be expressed as $X(x) \Leftrightarrow X(\nu)$, where x is distance and ν is wavenumber. In the Fourier domain, Eq. 1 can be reexpressed as:

$$\begin{aligned} E(x) &= \Im^{-1}\{E(\nu)\} \\ &= \Im^{-1}\{A\delta(\nu - \nu_0)\}\Im^{-1}\{L(\nu)\}\Im^{-1}\{R(\nu)\} \end{aligned} \quad (2)$$

where $\Im^{-1}$ represents the inverse Fourier transform. The $L(\nu)$ Fourier pair, $L(x)$, is a continuous decreasing function, and the $R(\nu)$ Fourier pair, $R(x)$, is usually a triangular apodization function for Fourier transform infrared spectroscopy (FT-IR).[23] $R(x)$ becomes zero for $x > x_f$, where $1/x_f$ results in the instrumental nominal resolution.[23]

Deconvolution of Eq. 1 by $L(\nu)$ can be obtained by dividing $E(x)$ by $L(x)$, and performing their Fourier transform. This gives the so-called Fourier self-deconvoluted spectrum $E'(\nu)$, where the bandwidth is only limited by the instrumental resolution:

$$E'(\nu) = \Im\{E(x)/L(x)\} = A\delta(\nu - \nu_0) \otimes R(\nu) \quad (3)$$

This solution is not always acceptable. Deconvolution is a difficult problem, and the presence of noise in $E(\nu)$, or even the limited dynamic range of the computational process can result in a calculated deconvoluted spectrum $E'(\nu)$ different from the ideal one. To give a solution to these problems, Kauppinen et al.[1] introduced a decreasing function, $D(x)$, multiplying $E(x)$ in Eq. 3. This function acts as a new instrumental function, thus controlling the resulting band shape in Eq. 3 and improving the stability of the solution by decreasing the final instrumental nominal resolution. The properties of $D(x)$ are similar to those of $R(x)$. $D(x)$ becomes zero for $x > l$ (l is called the cut-point) and goes to zero before $R(x)$ does ($l < x_f$), so the effect of $R(x)$ on the final band shape is negligible and would not be taken into account. The new nominal resolution in the deconvoluted spectra is thus $1/l$. Now Eq. 3 becomes:

$$E'(\nu) = \Im\{E(x)D(x)/L(x)\} = A\delta(\nu - \nu_0) \otimes D(\nu) \quad (4)$$

where $D(\nu)$ controls the final band shape and the width of the deconvoluted band. At the same time, the band shape and width of the original band is approximately given by $L(\nu)$. The narrowing obtained (k) is thus:

$$k = \frac{FWHH[E(\nu)]}{FWHH[E'(\nu)]} \cong \frac{FWHH[L(\nu)]}{FWHH[D(\nu)]} \quad (5)$$

where FWHH is full width at half-height.

Fourier self-deconvolution (FSD) is only a special case of Fourier deconvolution (FD), where the $L(\nu)$ convolution is completely inverted. The properties of the more general Fourier deconvolution are the following: the area and position of a band are conserved after its application, but the width, shape, and height are affected.[24] Being a linear process, conclusions on its application to a band can be directly extended to multiple overlapping bands and to the presence of noise. Finally the deconvoluted spectrum $E'(\nu)$ is normally obtained at a lower instrumental resolution than the original spectrum $E(\nu)$.[1] The consequence of this lower resolution is that some information is lost during FD because $D(x)$ removes data (and noise) above l. In addition, it is important to point out that as data from $E(x)$ are removed above l by $D(x)$, it is indifferent to whether these data were or were not acquired. If a spectrum will only be processed by FD, the nominal resolution ($1/x_f$) at which it is acquired should be accordingly adjusted to make x_f only slightly higher than l.

Fourier Self-Deconvolution for a Lorentzian Band. For most IR bands, the line broadening $L(\nu)$ function can be approximated to a Lorentzian band shape with FWHH equal to γ.[23] To remove this broadening from the spectrum $E(\nu)$, Eq. 4 should be applied, where $D(x)$ should be appropriately chosen and $L(x)$ is given by the Fourier transform of a Lorentzian band shape. Then, according to Eq. 4, a band with the original area and position and the band shape of $D(\nu)$ is obtained. The narrowing obtained will be equal to $a \times \gamma \times l$, where $(a \times l)^{-1}$ is the FWHH of $D(\nu)$ (a is close to one). Values for a were given for several filters by Kauppinen et al.[2] and by Marshall and Verdun.[25] For example, a is equal to 0.985 for a truncated Gaussian filter and equal to 1.05 for a Bessel filter. For practical reasons, the use of the k instead of l as an input parameter in FD is often preferred, although not by all users.[18]

Fourier Deconvolution for Lorentzian Bands. Until this point it was supposed that the line-broadening $L(\nu)$ function can be known and furthermore, that in the case of a multiple-band spectrum this line-broadening width is common to all bands. When this is not the case, line

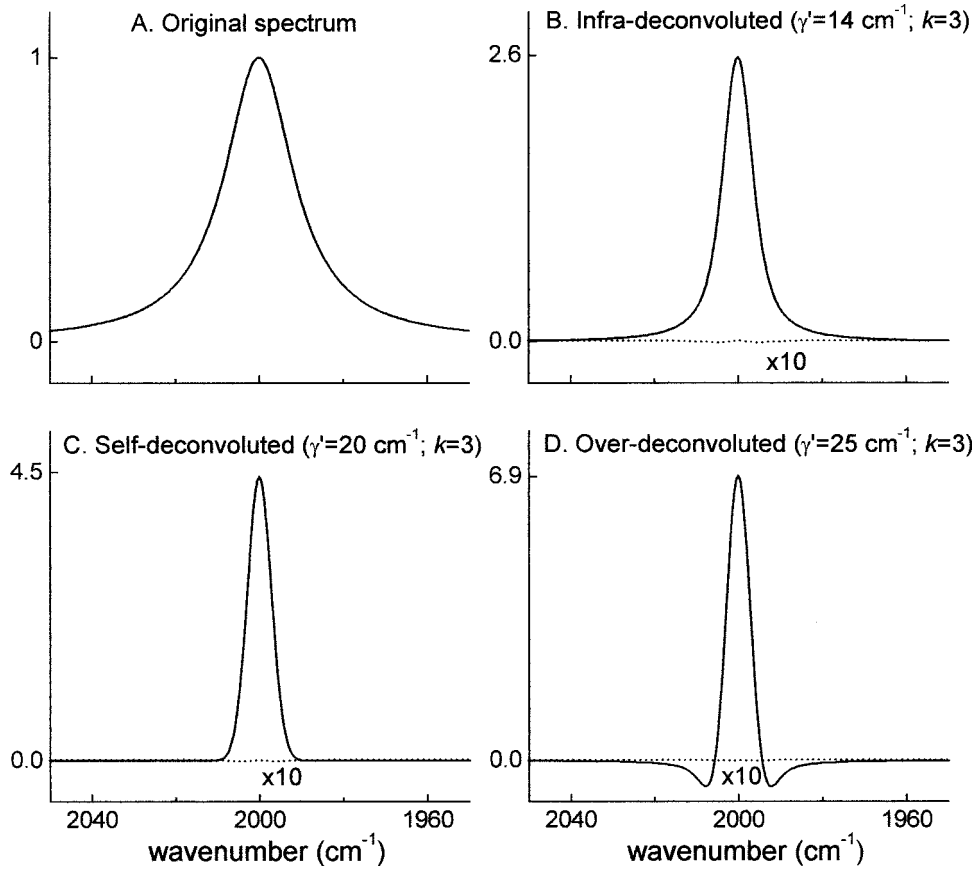

FIG. 1. A pure Lorentzian band centered at 2000 cm^{-1}, with area equal to one, and a FWHH of 20 cm^{-1} (**A**) was deconvoluted with the parameters displayed in each graph (**B–D**) using a Gaussian filter. The deconvoluted bands were fitted using a Voigt band. The derived parameters (equal for the three deconvolutions) were: position at 2000.00 cm^{-1}, area of 1.000, and width of 20.00 cm^{-1}. The fit residual (dotted line) multiplied by ten is displayed as well.

broadening cannot be completely eliminated from the spectrum, even if the $L(\nu)$ profile is perfectly known. We cannot speak about an actual FSD, but about FD. The spectrum for n Lorentzian bands will be:

$$E(\nu) = \sum_{i=1}^{n} \frac{A_i\gamma_i}{2\pi[(\gamma_i/2)^2 + (\nu - \nu_i)^2]} \otimes R(\nu) \qquad (6)$$

where A_i, γ_i, and ν_i are the area, width, and position of the i band. $E(x)$ is obtained as:

$$E(x) = \sum_{i=1}^{n} A_i \exp(-2\pi\nu_i|x|j)\exp(-\gamma_i\pi|x|)R(x) \qquad (7)$$

where j stands for $\sqrt{-1}$. The deconvolved spectrum $E'(\nu)$ becomes:

$$E'(\nu) = \Im\left\{\frac{E(x)D(x)}{W(x)}\right\} = \sum_{i=1}^{n} \frac{A_i(\gamma_i - \gamma')}{2\pi\{[(\gamma_i - \gamma')/2]^2 + (\nu - \nu_i)^2\}} \otimes D(\nu) \qquad (8)$$

where $W(\nu)$ is the Lorentzian band shape of width γ' used to deconvolve $E(\nu)$. So the spectrum after deconvolution can be expressed as the convolution of Lorentzian bands of width equal to γ_i' with $D(\nu)$, where γ_i' is given by $\gamma_i - \gamma'$. The narrowing factor (k) derived for the self-deconvoltion case (Eq. 5) will be redefined for the general case as the ratio of the width used to deconvolve $W(\nu)$ to the width of the filter $D(\nu)$:

$$k = \frac{FWHH[W(\nu)]}{FWHH[D(\nu)]} = al\gamma' \qquad (9)$$

where we see that the narrowing factor depends only on parameters defined by the user, and it is not related to the spectrum being deconvoluted.

The effective narrowing factor for a band i (k_i^{eff}), will be defined as the actual narrowing experienced by a band i:

$$k_i^{\text{eff}} = \frac{FWHH[E_i(\nu)]}{FWHH[E_i'(\nu)]} \qquad (10)$$

RESULTS AND DISCUSSION

Use of Voigt Bands to Fit Deconvoluted Lorentzian Bands. When in Eq. 8, $D(x)$ is a truncated Gaussian, the resulting bands can be closely described by Lorentzian bands of FWHH equal to γ_i', convolved with a Gaussian band of FWHH equal to γ'/k, i.e., Voigt bands with fixed Gaussian width. Voigt bands do not have an analytical expression (in the wavenumber domain), but they are important enough to be included in most of the fitting programs for spectroscopy. In this way considerable extra effort to the user is saved.

Figure 1 shows a Lorentzian band with a 20 cm^{-1}

width (γ_i = 20 cm^{-1}), with maximum at 2000 cm^{-1}, and area unity. This band was deconvolved using a deconvolution width (γ') of 14 cm^{-1} (infra-deconvolution), 20 cm^{-1} (self-deconvolution), and 25 cm^{-1} (over-deconvolution), and a narrowing factor (k) equal to 3. A Voigt band was used to fit the deconvoluted bands. Figure 1 also displays the residual of the fit multiplied by ten. During the fit, the area, position, and Lorentzian width of the deconvoluted band (γ_i') were adjusted, and the Gaussian width was fixed to γ'/k. From the fit to the three deconvolutions, the area, position, and width of the original Lorentzian (γ_i), given by $\gamma_i' + \gamma'$, were precisely obtained. This means that the use of the Voigt band shape is equally applicable to other situations apart from self-deconvolution, as are infra- and over-deconvolution.

One of the most used filters in deconvolution is the Bessel filter.[2] When this filter is used, the FD of a Lorentzian band is the convolution of a Lorentzian band with width given by $\gamma_i - \gamma'$, with the Fourier transform of the Bessel filter, of width equal to γ'/k. This type of function is not included in commercial fitting programs, but it has an analytical solution, so it might be introduced in fitting programs that allow for user-defined functions. The analytical expression is, however, very complex. For an individual band i it becomes:

$$\begin{aligned} E'(\nu) = {} & \frac{A_i \exp(-\pi l \gamma_i')}{\pi^5 l^4 (\gamma_i'^2 + 4\nu'^2)^5} \\ & \times \{\sin(2\pi l \nu') 16\nu' \\ & \quad \times [\pi^2 l^2 (\gamma_i'^2 + 4\nu'^2)^2 (3\gamma_i'^2 - 4\nu'^2) \\ & \qquad + 12\pi l \gamma_i' (\gamma_i'^2 - 4\nu'^2)(\gamma_i'^2 + 4\nu'^2) \\ & \qquad + 3(5\gamma_i'^4 - 40\nu'^2\gamma_i'^2 + 16\nu'^4)] \\ & \quad - \cos(2\pi l \nu') \\ & \quad \times 8[\pi^2 l^2 \gamma_i' (\gamma_i'^2 - 12\nu'^2)(\gamma_i'^2 + 4\nu'^2)^2 \\ & \qquad + 3\pi l (\gamma_i'^2 + 4\nu'^2) \\ & \qquad \times (\gamma_i'^4 - 24\nu'^2\gamma_i'^2 + 16\nu'^4) \\ & \qquad + 38(\gamma_i'^4 - 40\nu'^2\gamma_i'^2 + 80\nu'^4)]\} \end{aligned} \quad (11)$$

where $\gamma_i' = \gamma_i - \gamma'$, $\nu' = \nu - \nu_0$, A_i is the area, and $l = k/(1.05\gamma')$. We found it more convenient to use commercially available tools. For this reason, we used a Voigt band instead of Eq. 11 to fit a deconvoluted Lorentzian band filtered with a Bessel function. We observed that the Fourier transform of a Bessel filter with FWHH equal to γ, is relatively well described by a Gaussian band of FWHH equal to 0.937γ (not shown). In fact, this similarity holds for most of the FD filters, and so a Voigt band can generally be used as an approximation to any deconvoluted Lorentzian band.

Figure 2 is similar to Fig. 1, but a Bessel filter was used in the deconvolution process. A Voigt band was used to fit the deconvolved bands, with a Gaussian width kept fixed to $0.937\gamma'/k$. From the fit of the deconvoluted bands, the area, position, and width of the original Lorentzian were precisely obtained for the infra- and self-deconvoluted spectrum, although the Voigt approximation was less accurate for the over-deconvoluted case. The areas obtained were 0.99, 1.02, and 1.16 for the infra-, self-, and over-deconvoluted bands, respectively.

We tested other bands often used to fit deconvoluted Lorentzian bands with the aim of determining if any of them could surpass the results we obtained with the use of Voigt bands. For this, the deconvoluted bands in Fig. 2 (with area equal to one) were fitted with Lorentzian, Gaussian, and mixed Gaussian–Lorentzian bands. When a Lorentzian band was used, the areas obtained were 1.06, 1.35, and 1.88; only for the infra-deconvolution case could the Lorentzian band compete with the Voigt band. A Gaussian band gave area values of 0.78, 1.05, and 1.54, being accurate only for the self-deconvoluted band. The mixed Gaussian–Lorentzian band, with one fitting parameter more than the Voigt band, gave areas of 1.00, 0.91, and 0.60. In conclusion, the Voigt approximation is more accurate and has more general scope of validity than the previously used bands, which seem to be appropriate only in some concrete cases. Moreover, these bands only report the position and area but not the width of the original band, information that *is* available with the use of the Voigt bands.

The Narrowing Factor (k) and the Effective Narrowing Factor (k^{eff}). In Eq. 10, we introduced the expression for the effective narrowing. We will show how this parameter depends on the narrowing factor (k), on the ratio of the initial Lorentzian width to the width used to deconvolve (γ_i/γ'), and on the used filter ($D(x)$).

The FWHH of a band profile after deconvolution can be obtained by solving the following equation:

$$\frac{\int_0^l \exp(-\pi(\gamma_i - \gamma')x) D(x) \cos(2\pi\nu x)\, dx}{\int_0^l \exp(-\pi(\gamma_i - \gamma')x) D(x)\, dx} = 0.5 \quad (12)$$

where the numerator integral gives the band profile after deconvolution,[20] the denominator integral normalizes the maximum height to one, and the equality is solved for the two positions (ν_1 and ν_2) that correspond to half of the maximum height. The FWHH after deconvolution is thus the absolute value obtained when subtracting both solutions, and the effective narrowing is:

$$k^{\text{eff}} = \frac{FWHH[E_i(\nu)]}{FWHH[E_i'(\nu)]} = \frac{\gamma_i}{|\nu_1 - \nu_2|} \quad (13)$$

Figure 3A shows the k^{eff} dependence on the γ_i/γ' ratio for different narrowing factors (k), when $D(x)$ is a Bessel function. The effective narrowing obtained by deconvolution is only equal to the narrowing factor when $\gamma_i/\gamma' = 1$ (in self-deconvolution). The dependence of k^{eff} on the γ_i/γ' ratio at a fixed k is bell-shaped, and the maximum shifts from infra-deconvolution to over-deconvolution as k is increased. Figure 3B shows how the k^{eff} depends on k for different γ_i/γ' ratios. When $\gamma_i/\gamma' = 1$, k^{eff} increases at the same rate that k is increased. When $\gamma_i/\gamma' > 1$ (infra-deconvolution) the increase of k^{eff} is smaller than the increase of k, becoming null at a sufficiently high k. In contrast, when $\gamma_i/\gamma' < 1$ (over-deconvolution) the increase of the effective narrowing is greater than the increase of k. In addition, to obtain low narrowing, say $k^{\text{eff}} < 1.5$, it seems not very critical to use a deconvolu-

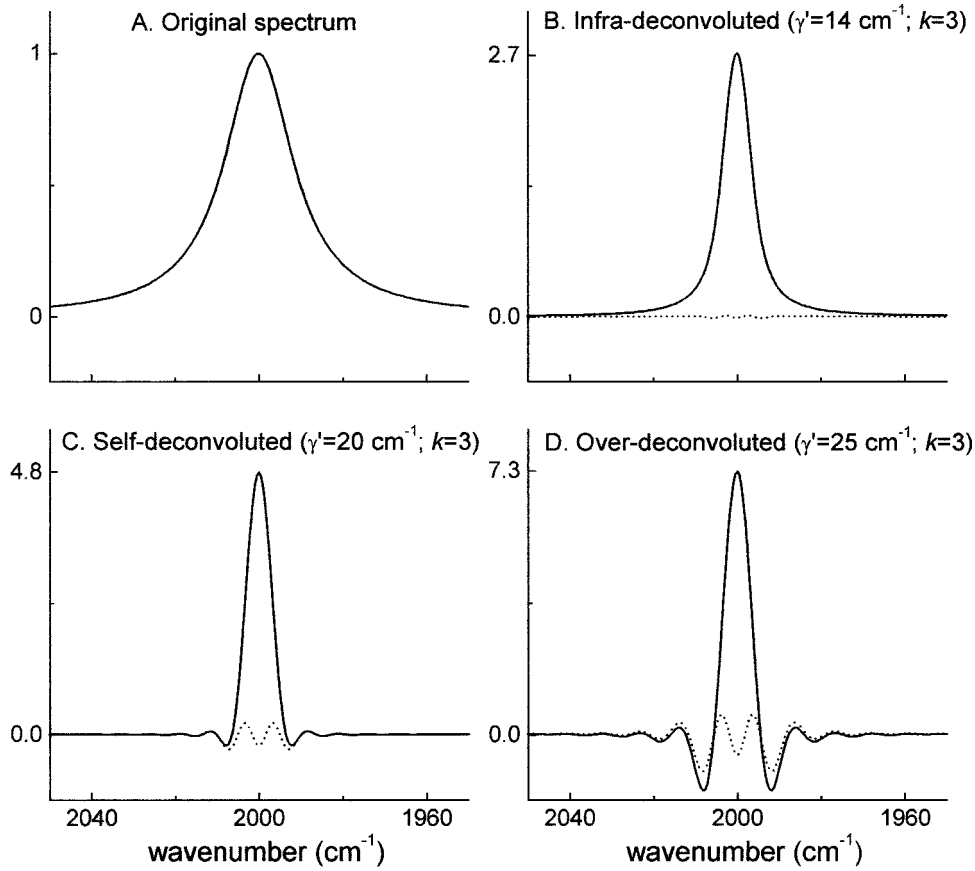

FIG. 2. A pure Lorentzian band centered at 2000 cm^{-1}, with area equal to one, and a FWHH of 20 cm^{-1} (**A**) was deconvoluted with the parameters displayed in each graph (**B–D**) using a Bessel filter (solid line). The deconvoluted bands were fitted using a Voigt band. The derived parameters were: (**B**) position (ν_0) at 2000.00 cm^{-1}, area (A) of 0.989, and width (γ_i) of 19.72 cm^{-1}; (**C**) ν_0 at 2000.00 cm^{-1}, A of 1.021, and γ_i of 19.89 cm^{-1}; (**D**) ν_0 at 2000.00 cm^{-1}, A of 1.160, and γ_i of 20.96 cm^{-1}. The fit residual (dotted line) at the same scale is displayed as well.

tion FWHH (γ') close to the actual FWHH (γ_i), but for high narrowing ($k^{\text{eff}} > 2.5$) it becomes very important to match the actual band width with less than a 20% relative error.

When the filter $D(x)$ is a truncated Gaussian, plots similar to those in Fig. 3 are obtained, although with slightly different values (not shown).

Noise in Fourier Deconvolution. An important limitation of deconvolution is its effect in the signal-to-noise ratio of the deconvoluted spectrum. The ratio of the signal-to-noise ratio of a band after deconvolution $(S/N)_f$ to the signal-to-noise ratio before deconvolution $(S/N)_i$ depends on several factors: the narrowing factor (k), the original bandwidth (γ_i), the ratio between the original bandwidth and that used to deconvolve (γ_i/γ'), the filter function $D(x)$, the instrumental line shape function $R(x)$, and the nominal resolution of the original spectrum ($1/x_f$). Kauppinen et al.[2] studied $(S/N)_f/(S/N)_i$ vs. k for different filter functions $D(x)$ in the case of self-deconvolution. The study aimed at finding the most convenient filter function that gave minimal reduction of the signal-to-noise ratio for a given k, with a final shape with tolerable side lobes. They found that the Bessel function was one of the most suitable filter functions for self-deconvolution and much more convenient than Gaussian for $k > 2$. They also derived a formula to compute approximately $(S/N)_f/(S/N)_i$ in the presence of white noise (Eq. 17, in Kauppien et al.[2]). We extended the formula to include other situations apart from the self-deconvolution case:

$$\frac{(S/N)_f}{(S/N)_i} = \left\{ \int_0^l D(x)R(x)\exp[-\pi(\gamma_i - \gamma')x]\,dx \div \sqrt{\int_0^l D(x)^2R(x)^2\exp(2\pi\gamma' x)\,dx} \right\} \div \left[\int_0^{x_f} R(x)\exp(-\pi\gamma_i x)\,dx \Big/ \sqrt{\int_0^{x_f} R(x)^2\,dx} \right] \tag{14}$$

We computed Eq. 14 for the case when $R(x)$ is a triangular function (one of the most common apodizations in FT-IR), taking a nominal resolution of 2 cm^{-1}, an original bandwidth of 20 cm^{-1}, and $D(x)$ being either a Bessel or a Gaussian function. Figure 4 shows the results of applying Eq. 14 for the Bessel apodization. It can be observed that the signal-to-noise ratio decays almost exponentially as k is increased, with a slope in logarithmic scale ranging between 0.85 and 0.65. This means that for having the same final signal-to-noise in a deconvoluted spectrum, the k used can be increased in one unit if the signal-to-noise ratio of the original spectrum is increased 5–7 times. Figure 4 also shows that the reduction in the

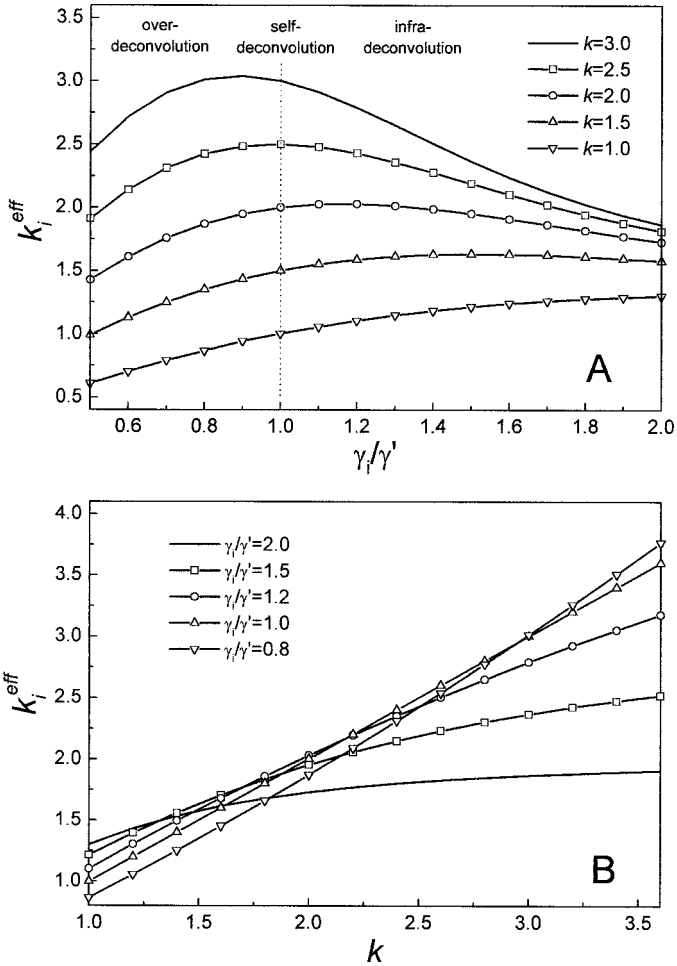

FIG. 3. Dependence of the effective narrowing (k^{eff}_i) obtained after deconvolution of a Lorentzian band, using a Bessel filter, on: (**A**) the ratio of the Lorentzian FWHH to the FWHH used to deconvolve (γ_i/γ') for five different narrowing factors (k); (**B**) the narrowing factor (k) for different ratios of the Lorentzian FWHH to the FWHH used to deconvolve (γ_i/γ').

signal-to-noise ratio due to deconvolution increases from over- to infra-deconvolution.

Effective Narrowing and Noise Increase. One of the aims of deconvolution is the maximum band narrowing with the minimum decrease of the signal-to-noise ratio. This procedure allows finding the number and approximate positions of components of an envelope band. Therefore, we are interested in how the signal-to-noise ratio varies, not with the narrowing factor (Fig. 4), but with the effective narrowing, since the higher the signal-to-noise ratio and the effective narrowing, the more easily component bands will be detected. This dependence is shown in Fig. 5 for both Bessel and truncated Gaussian filters, for an original Lorentzian band of FWHH (γ_i) equal to 20 cm^{-1}. The plots were obtained by combining Eqs. 12, 13, and 14. The differences between infra-, and self- or over-deconvolution are evident. For example, to obtain an effective narrowing higher than 2 by means of infra-deconvolution would be very expensive in terms of signal-to-noise degradation. In contrast, according to Fig. 5, over-deconvolution allows one to obtain higher narrowing with less cost in the signal-to-noise ratio; thus, it can be useful for the identification of the number of bands

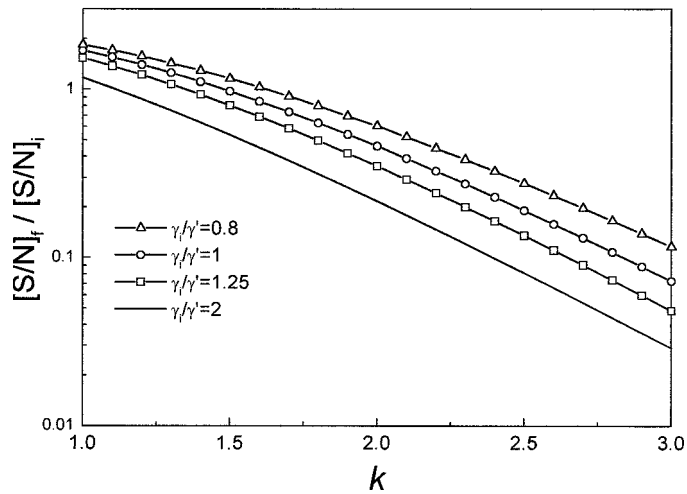

FIG. 4. Dependence of the ratio (signal-to-noise after deconvolution/signal-to-noise before deconvolution) on the narrowing factor (k), for a Lorentzian band of FWHH equal to 20 cm^{-1} deconvolved using a Bessel filter. The dependence was drawn for different ratios of the Lorentzian FWHH to the FWHH used to deconvolve (γ/γ').

and their positions. However, the distortions in the line shape introduced by over-deconvolution must be taken into account. For most of the filters, over-deconvolution is accompanied by marked negative and/or positive lobes and oscillations that can hide weak bands. These distortions in shape are markedly higher for the Bessel filter (high negatives lobes, faint positive lobes, and oscillations (see Fig. 2D)) than for the Gaussian filter (low negatives lobes, no positive lobes, and no oscillations (see Fig. 1D)).

Optimum Deconvolution Parameters to Resolve Noisy Overlapped Bands. According to the previous section the problem of finding the optimum deconvolution parameters is reconverted into the question of finding a compromise between the effective narrowing and the

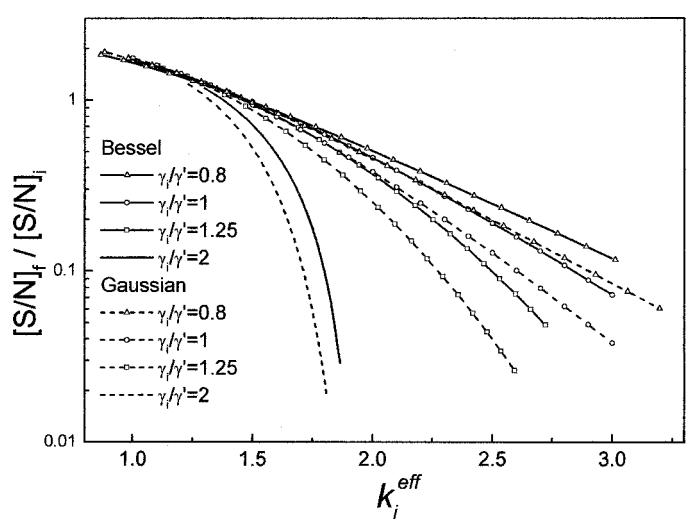

FIG. 5. Dependence of the ratio (signal-to-noise ratio after deconvolution/signal-to-noise ratio before deconvolution) on the effective narrowing factor (k^{eff}_i), for a Lorentzian band of FWHH equal to 20 cm^{-1}. The dependence was drawn for different ratios of the Lorentzian FWHH to the FWHH used to deconvolve (γ/γ'). Solid lines represent the use of a Bessel filter and dotted lines the use of a Gaussian filter.

final signal-to-noise ratio needed to clearly see the components. Let us consider a spectrum that is optimally deconvoluted. If we have a spectrum composed of the same bands, but slightly broader or closer bands, and deconvoluted in the same way, bands will appear less resolved after deconvolution. In this case, the final signal-to-noise ratio, previously sufficient to clearly differentiate bands from noise, can now become insufficient as bands become less marked. This simple situation illustrates the fact than the optimum final signal-to-noise ratio and effective narrowing depend on the parameters of the overlapped bands, but these parameters are not known. Given a certain known spectrum with a certain initial signal-to-noise ratio, it may be possible to find optimum deconvolution conditions, but a general procedure to determine the highest number of clearly resolved component bands for any spectrum is unlikely to ever be found, even though some authors have developed methods that are commonly used to determine optimum deconvolution parameters.[3,20,26]

One of the most used criteria was derived by Kauppinen et al.[3] The criterion is based on the fact that the interferogram of a spectrum, $E(x)$ in our notation, should be cut before its signal is equal to the noise; anything else would mean an unnecessary increase of noise. For a Lorentzian band of width γ, the maximum cut-point (l_{max}) is:[3]

$$l_{max} = (\pi\gamma)^{-1}\ln[\pi\gamma x_f (S/N)_i] \qquad (15)$$

where $(S/N)_i$ is the signal-to-noise ratio of the band before deconvolution, and x_f is the reciprocal of the nominal resolution. For the self-deconvolution case, the maximum narrowing factor recommended (k_{max}) is thus:[3]

$$k_{max} = a\gamma l_{max} = \frac{a}{\pi}\ln\left[\pi\gamma x_f\left(\frac{S}{N}\right)_i\right] \approx \log\left[\left(\frac{S}{N}\right)_i\right] \qquad (16)$$

where the factor a is filter dependent. Note that Eq. 16 assumes that we are operating in self-deconvolution conditions, and only an estimate of the highest narrowing factor recommended (k_{max}) is given. When a narrowing factor equal to k_{max} is used to deconvolve a Lorentzian band ten times broader than the nominal resolution (a reasonable case for IR bands obtained at 2 cm^{-1} resolution), apodized with a triangle function, the final signal-to-noise ratio obtained by this criterion is around 60. This method therefore provides only a way to keep the final signal-to-noise ratio over an arbitrary value of 60, which is not necessarily an optimal condition. Moreover, practical reasons tend to decrease this number further, namely, infra-deconvolution, the way the $(S/N)_i$ is determined (for overlapped bands the envelope signal-to-noise ratio is often used), and the presence of non-pure Lorentzian band shape.

Graphical criteria[20,26] are similar to that of Kauppinen et al. (tries to control the noise enhancement in deconvolution whereas the effective narrowing is ignored). The interferogram point where the noise surpasses the signal is found empirically in a power spectrum of the spectrum to be deconvoluted. The problem is that only the point where the global interferogram signal fades away into the noise is obtainable. Narrow bands dominate the signal at long distances but these narrow bands may not be the bands we are interested in deconvolving, carrying to an over-estimation of the cut-point (l) and so to an unnecessary decrease of signal-to-noise in the bands we are really interested in. When used, this overestimation of l leads to the use of very low deconvolution bandwidths ($\gamma' \approx 4$ cm^{-1}) to make k acceptably small ($k = 1.6$) in order to avoid an intolerable signal-to-noise degradation.[20] The undesirable consequence will be a very small effective narrowing.

Depending on the spectrum to be deconvolved, our general recommendation when Fourier deconvolution is used to identify the number of underlying bands is the following: if the bands are expected to have similar widths, then the Bessel filter with a γ' giving no over-deconvoluted bands is recommended. For a spectrum where bands show very dissimilar widths, then an averaged width should be used to deconvolve (to avoid a generalized infra-deconvolution), even if some bands are over-deconvoluted. A Gaussian filter is recommended in this case to reduce the possible artifacts introduced by the presence of negative and positive side lobes. To obtain the narrowing factor, an initial guess can be obtained from the Kauppinen et al. criterion. In any case, the magnitude of the oscillations in an interval free from bands should be compared with the observed features of the spectrum (shoulders and maxima) in order to correctly assign features either to resolved bands or to noise. Other than that, it is advisable to perform deconvolution in replicate spectra, and thus non-repetitive features can be assigned to noise.

Precision in the Curve Fitting of a Fourier Self-Deconvoluted Noisy Lorentzian Band. Although maximum narrowing with minimum decrease of signal-to-noise ratio is critical to band identification of overlapped bands, the needs of other types of analysis are different. For instance, to retrieve band parameters from deconvolution spectra, curve fitting is necessary. The precision in the parameters obtained by curve fitting depends on the noise but also on the number of independent points in the data. For an isolated band in the presence of white normal noise, the precision in the determination of a band parameter by curve fitting is given by:[25]

$$P(a_i) = \frac{\bar{a}_i}{\sigma(a_i)} = c(a_i) \times \left(\frac{S}{N}\right) \times \sqrt{N} \qquad (17)$$

in which it is stated that the precision P (relative error reciprocal) for a parameter a_i obtained by curve fitting is proportional to the signal-to-noise ratio (S/N) and to the square of the number of independent points per line width, with the proportional constant (c) dependent on the parameter being determined and on the band shape. This expression is valid as far as the noise is white and normal and the curve fitting is performed with the right band shape.[25]

Let us consider a noisy pure isolated Lorentzian band obtained from an ideal FT-IR experiment with bandwidth γ_i equal to 20 cm^{-1}, at 2 cm^{-1} nominal resolution, and 0.5 cm^{-1} digital resolution. Since in FT-IR spectroscopy two independent points are obtained per nominal resolution (if the digital resolution is at least half of the nominal resolution),[25,27] the precision in the area measurement (P(area)), when the bandwidth is known, will be $\sqrt{(\pi/4)}$

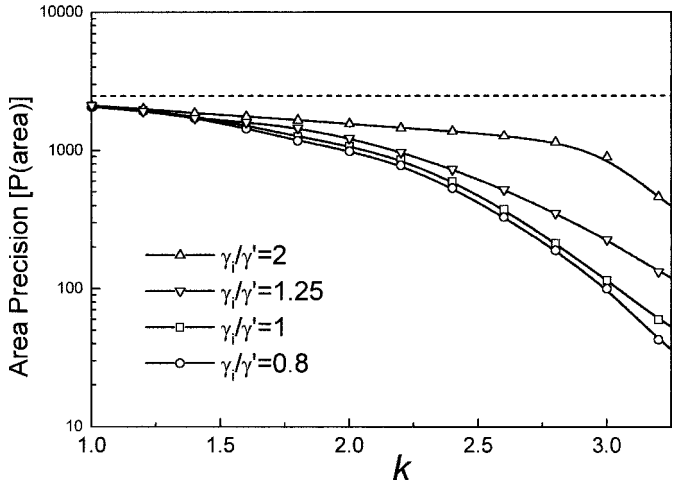

FIG. 6. Area precision obtained from the curve fitting of an FD isolated noisy Lorentzian band (γ = 20 cm^{-1}) as a function of the narrowing factor (k), for different γ/γ' ratios. The precision was obtained experimentally by simulations. The precision obtained when fitting the non-deconvoluted band (marked as a dotted line) was observed to be always superior to that obtained by FD.

$\times$ (S/N) $\times \sqrt{(20/1)}$.[27] When the signal-to-noise ratio is 1000, P(area) is thus 3964. There is another approach to obtain the precision, not based on theoretical considerations but on an empirical approach, as it is the calculus of the mean ($\bar{a}_i$) and standard deviation ($\sigma(a_i)$) of the fitted parameters for a large number of replicates. When twenty noisy Lorentzian bands (with signal-to-noise ratio equal to 1000) were curve fitted with the bandwidth fixed at 20 cm^{-1}, the P(area) obtained in this way was 4163, close enough to the theoretical result to consider that 20 simulations give reliable results.

The question now is how FD affects the precision in the area determination. We will consider the self-deconvolution case, when the width of the Lorentzian band is perfectly known. When a truncated Gaussian filter is used in the deconvolution, a Lorentzian band becomes a Gaussian band with a bandwidth equal to γ'/k cm^{-1}. As the nominal resolution after deconvolution is $l^{-1} \cong k/\gamma'$, N becomes 2. The final signal-to-noise ratio after deconvolution can be determined as previously described (see Eq. 14). Thus, for a Gaussian of known width, P(area) becomes 0.868 $\times$ $(S/N)_f$ $\times \sqrt{2}$.[25] This theoretical estimation is probably not accurate, as the expression in Eq. 17 assumed the noise to be white, and this is not the case in a deconvoluted spectrum. For this reason, P(area) was also empirically determined for several k values by fitting a Gaussian band of fixed width to twenty self-deconvoluted noisy Lorentzian bands. The results showed discrepancies between the theoretical P(area) and that empirically determined by simulations (not shown). These discrepancies are reduced at low k. This is reasonable, as at low k the exponential multiplication function in the interferogram grows less, the noise is thus whiter, and the theoretical expression becomes applicable. For that reason, further work was performed on simulations and not on analytical expressions.

Precision in the Curve Fitting of a Fourier Deconvoluted Noisy Lorentzian Band. Twenty deconvoluted noisy Lorentzian bands, with a $(S/N)_i$ equal to 1000 and a width (γ_i) of 20 cm^{-1}, were curve fitted with a Voigt band plus a baseline. The area precision (P(area)) obtained as a function of k for various γ/γ' ratios appears in Fig. 6, where two trends are evident: the area precision decreases with k, and it also decreases from infra- to over-deconvolution. This result is important as it shows that self-deconvolution does not need any special quality in order to retain the information content of the original spectra over the noise. Moreover, comparison of Figs. 4 and 6 shows that after deconvolution the signal-to-noise ratio and area precision display opposite dependence on the γ_i/γ' ratio; therefore, the final signal-to-noise ratio is not the only determining factor in the parameter precision, and the number of independent points per bandwidth (and probably the frequency dependence of the noise) plays an important role. This important role may not be evident when judging a fitting by eye. An example of this is presented in Fig. 7, in which a noisy Lorentzian

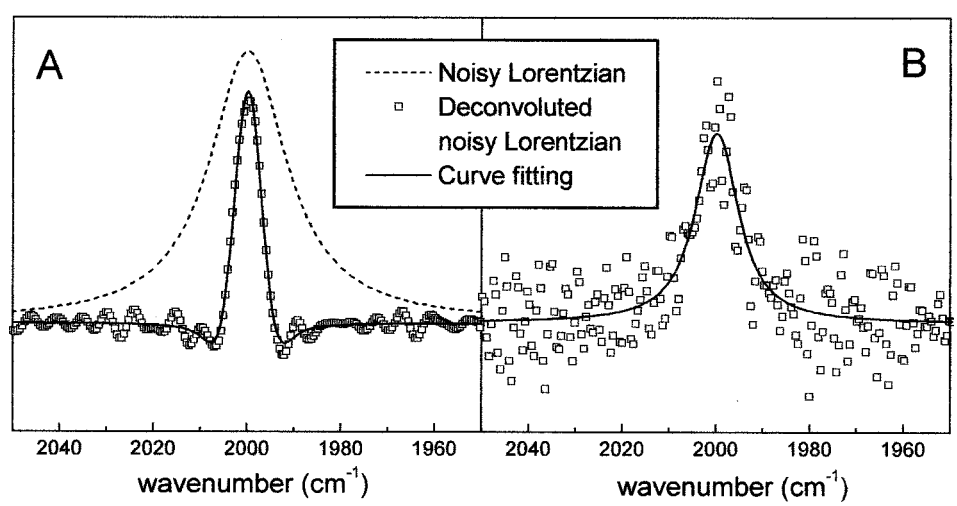

FIG. 7. A noisy Lorentzian band (dotted line) of area unity and FWHH of 20 cm^{-1} with an initial signal-to-noise ratio of 1000, 2 cm^{-1} nominal resolution, and 0.5 cm^{-1} digital resolution, was deconvoluted (open squares) with: (**A**) γ' = 25 cm^{-1} and k = 2.5; (**B**) γ' = 10 cm^{-1} and k = 2.5. After that, both bands were curve fitted (solid line). Although the signal-to-noise ratio was six times higher in (**A**), the area can be obtained with six times more precision from (**B**), as reported in Fig. 6. For the present example, the curve fitting in (**A**) reported an area of 1.017 and a FWHH of 20.19 cm^{-1}, whereas that in (**B**) reported an area of 1.003 and a FWHH of 20.06 cm^{-1}. All plots are in a relative scale.

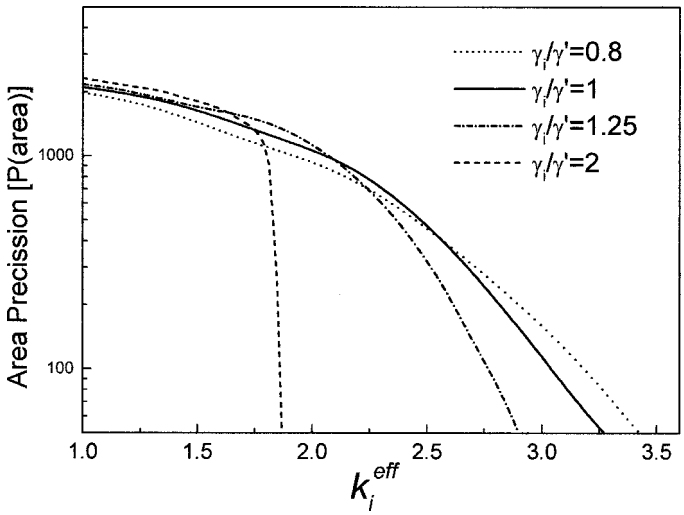

FIG. 8. Same as Fig. 6, but the data was plotted as a function of the effective narrowing (k^{eff}), instead of the narrowing factor (k).

band was infra- and over-deconvoluted. Although the over-deconvoluted band shows a much clearer appearance, with a signal-to-noise ratio six times higher than for the infra-deconvoluted band, better results were obtained curve fitting the infra-deconvoluted band (see legend of Fig. 7).

The dashed line in Fig. 6 marks the P(area) for the original noisy Lorentzian band. It can be concluded that, as expected for an isolated band in the presence of white noise, the highest precision is obtained from the curve fitting of the crude rather than from the deconvoluted data.

Curve Fitting of Complex Spectra. When dealing with complex spectra, other factors apart from the obtainable precision grow in importance, making the curve fitting of deconvoluted spectra usually much more attractive. Namely, if bands are significantly resolved after deconvolution, the curve fitting convergence will be faster, the obtained solution will reduce its sensitivity to the curve fitting initial parameter guesses, and systematic errors in the data (such as baseline distortions) or in the assumptions (such as the use of an incorrect band shape) will less affect the quality of the obtained results.[18] The same benefits have been observed when second derivative spectra are fitted.[28] Currently, the most important shortcoming of curve fitting of deconvoluted spectra is the systematic error introduced by the use of inappropriate bands (Lorentzian and Gaussian); but as we have presented, this error can be eliminated or at least reduced by introducing Voigt bands in curve fitting.

As we showed in Fig. 6, the precision obtained by curve fitting a deconvoluted band was dependent on the deconvolution parameters used. From the set of deconvolution parameters giving a well-conditioned curve-fitting, we would like to use the parameters giving the highest area precision, i.e., the lower error in the band area estimation. For overlapping bands, Eq. 17 gives an overestimation of parameter precision. Parameter precision for an overlapped band will depend on parameters in Eq.

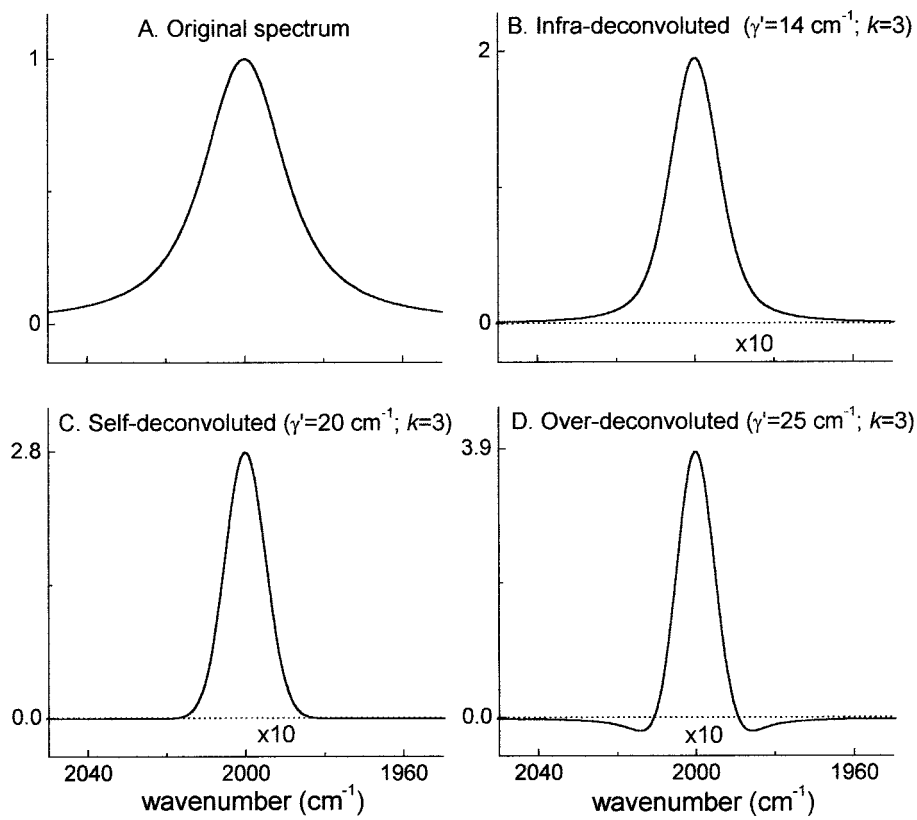

FIG. 9. A Voigt band centered at 2000 cm^{-1}, with area equal to one, Lorentzian FWHH of 20 cm^{-1}, and Gaussian FWHH of 10 cm^{-1} (**A**), was deconvoluted (**B–D**) with the parameters displayed in each graph using a Gaussian filter. The deconvoluted bands were fitted using a Voigt band. The derived parameters were: position at 2000.00 cm^{-1}, area of 1.000, Lorentzian width of 20.00 cm^{-1}, and Gaussian width of 10.00 cm^{-1}. The fit residual (dotted line) multiplied by ten is displayed as well.

17 but also on the rest of the overlapped bands. For that reason, only a general consideration of the problem will be given. Figure 8 shows the area precision for a deconvoluted noisy isolated Lorentzian band for different γ_i/γ' ratios as a function of the effective narrowing (the same data as Fig. 6 but with respect to the effective narrowing). As data in Fig. 8 was derived for an isolated band, the precision it gives will be an overestimation for an overlapped band. As the effective narrowing obtained in deconvolution is increased, overlapped bands will become more resolved, and they will approach the calculated precision for an isolated band. It should be noted that in Fig. 8 the area precision decreases drastically with the increase of the effective narrowing. Thus, it should be advisable to apply the minimum effective narrowing needed to partially resolve the component bands in the spectrum in order to obtain both high area precision and a good conditioning for the curve fitting. Figure 8 also shows how the useful region for curve fitting decreases at higher γ_i/γ' ratios. For instance, when γ_i/γ' was 2 the precision dropped dramatically for k^{eff} higher than 1.7. The use of ratios close to 1 appears more robust since the obtained precision decreases slowly up to a k^{eff} of 2.5 while keeping high precision over the entire range. From our experience in IR spectroscopy of proteins, we considered that amide I bands must be effectively narrowed at least around a factor of 2 to become partially resolved, and so the FWHH used to deconvolve (γ') should be in general chosen to be close to γ_i. Usually, complex spectra will display bands with different widths, and so the spectroscopist should decide whether γ_i should be considered the averaged width expected for the component bands or the width expected for the most intense bands.

On the other hand, when a Bessel filter is used and curve fitting is performed with Voigt bands, the FWHH used to deconvolve should be chosen as the width of the narrowest band (γ' equal to the smaller γ_i), as Voigt bands do not correctly fit over-deconvoluted bands for this filter.

Treatment of Non-Pure Lorentzian Bands. We have assumed all along that the line shape broadening function $L(\nu)$ could be approximated to a Lorentzian profile. When a band is subject to both homogeneous and inhomogeneous broadening, $L(\nu)$ can be generally approximated to a convolution of a Lorentzian profile with a Gaussian, i.e., a Voigt profile:[22,29]

$$L(\nu) = \frac{\gamma_L}{2\pi[(\gamma_L/2)^2 + \nu^2]} \otimes \frac{2\sqrt{\ln 2}}{\gamma_G\sqrt{\pi}} \exp\left[-\left(\frac{2\nu\sqrt{\ln 2}}{\gamma_G}\right)^2\right] \tag{18}$$

where γ_L is the FWHH of the Lorentzian component, and γ_G is the FWHH of the Gaussian component. To reduce the FWHH of the broadening function $L(\nu)$, it is more convenient to remove the Lorentzian character than to remove the Gaussian character. If the band is deconvoluted with a Lorentzian of FWHH equal to γ' and a filter $D(x)$ is used, the deconvoluted band becomes:

$$E'(\nu) = \frac{A(\gamma_L - \gamma')}{2\pi\{[(\gamma_L - \gamma')/2]^2 + (\nu - \nu_0)^2\}} \otimes \frac{2\sqrt{\ln 2}}{\gamma_G\sqrt{\pi}} \exp\left[-\left(\frac{2\nu\sqrt{\ln 2}}{\gamma_G}\right)^2\right] \otimes D(\nu) \tag{19}$$

where A is the band area and ν_0 is the band maximum. If the filter used is a truncated Gaussian, then the deconvoluted band can be closely expressed as a Voigt band:

$$E'(\nu) = \frac{A\gamma_L'}{2\pi\{[(\gamma_L - \gamma')/2]^2 + (\nu - \nu_0)^2\}} \otimes \frac{2\sqrt{\ln 2}}{\gamma_G'\sqrt{\pi}} \exp\left[-\left(\frac{2\nu\sqrt{\ln 2}}{\gamma_G'}\right)^2\right] \tag{20}$$

where $\gamma_G' = \sqrt{(\gamma_G^2 + (\gamma'/k)^2)}$. Now we will consider self-deconvolution as the condition that removes all the Lorentzian character of the original band ($\gamma' = \gamma_L$), and infra- and over-deconvolution when $\gamma' < \gamma_L$ and $\gamma' > \gamma_L$, respectively.

Figure 9 shows a Voigt band with $\gamma_L = 20$ cm^{-1} and $\gamma_G = 10$ cm^{-1}, area unity, and maximum at 2000 cm^{-1}, deconvolved for a Lorentzian band of diverse widths. A Gaussian filter was used and k was equal to 3. The resulting deconvoluted bands were curve fitted using a Voigt band with free Lorentzian and Gaussian width (γ_L' and γ_G'). All band parameters were obtained with high accuracy.

When the filter $D(x)$ is a Bessel apodization function, Eq. 19 has no analytical solution. Taking into account that the Fourier transform of a Bessel function resembles a Gaussian band, Eq. 19 can be approximated to a Voigt band, as that of Eq. 20, with $\gamma_L' = \gamma_L - \gamma'$, and $\gamma_G' = \sqrt{(\gamma_G^2 + (0.937\gamma'/k)^2)}$. When the Voigt band in Fig. 9 was deconvoluted using a Bessel filter, the band parameters derived by curve fitting showed good similarity to the original ones.

CONCLUSION

The theory of Fourier deconvolution has been presented for the case outside the self-deconvolution condition. When the original bands are pure Lorentzian in character, expressions were derived to compute the effective narrowing and the final signal-to-noise ratio after applying deconvolution. Two application areas are considered: identification of the underlying bands and curve fitting.

For the identification of the components under an envelope band, our results are in disagreement with general recommendations that favor the use of infra-deconvolution because it gives little narrowing while the signal-to-noise ratio is highly degraded. On the other hand, the usually avoided over-deconvolution showed good properties with respect to band narrowing and final signal-to-noise ratio. Moreover, for the Gaussian filter, over-deconvolution shows a fairly good shape, with only slight negative lobes, without positive lobes, and no side oscillations.

Concerning the use of a Fourier deconvoluted spectrum as a starting point for curve fitting, we have shown both theoretically and practically that Voigt bands can be used to fit deconvoluted Lorentzian and Lorentzian–Gaussian bands with high accuracy, being independent of infra-, self-, or over-deconvolution conditions. For a noisy isolated band, the effect of FD on the band precision obtained for the curve fitting was also studied. We concluded that deconvolution reduces the precision ob-

tainable by curve fitting, which is maximum when working with non-deconvoluted bands. Overlapped bands containing noise have been only briefly considered, and a tentative criterion has been proposed to obtain the highest precision in the area determination while maintaining good conditioning for the curve fitting. This criterion, when focused in the amide I region, is reduced to deconvolve with the expected average width of the component bands (or with the expected width of the most intense band) and a narrowing factor of at least 2. This recommendation should be independent of the initial signal-to-noise ratio of the spectrum, although it will severely affect the precision obtained.

As a final point, when a Bessel filter was used, the Voigt approximation also showed good results, although the errors increased in over-deconvolution. We considered that these conclusions are general for most common FD filters, and so Voigt bands can be generally used in the curve fitting of deconvoluted bands with little error, as far as bands are infra- or self-deconvoluted. In order to archive higher accuracy, or to deal with over-deconvoluted bands, the Voigt approximation should be replaced by the analytical expression of the deconvoluted band, an alternative, however, not always suitable due to its complexity.

Although it is likely that present or future nonlinear band-narrowing algorithms could surpass FD in its narrowing effect, we believe that FD should be the tool of choice when original spectra must be curve fitted because its linear property allows one to know the type of bands needed to fit the deconvoluted spectra if the type of bands in the original spectra are known.

ACKNOWLEDGMENTS

This work was supported by grants Bio4-CT97-2119 from the European Commission, 1999SGR00102 from the D.G.R. (Generalitat de Catalunya), BMC2000-0121 from the D.G.I. (Ministerio de Ciencia y Tecnología), and fellowship 1998-FI-00215 from the D.G.R. (Generalitat de Catalunya) to V.A.L.F.

1. J. K. Kauppinen, D. J. Moffatt, H. H. Mantsch, and D. G. Cameron, Appl. Spectrosc. **35,** 271 (1981).
2. J. K. Kauppinen, D. J. Moffatt, D. G. Cameron, and H. H. Mantsch, Appl. Opt. **20,** 1866 (1981).
3. J. K. Kauppinen, D. J. Moffatt, H. H. Mantsch, and D. G. Cameron, Anal. Chem. **53,** 1454 (1981).
4. D. M. Byler and H. Susi, Biopolymers **25,** 469 (1986).
5. R. Narayan and R. Nityananda, Annu. Rev. Astrophys. **24,** 127 (1986).
6. D. G. Cameron and D. J. Moffatt, Appl. Spectrosc. **41,** 539 (1987).
7. J. Biemond, R. L. Lagendijk, and R. M. Mersereau, Proc. IEEE **78,** 856 (1990).
8. J. K. Kauppinen, D. J. Moffatt, M. R. Hollberg, and H. H. Mantsch, Appl. Spectrosc. **45,** 411 (1991).
9. D. K. Buslov and N. A. Nikonenko, Appl. Spectrosc. **51,** 666 (1997).
10. P. E. Saarinen, Appl. Spectrosc. **51,** 188 (1997).
11. A. Barth, Spectrochim. Acta, Part A **56,** 1223 (2000).
12. S. Krimm and J. Bandekar, Adv. Protein Chem. **3,** 181 (1986).
13. S. Y. Venyaminov and N. N. Kalnin, Biopolymers **30,** 1259 (1990).
14. F. Dousseau and M. Pézolet, Biochemistry **29,** 8771 (1990).
15. J. L. Arrondo, A. Muga, J. Castresana, and F. M. Goñi, Prog. Biophys. Mol. Biol. **59,** 23 (1993).
16. L. K. Tam and S. A. Tatulian, Q. Rev. Biophys. **30,** 365 (1997).
17. E. Goormaghtigh, V. Cabiaux, and J. M. Ruysschaert, Eur. J. Biochem. **193,** 409 (1990).
18. J. A. Pierce, R. S. Jackson, K. W. van Every, and P. R. Griffiths, Anal. Chem. **62,** 477 (1990).
19. P. R. Griffiths, J. A. Pierce, and G. Hongin, ''Curve Fitting and Fourier Self-Deconvolution for the Quantitative Representation of Complex Spectra'', in *Computer-Enhanced Analytical Spectroscpy* (Plenum Press, New York, 1987), p. 29.
20. K. Rahmelow and W. Hübner, Appl. Spectrosc. **50,** 795 (1996).
21. W. H. Press, S. A. Teukolsky, W. T. Vetterling, and B. P. Flannery, *Numerical Recipes in C: The Art of Scientific Computing* (Cambridge University Press, Cambridge-New York-Melbourne, 1992), 2nd ed., Chap. 15.
22. D. W. Oxtoby, Annu. Rev. Phys. Chem. **32,** 77 (1981).
23. P. R. Griffiths and J. A. de Haseth, *Fourier Transform Infrared Spectrometry* (John Wiley and Sons, New York, 1986), Chap. 1.
24. D. G. Cameron and D. J. Moffatt, J. Test. Eval. **12,** 78 (1984).
25. A. G. Marshall and F. R. Verdun, *Fourier Transforms in NMR, Optical, and Mass Spectrometry* (Elsevier, Amsterdam-Oxford-New York-Tokyo, 1990), Chaps. 2 and 3.
26. L. Smeller, K. Goossens, and K. Heremans, Appl. Spectrosc. **49,** 1538 (1995).
27. Z. Liang and A. G. Marshall, Appl. Spectrosc. **44,** 766 (1990).
28. F. Holler, D. H. Burns, and J. B. Callis, Appl. Spectrosc. **43,** 877 (1989).
29. A. B. Myers, Annu. Rev. Phys. Chem. **49,** 267 (1998).

THE JOURNAL OF BIOLOGICAL CHEMISTRY
Vol. 277, No. 5, Issue of February 1, pp. 3380–3387, 2002

Printed in U.S.A.

Study of Amide-proton Exchange of *Escherichia coli* Melibiose Permease by Attenuated Total Reflection-Fourier Transform Infrared Spectroscopy

EVIDENCE OF STRUCTURE MODULATION BY SUBSTRATE BINDING*

Received for publication, June 13, 2001, and in revised form, November 15, 2001
Published, JBC Papers in Press, November 29, 2001, DOI 10.1074/jbc.M105466200

Natàlia Dave‡§, Víctor A. Lórenz-Fonfría‡¶, Joaquim Villaverde‡§, Raymonde Lemonnier‖, Gérard Leblanc‖, and Esteve Padrós‡**

From the ‡Unitat de Biofísica, Departament de Bioquímica i de Biologia Molecular, Facultat de Medicina, Universitat Autònoma de Barcelona, Bellaterra 08193, Barcelona, Spain and the ‖Laboratoire de Physiologie des Membranes Cellulaires-Laboratoire de Recherche Correspondant du Commissariat à l'Energie Atomique 16V, Université de Nice Sophia-Antipolis and CNRS (URA 6078), 06238 Villefranche sur Mer cedex, France

The accessibility of *Escherichia coli* melibiose permease to aqueous solvent was studied following hydrogen-deuterium exchange kinetics monitored by attenuated total reflection-Fourier transform infrared spectroscopy under four distinct conditions where MelB forms different complexes with its substrates (H^+, Na^+, melibiose). Analysis of the amide II band upon ^2H_2O exposure discloses a significant sugar protection of the protein against aqueous solvent, resulting in an 8% less exchange of the corresponding H^+·melibiose·MelB complex compared with the protein in the absence of sugar. Investigation of the amide I exchange reveals clear substrate effects on β-sheet accessibility, with the complex H^+·melibiose·MelB being the most protected state against exchange, followed by Na^+·melibiose·MelB. Although of smaller magnitude, similar changes in α-helices plus nonordered structures are detected. Finally, no differences are observed when analyzing reverse turn structures. The results suggest that sugar binding induces a remarkable compactness of the carrier's structure, affecting mainly β-sheet domains of the transporter, which, according to secondary structure predictions, may include cytoplasmic loops 4–5 and 10–11. A possible catalytic role of these two loops in the functioning of MelB is hypothesized.

It has become increasingly necessary to obtain both static and dynamic structural information to understand how hundreds of membrane co-transporters (or symporters) use the transmembrane electrochemical potential gradient of ions to drive solute transport in living cells. The melibiose permease (MelB)[1] of *Escherichia coli* encoded by the *melB* gene (1) is one of these hydrophobic membrane transporters (473 amino acids) and is the best-studied transporter of a large family of Na^+ solute symporters (2–4). MelB couples uphill transport of α- or β-galactosides to the downhill inward movement of Na^+, Li^+, or H^+. The coupling ions compete for the same binding site and enhance the affinity of the co-transported sugar, with Na^+ and Li^+ as better activators than H^+ (5, 6). The currently accepted topological model, consisting of 12 transmembrane domains and N and C termini located in the cytoplasm, is strongly supported by immunological studies (7, 8), extensive *melB-phoA* fusion analyses (8, 9), and proteolytic mapping (10). Photolabeling (11) and mutagenesis studies combined with fluorescence analysis (12) highlight the importance of the helix IV-loop 4–5 domain for MelB transport function. FTIR studies (13) showed a high α-helical content, giving support to the existence of 12 α-helix transmembrane domains.

Despite the high hydrophobic character of MelB (70% apolar residues) and the large proportion of transmembrane domains, helices are amphiphilic and form polar domains buried in the core of the protein that may accommodate the hydrophilic co-substrate. Thus, several acidic or polar residues either on helix I, II, or IV are likely to play a role in ion recognition (14–16). Evidence that C-terminal helices border the sugar binding site has been obtained (17–21). Moreover, evidence has been obtained that these polar domains are dynamic structures. An illustration is the ion (or sugar)-induced cooperative modification of MelB structure measured by spectroscopic and biochemical means and in particular ion-induced modification of the sugar binding domain (10, 13, 17–21).

The analysis of hydrogen-deuterium exchange kinetics provides a means to gain further insight into the structure and dynamics of the protein, and to identify sub-molecular motional domains (22–24). The H/D exchange kinetics can be obtained by ATR-FTIR spectroscopy, applied to film samples. Changes in intensity in the amide II (1600–1500 cm^{-1}) regions of a protein upon exposure to ^2H_2O can be followed in real time by using the ATR-FTIR technique, and their kinetics provides information about changes in protein tertiary structure and stability (25, 26). The rate of exchange is sensitive to the accessibility and stability of the protein, giving an estimation of how accessible is the protein structure to the aqueous solvent (27). Moreover, during the deuteration course amide I shifts

* This work was supported in part by grants Bio4-CT97-2119 from the European Commission (to G. L. and E. P.), Picasso 98127 (to G. L.), BMC2000-0121 from the Dirección General de Investigación, HF1997-0239 from the Ministerio de Educación y Cultura, BIO97-1918-CE from Comisión Interministerial de Ciencia y Tecnologia and 1999SGR-0102 from the Direcció General de Recerca (to E. P.). The costs of publication of this article were defrayed in part by the payment of page charges. This article must therefore be hereby marked "*advertisement*" in accordance with 18 U.S.C. Section 1734 solely to indicate this fact.

§ Fellows of the European Commission (Bio4-CT97-2119).
¶ A fellow of the Generalitat de Catalunya (1998-FI-00215).
** To whom correspondence should be addressed: Unitat de Biofísica, Facultat de Medicina, Universitat Autònoma de Barcelona, Bellaterra 08193, Barcelona, Spain. Tel.: 34-9358-11870; Fax: 34-9358-11907; E-mail: esteve.padros@uab.es.

[1] The abbreviations used are: MelB, melibiose permease; Mel, melibiose (6-*O*-α-galactopyranosyl-D-glucose); DM, dodecyl maltoside; α-NPG, *p*-nitrophenyl α-D-6-galactopyranoside; ATR-FTIR, attenuated total reflection-Fourier transform infrared; *k*, narrowing factor; MES, 4-morpholineethanesulfonic acid; H/D, hydrogen/deuterium.

about 5–10 cm^{-1} (28–31). Because this band provides information on the secondary structure of the protein (32, 33), a careful analysis of amide I should show how the different structures undergo exchange.

The observations that the purified MelB transporter retains full activity once reconstituted in liposomes (34) and that its conformation can be controlled by manipulating the medium co-substrate (18, 35) open the possibility to investigate the kinetics of H/D exchange of different conformations of MelB. The purpose of the present study is to examine the co-substrate dependence of accessibility of MelB and of its structural components by following the variations of the amide I and II components of the ATR-FTIR spectrum of MelB upon exposure to ^2H_2O.

EXPERIMENTAL PROCEDURES

Materials—*p*-Nitrophenyl α-D-[6-^{3}H]galactopyranoside ([α-^{3}H]NPG) was synthesized in our department (Laboratoire de Physiologie des Membranes Cellulaires) under the direction of Dr. B. Rousseau. Synthesis of (3-lauryl-amido)-*N*,*N*′-(dimethylamino)propylamine oxide was performed as previously described (36). Dodecyl maltoside (DM) was obtained from Roche Molecular Biochemicals, and nickel-nitrilotriacetic acid resin was from Qiagen. SM-2 Bio-Beads were obtained from Bio-Rad. Total *E. coli* lipids (acetone/ether-precipitated) were purchased from Avanti Polar Lipids. High purity grade salts or chemicals (Suprapur, Merck) were used to prepare nominally Na^+-free media containing less than 20 μM sodium salts. All other chemicals were obtained from commercial sources.

MelB Overproduction and Purification—An RecA derivative of *E. coli* DW2 (D*mel* D*lac*ZY) as described previously (37) was transformed with pK95DAHB plasmid to overexpress a wild type His-tagged MelB (19). Transformed cells were grown at 30 °C in 200 liters of M9 medium supplemented with appropriate carbon sources and ampicillin (100 mg/ml) at the Center de Fermentation, CNRS (Marseille, France), and used to prepare inverted membrane vesicles, by means of a French press (American Instrument Co). Purification of the His-tagged MelB was essentially carried out as previously described (34).

Preparation of MelB Proteoliposomes—MelB protein (0.5 mg/ml) solubilized in DM (0.1% w/v) was mixed with *E. coli* lipids to give a protein-to-lipid ratio of 1:2 (w/w). DM was removed by overnight adsorption in SM-2 Bio-Beads at 4 °C (38). The proteoliposomes were then subjected to repeated freeze/thaw-sonication-wash cycles in nominally Na^+-free, 20 mM MES, 10 mM KCl buffer (pH 6.6) to eliminate the NaCl from the sample and medium.

MelB Activity and Protein Assays—MelB activity in proteoliposomes or in the solubilized form was assessed by measuring [α-^{3}H]NPG binding activity as previously described (5). The protein concentration was assayed using serum bovine albumin as standard (39).

Infrared Measurements—A sample of 20 μl of protein solution at different substrate conditions (155 μg) was spread homogeneously on one side of a germanium crystal (50 × 10 × 2 mm, Harrick, Ossining, NY, yielding 12 internal reflections at the sample side) under a stream of nitrogen. The film was left at room temperature for more than 1 h, and the ATR device was covered with a stainless steel plate containing a gas input and output. For exchange, the film was exposed to a continuous flow of N_2 gas (220 ml/min), saturated with ^2H_2O by flushing it through nine closed 10-ml vials containing 2–3 ml of ^2H_2O each. The spectra were recorded every 5 min during the first 300 min, then every 10 min up to 600 min, and finally every 20 min up to 770 min. All the spectra were recorded at 20 °C with a thermostatic circulatory bath connected to the stainless plate, using an FT6000 Bio-Rad spectrometer, equipped with a cooled liquid nitrogen mercury-cadmium-telluride detector at a nominal resolution of 2 cm^{-1}.

The four film conditions analyzed were (*a*) MelB without added substrates (in the presence of H^+ as the only substrate); MelB incubated during 12 h with (*b*) NaCl 10 mM, (*c*) melibiose 5 mM, and (*d*) melibiose 5 mM and NaCl 10 mM. All samples were shortly sonicated before use. In the final rehydrated state, concentrations of the media salt and sugar constituents were increased about 20 times as compared with the initial suspension. As a result, all sugar binding sites were saturated.

Analysis of Infrared Spectra—Several corrections were applied to the experimental data prior to the analysis of H/D exchange kinetics of protein amide groups. All the spectra were first corrected for water atmospheric contribution (26). A correction of the amide II signal for film inflation was applied using the ratio amide II/amide I as a normalization factor (31). The ranges of integration for amides I and II were 1696–1600 cm^{-1} and 1565–1525 cm^{-1}, respectively. This correction was made under the assumption that the amide I band shifts only a few cm^{-1} upon H/D exchange, and therefore the area integrated in the amide I region reflects the amount of protein remaining in the effective IR path. Moreover, amide I and II are adjacent bands in the spectrum, so other sources of error, as effective path dependence on wavenumber or baseline problems, were minimized.

Another correction we considered was a possible lipid contribution in the amide I and II regions. To this end, H/D exchange kinetic experiments were performed on films of *E. coli* lipids devoid of proteins and used to estimate the lipid contribution to the amide I and II regions during the kinetic analyses. The subtraction factor was obtained by scaling the CH_2-stretching band of the lipid (3029–2780 cm^{-1}). The correction for the side chain absorption was made trough the creation of two synthetic spectra of the MelB primary sequence, one with data for the hydrogenated amino acids from Venyaminov and Kalnin (40) (correction of the spectra obtained before exchange starts) and the other with data for the deuterated amino acids from Chirgadze *et al.* (41) (correction of the spectra once exchange has started). The subtracting factor to scale the spectra was that needed to eliminate the tyrosine band (highly resolved in the deuterated form) (42).

After performing all indicated corrections, we obtained curves for MelB exchange upon different substrate conditions. These curves are known to be the Laplace transform of the amide-hydrogen time-exchange distribution function (31), which can be obtained by applying the inverse Laplace transform to the experimental data. The inverse Laplace transforms were obtained by the maximum entropy regularization method (43, 44), weighted to a prior flat estimate. This ensures that, when no information is present in the data, a flat distribution is assigned and over-interpretation is prevented. The regularized solution was obtained by a positive-constrained minimization using a variable metric method (44). The chose of the regularization parameter affects the resolution of the calculated distribution; because its value is decreased, more details become evident but also the result becomes more dependent on noise. The optimum value applied to all samples was considered to be the lower value common to all samples that gave results not significantly affected by the noise, as reported by Monte-Carlo simulations. The reported parameters and errors refer to the mean and standard errors obtained from independent samples in the same conditions (n = 2–3).

To analyze the behavior of each secondary structure through amide I (32, 33), different intensities were monitored from the deconvoluted exchange kinetics spectra: 1678 cm^{-1} for reverse turns, 1660 cm^{-1} for α-helices and non-ordered structures, and finally 1626 cm^{-1} for β-strands. The deconvolution parameters used for all spectra were a full width at half-height of 14 cm^{-1} and a k factor of 2 (below log(S/N)) (45). The monitored wavenumbers were selected according to the following procedure: First, a set of intensities at different wavenumbers of the amide I were monitored for all the kinetic spectra subtracted from the first unexchanged film spectrum. Baseline intensity monitored at 1860 cm^{-1}, where no sample absorption exists, was also included. Then, several criteria were followed: (*a*) the selected wavenumber must describe one secondary structure without the contribution of another one, except for α-helices, although it is difficult to discriminate from non-ordered structures contribution; (*b*) they must have a good signal-to-noise ratio; and (*c*) they must be far from isosbestic points. When all curves were obtained, the distribution function was calculated by a slightly different mathematical procedure to that applied to the amide II, for the reason that monitoring the intensity at a position inside the amide I band will not yield a zero value after complete exchange. This is because amide I only shifts a few cm^{-1}, and the exchanged band will still cause similar absorbance in the same region than the initial band. In other words, ideal exchange kinetics will reach a non-zero flat baseline at 100% exchange. As a consequence, the contribution of any unexchanged residues to the selected positions in the experimental kinetics will be masked under that unavoidable baseline. Unfortunately, it is not possible to measure in our case the amide I spectrum of a 100% exchanged protein (denaturation will lead to a completely different amide I spectrum), and therefore our approach is limited to the hydrogens that show measurable exchange during the experiment. In this context, side-chain subtraction though the use of synthetic spectra did not add information to the results, because the quantitative analysis is already prevented and it only changes the value of the baseline contribution. Therefore, no side-chain subtraction was made for the amide I band. For the distribution calculation, a non-weighted zero order Tikhonov regularization was used (43), and a baseline was

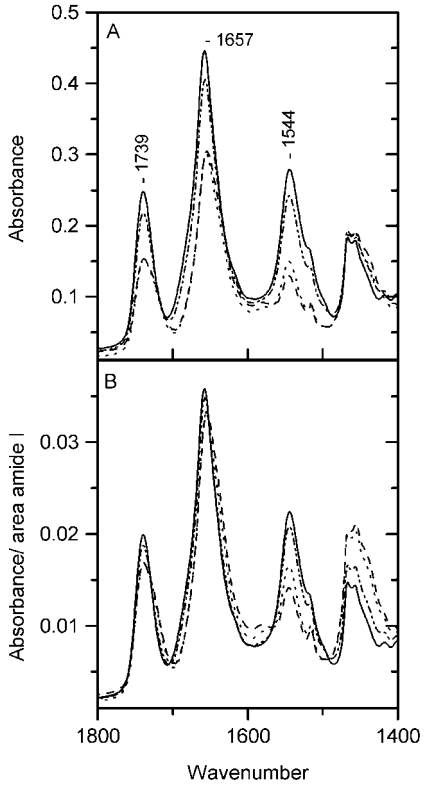

FIG. 1. **ATR-FTIR spectra of MelB in the 1800–1400 cm^{-1} region.** *A*, ATR-FTIR spectra in the 1800–1400 cm^{-1} region of a 150-μg film of MelB initially in buffer (20 mM MES, 10 mM KCl, and pH 6.6) recorded before the onset time exposure (t = 0 min) and after different time periods of exposure of the film to ^2H_2O-saturated N_2 gas at t = 0 min (*solid lines*), t = 2.5 min (*dashed and dotted lines*), t = 34 min (*dotted lines*), and t = 770 min (*dashed lines*). *B*, the spectra shown in *A* were corrected for film inflation using the amide I area (1696–1600 cm^{-1}) as internal standard and plotted as the ratio of absorbance/amide I area. In all instances, spectra were corrected for water atmospheric contribution.

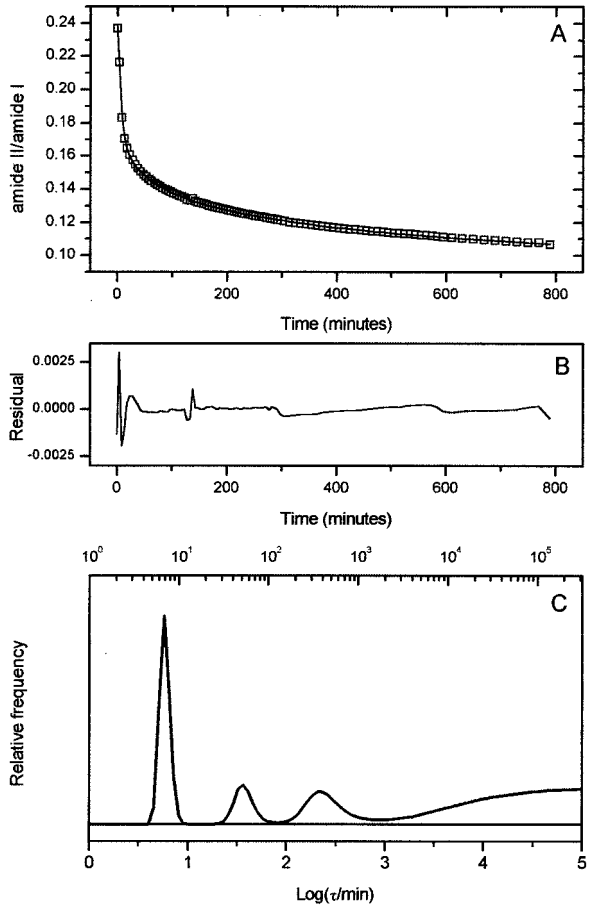

FIG. 2. **Kinetics of H/D exchange of the amide II of MelB without added substrates.** *A*, amide II/amide I ratio of MelB film in buffer (20 mM MES, 10 mM KCl, and pH 6.6). The data were corrected for film inflation and for contribution of lipid and side chains. The *solid line* represents the fit adjusted to the kinetic decay curve by a regularized inverse Laplace transform. *B*, residual obtained by the subtraction of the kinetic curve and mathematical fit. The graphic is expanded 100 times compared with *A*. *C*, distribution function of the exchange rate obtained by inverse Laplace transform of the exchange decay curve of *A*.

included. This weighting allows the distribution to reflect only features that cannot be assigned to a baseline. Only the features that show reproducibility between two different samples were considered. The reported errors refer to the standard errors from independent experiments in the same conditions (n = 2–3).

RESULTS

The kinetics of H/D exchange of MelB was investigated on purified MelB permease reconstituted in liposomes. To study the influence of substrate binding on the deuteration process, the proteoliposomes were equilibrated in media of given composition that led to the formation of specific MelB complexes: (i) a H^+·MelB binary complex in Na^+- and sugar-free medium; (ii) a Na^+·MelB binary complex in sugar-free medium containing 10 mM NaCl; (iii) a H^+·mel·MelB ternary complex in Na^+-free medium containing 5 mM melibiose; (iv) and finally a Na^+·mel·MelB ternary complex in medium containing 10 mM NaCl and 5 mM melibiose (2).

Amide II Signal and Kinetics of Overall H/D Exchange of MelB Permease—The time course of MelB deuteration that takes place on flushing a stream of N_2 saturated with ^2H_2O on dried films of MelB proteoliposomes was investigated by recording the variation of the ATR-FTIR spectra in the 1800–1400 cm^{-1} region as a function of time. The specific experiment illustrated in Fig. 1*A* was carried out on H^+·MelB binary complex preparations. The ATR-FTIR spectra were recorded before (*spectrum 1*) and at selected times after starting deuteration (*spectra 2–4*). All spectra display three major absorption peaks, at around 1739 cm^{-1} (phospholipids), 1657 cm^{-1} (amide I), and 1544 cm^{-1} (amide II), respectively. When the deuteration process starts, the amide II band shifts about 100 cm^{-1} downward (named amide II′) overlapping the band situated at 1460 cm^{-1} (corresponding mostly to CH_2 scissoring). As reported previously (29), part of the decrease in absorbance of all bands observed in the first two spectra of Fig. 1*A* (*spectra 2* and *3*) after the onset of deuteration can be attributed to film inflation. This effect is due to increasing hydration of the film, which induces swelling of the proteoliposomes stacked on the germanium crystal, causing exclusion of a fraction of them from the evanescent beam path. Fig. 1*B* shows the same spectra corrected for film inflation using the amide II/amide I ratio as normalizing factor (see "Experimental Procedures"). On comparing the third and fourth spectra, no further decrease in the C=O and amide I bands can be observed, whereas the amide II band continues decreasing. From these observations, it can be deduced that after 35 min film swelling is over, while H/D exchange continues.

The overall structure accessibility of proteins to ^2H_2O can be assessed by examining the time-dependent variation of the corrected amide II signal (31) integrated between 1565 and 1525 cm^{-1}. Fig. 2*A* shows the change in amide II signal recorded from the H^+·MelB binary complex. At the end of the experiment, the amount of amide hydrogens exchanged is about 55%. The distribution function of the amide proton ex-

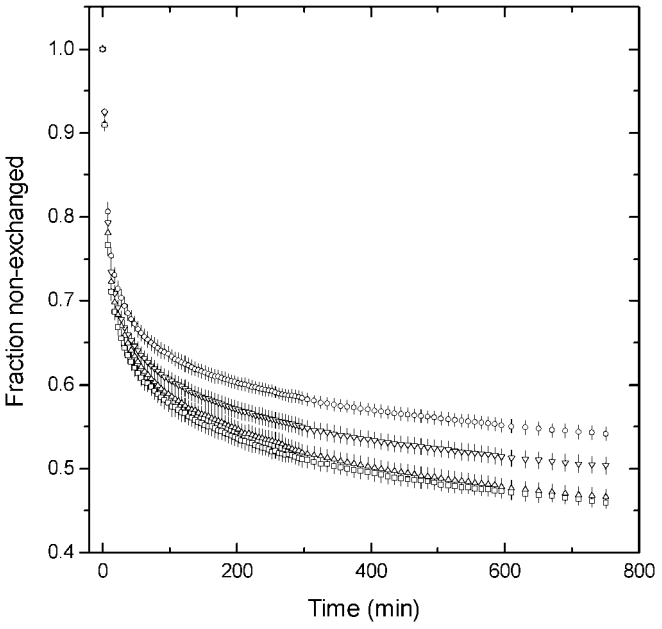

FIG. 3. **Kinetics of H/D exchange of the amide II band of MelB in buffer (20 mM MES, 10 mM KCl, and pH 6.6), in different substrate conditions.** *Symbols*: without added substrates (△); with NaCl 10 mM (□); with melibiose 5 mM (○); and with melibiose 5 mM plus NaCl 10 mM (▽). All the spectra of the kinetics were corrected for film inflation, lipid, and side chain absorption and water atmospheric contributions. The *bar* represents the standard error calculated from $n = 3$ experiments.

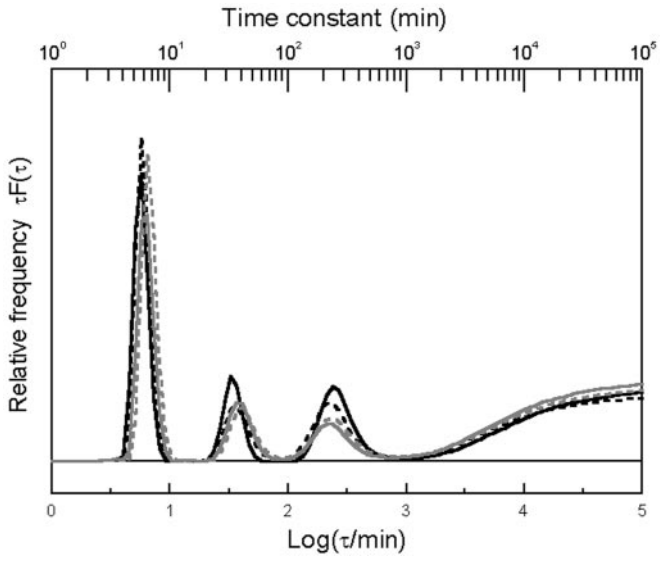

FIG. 4. **Distribution functions of the amide II exchange rates of MelB in buffer (20 mM MES, 10 mM KCl, and pH 6.6), in different substrate conditions.** *Symbols*: without added substrates (*black*), NaCl 10 mM (*dashed black*), melibiose 5 mM (*gray*), and 5 mM melibiose plus 10 mM NaCl (*dashed gray*), obtained by inverse Laplace transform of the averaged decay kinetics.

changed kinetics was obtained by a regularized inverse Laplace transform of the experimental data (Fig. 2*C*). This distribution resolves four components or pools with different time-exchange constants. Within the time window of the experiment, the three first pools can be considered as amide-proton exchangeable pools: a fast exchanging pool that exchanges with a time-constant of about 6 min, an intermediate exchange at 35 min, and a slow exchange at 235 min. The last one is a very slowly exchanging pool with a time constant higher than 1000 min and may represent either the actually non-exchangeable protons or any fraction that does not significantly exchange during the time window of the analysis. The direct Laplace transform of the distribution function is presented as a *continuous line* in Fig. 2*A*, where it is apparent that it fits the experimental data. The difference between the experimental data and the fitted data shown in Fig. 2*B* is considered as noise in the calculation of the distribution function.

Previous fluorescence and FTIR spectroscopy studies have shown that individual or concomitant addition of MelB substrates triggers overall or more localized change(s) of MelB conformation (13, 19, 20, 35). To analyze if modification of the overall H/D exchange properties of MelB (extent and time course) or of the given components of its secondary structure accompanies the substrate-induced structural variations, we first compared the H/D exchange kinetics of whole amide II for different MelB complexes. Fig. 3 shows the kinetic data recorded from each MelB complex. At 770 min, the total amount of MelB H/D exchange of H^+·MelB or Na^+·MelB binary complexes are similar, about 54% (*circle* and *square symbols*, respectively). In contrast, that of the H^+·mel·MelB ternary complex is decreased by 8% compared with that of the binary complexes (*downward triangle*; 46% of exchange). An intermediary reduction (4%) of the extent of H/D exchange of the Na^+·mel·MelB ternary complex is observed (*upward triangle*; 50% of exchange). These results strongly point out for a protective effect of the sugar on MelB permease toward H/D exchange. Possible unspecific effects of melibiose binding were discarded by analyzing the effect of saccharose (5 mM), which is not a substrate of MelB (18): No differences were found in the H/D exchange kinetics or extent, between the H^+·saccharose·MelB and H^+·MelB complexes (data not shown).

We then compared the distribution functions of the amide II H/D exchange kinetic data recorded from the different MelB complexes, to look for any influence of the substrates on the time constant and/or size contribution of the MelB kinetic pools (Fig. 4 and Table I). Similar distribution functions are found for all complexes, with time constants and sizes of the different pools of exchanged protons being comparable. However, some trends are apparent. One of these is the tendency of MelB incubated with melibiose (H^+·mel·MelB) to have kinetic components of reduced size as compared with H^+·MelB, especially evident for the slow pool (Table I). On the other hand, MelB incubated with Na^+ shows that the fast pool increased in size as compared with the rest of the samples. In addition, MelB incubated with both substrates (Na^+·mel·MelB) has the first two kinetic components slower than the H^+·MelB or Na^+·MelB binary complexes. In keeping with previous conclusions (13), these results indicate that binding of any of the substrates, alone or both together, induce conformational rearrangements that are evidenced by changes in H/D exchange characteristics.

Amide I Signal and H/D Exchange at the Secondary Structure Level—As it is known, the intensities at selected wavenumbers of the protein amide I band are good reporters of the contribution of individual structural components (turns, α-helices, or β-sheet structures) to the overall H/D exchange process (29). These representative wavenumbers of the MelB amide I are apparent on examining the differences between deconvoluted spectra obtained from the spectra of Na^+·mel·MelB ternary complex at selected times of the exchange kinetics (Fig. 5*A*). Difference spectra of MelB showed a similar profile for every substrate condition (although small differences on the shape are present, data not shown). Negative intensities (as 1678 cm^{-1} for example) are due to the disappearance of exchangeable amide hydrogens; positive intensities are due to the appearance of deuterated structures. From these observations

TABLE I
Exchanging components obtained following intensity changes of the amide II of MelB films under four different substrate conditions upon exposure to ^2H_2O

Amide II components		H^+	Na^+	H^+ · melibiose	Na^+ · melibiose
Fast	Time constant (min)	5.6 ± 0.2[a]	5.8 ± 0.4	6.1 ± 0.2	6.5 ± 0.3
	Area (%)	26.7 ± 0.9	29.4 ± 0.6	25.0 ± 1.0	28.2 ± 0.8
Intermediate	Time constant (min)	34 ± 2	35 ± 2	38 ± 3	40 ± 2
	Area (%)	10.4 ± 0.4	8.9 ± 1.2	9.1 ± 0.6	8.6 ± 0.5
Slow	Time constant (min)	240 ± 20	220 ± 20	220 ± 20	235 ± 15
	Area (%)	15.5 ± 0.4	14.3 ± 0.8	9.6 ± 0.5	11.3 ± 0.4
Non-exchangeable	Time constant (min)	>1000	>1000	>1000	>1000
	Area (%)	47.4 ± 0.9	47.5 ± 2.0	56.2 ± 1.1	52.0 ± 0.5

[a] All errors refer to standard errors obtained from independent samples in the same conditions for $n = 2$ or 3 experiments.

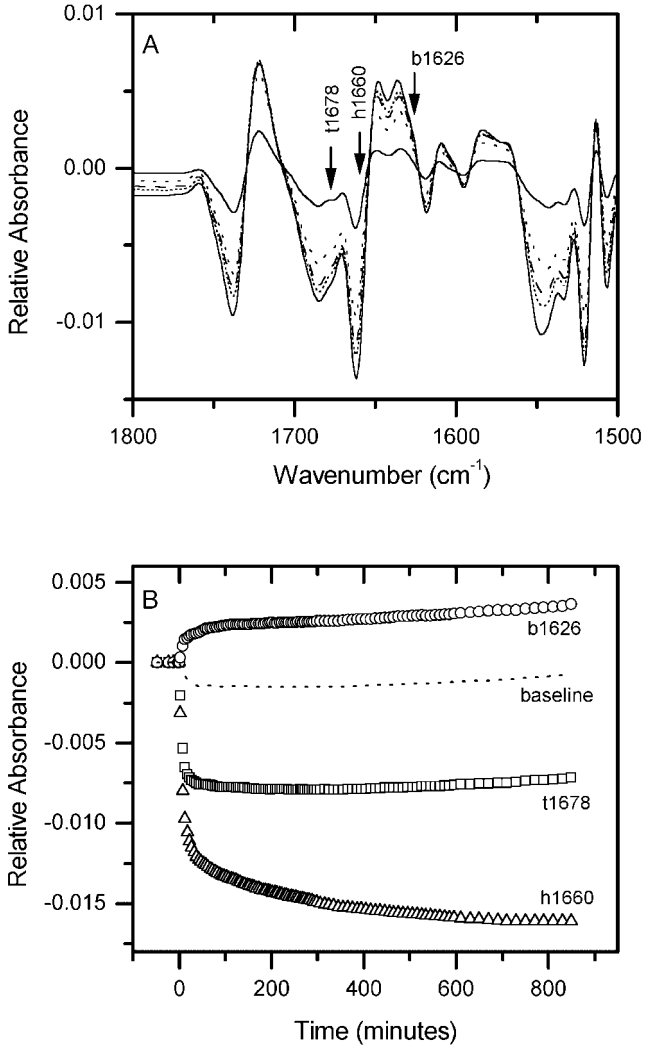

FIG. 5. **Analysis of amide I exchange kinetics.** MelB in buffer (20 mM MES, 10 mM KCl, and pH 6.6) was incubated with 5 mM melibiose and 10 mM NaCl. *A*, difference of the deconvoluted spectra at several times during H/D exchange kinetics in the 1800–1500 cm^{-1} region. *Arrows* point at 1678 cm^{-1} and 1660 cm^{-1} (disappearance of hydrogenated structures) and at 1626 cm^{-1} (appearance of deuterated structures) that are the positions used to measure each secondary structure and plotted in *B*. *B*, changes in the intensity of the difference spectra shown in *A* upon H/D exchange. Data were obtained by deconvolution of all recorded spectra and subtracted from the first unexchanged spectrum of the kinetics before ^2H exposure.

and previous FTIR studies on MelB (13), we selected wavenumber 1678 cm^{-1} to monitor turns, because it has a good intensity and it is far from the β-strand contribution at 1682 cm^{-1}. For α-helices plus non-ordered structure, the wavenumber 1660 cm^{-1} was preferred to 1655 cm^{-1}, because this last value is very near an isosbestic point. Finally, 1626 cm^{-1} rather than 1623 cm^{-1} was used to monitor changes in β-strands because variations at 1623 cm^{-1} were of small amplitude. To improve the accuracy of the intensity measurement, a baseline at 1860 cm^{-1} was chosen, because there is no sample absorbance at this wavenumber. Fig. 5*B* illustrates the time course of the signal variations recorded at these three specific wavenumbers of the amide I region during H/D exchange kinetics.

To assess how each structural component contribution is dependent on the substrates, we recorded the variation of the signal at 1623, 1660, and 1678 cm^{-1} from each MelB complex. Fig. 6 shows that the amount of exchange of the β-strands signal (at 1626 cm^{-1}, *top*) depends on one or more substrates in a manner reminiscent of the total amide II signal variations (see Fig. 3). Thus, it is high for the Na^+·MelB binary complex, intermediate for the H^+·MelB and Na^+·mel·MelB complexes, and small for the H^+·mel·MelB. In this latter case, a relative decrease in accessibility of about 40% is observed as compared with MelB without sugar (H^+·MelB). Fig. 6 (*middle panel*) shows that H/D exchange of α-helices + non-ordered structures (1660 cm^{-1} signal) appears to be slightly lower than the rest of samples, following the same tendency of β-strands. Finally, substrate incubation, either individually or in combination, only produced slight variations of reverse turns (signal at 1678 cm^{-1}, *bottom*).

Further insight can be gained by comparing the decay kinetics of the individual secondary structure signals among the different substrate conditions. Therefore, the regularized inverse Laplace transform procedure was applied to the experimental H/D kinetic curves recorded at the three selected wavenumbers for the different MelB complexes (Fig. 7). Before comparing the changes induced by substrates, an accurate analysis of the errors involved in data acquisition, data analysis, and sample-to-sample repeatability was performed. First, the confidence interval was established by Monte-Carlo simulations ($n = 20$; the difference between experimental data and fitted decay was taken as input noise for simulations), thereby obtaining the uncertainty on the time constant caused by experimental noise. Second, systematic errors were estimated by comparing time constants of two independent experiments. The total error was taken to be as the highest value from both sources of errors. As a conclusion of this analysis, only the first kinetic pools (time constant below ~30 min) showed differences among substrate conditions higher than the error, and thus were the only ones considered.

Fig. 7 shows typical distribution functions of H/D exchange obtained upon different substrate conditions, for each structure type. The largest differences in the fast component among the different substrate conditions are noted for β-sheets. The H^+·MelB and Na^+·MelB complexes display the fast component

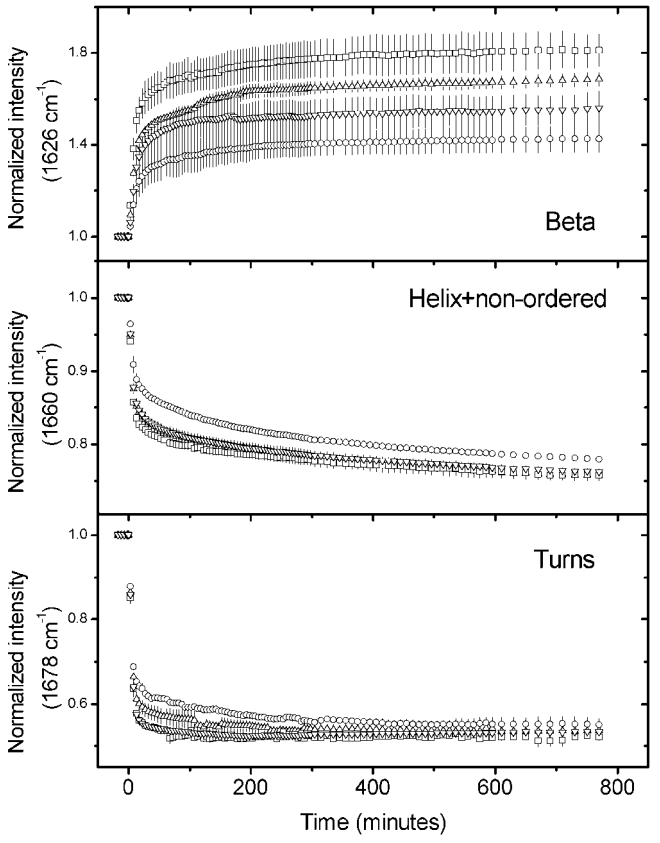

FIG. 6. **H/D exchange kinetic curves of secondary structure components of MelB upon different substrate conditions.** The *symbols* correspond to: MelB in buffer (20 mM MES, 10 mM KCl, and pH 6.6) without added substrates (△); with 10 mM NaCl (□); with 5 mM melibiose (○); and with 5 mM melibiose and 10 mM NaCl (▽). *Top*: intensity monitored at 1626 cm^{-1} representing β-sheet secondary structure. *Middle*: intensity monitored at 1660 cm^{-1} representing α-helices and non-ordered structures. *Bottom*: intensity monitored at 1678 cm^{-1} representing turns. The *vertical scale* has been set to arbitrary values for each panel.

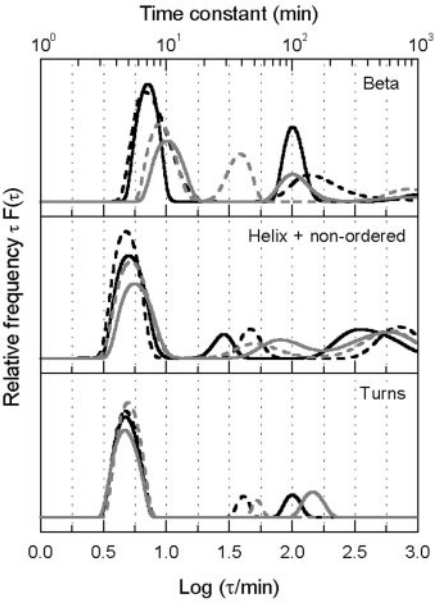

FIG. 7. **Distribution functions of the secondary structures exchange rates of MelB upon different substrate conditions.** The *symbols* correspond to: MelB in buffer (20 mM MES, 10 mM KCl, and pH 6.6) without added substrates (*black*); with 10 mM NaCl (*dashed black*); with 5 mM melibiose (*gray*); and with 5 mM melibiose plus 10 mM NaCl (*dashed gray*) obtained by an inverse Laplace transform of the averaged decay kinetic curves. The *vertical scale* has been set to arbitrary values for each panel.

at about 7 min, whereas this component is shifted to 8.9 min for the Na^+·mel·MelB complex and to 10.2 min for H^+·mel·MelB. In the case of α-helices plus non-ordered structures, the fastest component shows smaller differences. For the Na^+·MelB complex, the time constant is centered at 4.9 min, whereas for the rest of the complexes it is around 5.2 min. When analyzing turns, only small differences were observed among the samples, which show time constants for the fast component centered at about 4.7 min.

DISCUSSION

In this work, analysis of H/D exchange kinetics in both amide I and II regions of MelB has been used to investigate conformational changes of the permease upon different substrate conditions. To date, kinetics of H/D exchange of membrane proteins have only been undertaken in a very limited number of cases, restricted to the analysis of the amide II region (25, 46, 47). However, this technique has been demonstrated to be a useful tool for studying kinetic processes taking part in several soluble proteins (29–31). Its application appears to be particularly useful to document the dynamical properties of membrane proteins that are, in general, largely unknown.

Four representative substrate conditions were chosen for this study, depending on which cation is bound to MelB (proton or sodium), or if the disaccharide melibiose is present or not. Intrinsic fluorescence and FTIR studies already suggested that MelB substrates trigger structural variations of the carrier (13, 18). Both, the kinetics of global H/D exchange (based on the amide II band), and the exchange at the level of the different secondary structures (based on the amide I components) have been examined.

The results based on the amide II monitoring provide information on the whole protein. Extrapolation from data obtained up to 770 min shows that MelB is a relatively accessible protein, having an H/D exchange at 24 h of about 60%. It should be pointed out that in a previous report (13) the H/D exchange at 24 h was calculated to be about 80%, but no correction for the side-chain absorption was made for that calculation. Once corrected for such a contribution, Dave *et al.*'s (13) estimate becomes consistent with the result reported here. The extent of H/D exchange of MelB is lower than that reported for other polytopic membrane transporters of hydrophilic substrates, such as glucose erythrocyte carrier (85%) (48), lactose permease from *E. coli* (95%) (49), or the mitochondrial ADP/ATP transporter (85%) (42).

Comparison of the exchange levels after 24 h strongly suggests that the binding of sugar substrate significantly reduces the accessibility of MelB to the solvent. Both the total amount of H/D exchange and the Laplace transforms of exchange kinetics show a systematic sugar-induced reduction of the size of all different proton exchangeable populations and corresponding increase in the non-exchangeable pool size (see Table I). Therefore, it can be deduced that the structural/dynamical changes induced by melibiose have the effect of a total protection of some amino acids that were highly or partially accessible before the addition of melibiose. These results, indicating increased compactness of the protein, agree with the observation of a higher stability of MelB purified in the presence of melibiose (34). In the absence of sugar, the amount of H/D exchange is comparable whether MelB is incubated with sodium ions (Na^+·MelB) or not (H^+·MelB), whereas binding of both substrates (Na^+·mel·MelB) gives rise to an intermediate situation. On the other hand, differences in the distribution functions (see Table I) indicate that Na^+ and/or melibiose bind-

ing induce structural rearrangements that give rise to changes of accessibility properties (number of components, time constants) among the already exchangeable amide protons. These observations agree with the fact that incubation of MelB with at least 10 mM sodium ions modifies MelB affinity for its sugar substrate, most likely because of a modification of the permease structure (18, 34, 35). However, our data indicate that interaction of Na^+ with MelB induces a limited rearrangement of the transporter structure that does not end up in a radical modification of its H/D exchange characteristics.

The analysis of the H/D exchange kinetics of each secondary structure reveals differences that cannot be appreciated when studying only the amide II region. Particularly, β sheet structures present clear differences depending on MelB condition. In keeping with the conclusions obtained from amide II analysis, MelB incubated with melibiose and proton (Na^+·mel·MelB) presents the more protected situation. α-Helices plus non-ordered structures are also protected by sugar binding, but to a smaller extent (see Fig. 7, *middle*).

The most significant trend of our results is the finding of a protective effect of the sugar melibiose against H/D exchange. Despite the complex corrections applied to the experimental data, the errors are sufficiently low to conclude that this effect takes place mainly at the level of β sheet structures, although α-helices plus non-ordered structures also show the same tendency. In the absence of direct structural information on MelB, the location of these β sheet domains can only be speculative. Secondary structure prediction and a variety of experimental studies have led to a topological model of MelB permease consisting of 12 transmembrane helices (2, 7–10). Of particular interest for the present discussion are several features of two cytoplasmic loops, namely loop 4–5 (connecting helices IV and V) and loop 10–11 (connecting helices X and XI). Secondary structure prediction suggests that both loops have significant β-sheet content. Together, loops 4–5 and 10–11 are large enough to account for the β sheet domains that loose H/D exchange capacity in the presence of sugar. In addition and irrespective of whether MelB has a common or two separate co-substrate binding sites, these two loops are believed to be close to each other (12, 50).

Previous results indicate that some of the residues of these loops may play a role in MelB transport. Thus, Arg^{141} in loop 4–5 is specifically labeled by a photoactivable analogue of melibiose (11). We also recently observed that replacing Arg^{141} by a neutral residue selectively inactivates the substrate translocation step.[2] However, Botfield and Wilson (7) identified several point mutations in loop 10–11 altering MelB function. Strikingly and in a manner reminiscent to Arg^{141} substitution, substrate translocation is again selectively impaired on neutralizing the negative charge at position 365 in loop 10–11 (2). In light of these features, we hypothesize that loop 4–5 and eventually part of loop 10–11 may be β-sheet-containing mobile loops, which orient toward the protein interior once melibiose binds somewhere in a neighboring sugar binding site putatively located between helices IV and XI (19–21). The observation that MelB substrate cooperatively protects loop 4–5 against proteolysis or that loop 10–11 is particularly resistant to proteolytic cleavage (10) is consistent with this suggestion. Whether these loops are dynamic or permanent re-entrant loops is an attractive hypothesis raised by the recent demonstration of the existence of re-entrant loops in both bacterial and eucaryotic transporters, particularly the glutamate transporters (51).

It should finally be mentioned that alignment of the amino acid sequence of homologous transporters composing the galactosides-pentoses-hexuronides family (52, 53) supports the existence of conserved motifs in almost every loop 4–5 (^{132}(P/G)X_4DXRER^{141}) and in cytoplasmic loop 10–11 (^{351}DX_2(E/D)YGX_6R^{364}). These data further emphasize the potential functional/structural importance of the loops with significant β-sheet content for sugar transport.

[2] Abdeldayem, M., Basquin, C., Pourcher, T., and Leblanc, G., manuscript in preparation.

REFERENCES

1. Yazu, H., Shiota-Niiya, S., Shimamoto, T., Kanazawa, H., Futai, M., and Tscuchiya, T. (1984) *J. Biol. Chem.* **259,** 4320–4326
2. Pourcher, T., Bassilana, M., Sarkar, H. K., Kaback, H. R., and Leblanc, G. (1990) *Philos. Trans. R. Soc. Lond-Biol. Sci.* **326,** 411–423
3. Poolman, B., and Konings, W. N. (1993) *Biochim. Biophys. Acta* **1183,** 5–39
4. Reizer, J., Reizer, A., and Milton, H. S. (1994) *Biochim. Biophys. Acta* **1197,** 133–166
5. Damiano-Forano, E., Bassilana, M., and Leblanc, G. (1986) *J. Biol. Chem.* **261,** 6893–6899
6. Bassilana, M., Pourcher, T., and Leblanc, G. (1988) *J. Biol. Chem.* **263,** 9663–9667
7. Botfield, M. C., and Wilson, T. H. (1989) *J. Biol. Chem.* **264,** 11649–11652
8. Pourcher, T., Bibi, E., Kaback, R., and Leblanc, G. (1996) *Biochemistry* **35,** 4161–4168
9. Botfield, M. C., Naguchi, K., Tsuchiya, T., and Wilson, T. H. (1992) *J. Biol. Chem.* **267,** 1818–1822
10. Gwizdek, C., Leblanc, G., and Bassilana, M. (1997) *Biochemistry* **36,** 8522–8529
11. Ambroise, Y., Leblanc, G., and Rosseau, B. (2000) *Biochemistry* **39,** 1338–1345
12. Cordat, E., Leblanc, G., and Mus-Veteau, I. (2000) *Biochemistry* **39,** 4493–4499
13. Dave, N., Troullier, A., Mus-Veteau, I., Duñach, M., Leblanc, G., and Padrós, E. (2000) *Biophys. J.* **79,** 747–755
14. Wilson, D. M., and Wilson, T. H. (1992) *J. Bacteriol.* **174,** 3083–3086
15. Hama, H., and Wilson, H. (1993) *J. Biol. Chem.* **268,** 10060–10065
16. Pourcher, T., Zani, M. L., and Leblanc, G. (1993) *J. Biol. Chem.* **268,** 3209–3215
17. Wilson, D. M., and Wilson, T. H. (1994) *Biochim. Biophys. Acta* **1190,** 225–230
18. Mus-Veteau, I., Pourcher, T., and Leblanc, G. (1995) *Biochemistry* **34,** 6775–6783
19. Mus-Veteau, I., and Leblanc, G. (1996) *Biochemsitry* **35,** 12053–12060
20. Cordat, E., Mus-Veteau, I., and Leblanc, G. (1998) *J. Biol. Chem.* **273,** 33198–33202
21. Ding, P. Z., and Wilson, T. H. (2000) *J. Membr. Biol.* **174,** 135–140
22. Knox, D. G., and Rosenberg, A. (1980) *Biopolymers* **19,** 1049–1068
23. Gregory, R. B., and Lumry, R. (1985) *Biopolymers* **24,** 301–326
24. Clarke, J., and Itzhaki, L. S. (1998) *Curr. Opin. Struct. Biol.* **8,** 112–118
25. Goormaghtigh, E., Vigneron, L., Scarborough, G. A., and Ruyssachaert, J. M. (1994) *J. Biol. Chem.* **269,** 27409–27413
26. De Jongh, H. H. J., Goormaghtigh, E., and Ruyssachaert, J. M. (1995) *Biochemistry* **34,** 172–179
27. Lumry, R. (1995) in *Protein-Solvent Interactions* (Gregory, R. B., ed) pp. 1–141, Marcel Dekker, New York
28. Goormaghtigh, E., Cabiaux, V., and Ruysschaert, J. M. (1994) *Subcell. Biochem.* **23,** 363–404
29. De Jongh, H. H. J., Goormaghtigh, E., and Ruysschaert, J. M. (1997) *Biochemistry* **36,** 13593–13602
30. De Jongh, H. H. J., Goormaghtigh, E., and Ruysschaert, J. M. (1997) *Biochemistry* **36,** 13603–13610
31. Goormaghtigh, E., Raussens, V., and Ruysschaert, J. M. (1999) *Biochim. Biophys. Acta* **1422,** 105–185
32. Susi, H., Timasheff, S. N., and Stevens, L. (1967) *J. Biol. Chem.* **242,** 5460–5465
33. Timasheff, S. N., Susi, H., and Stevens, L. (1967) *J. Biol. Chem.* **242,** 5466–5473
34. Pourcher, T., Leclercq, S., Brandolin, G., and Leblanc, G. (1995) *Biochemistry* **34,** 4412–4420
35. Maehrel, C., Cordat, E., Mus-Veteau, I., and Leblanc, G. (1998) *J. Biol. Chem.* **273,** 33192–33197
36. Brandolin, G., Doussiere, J., Gulik-Krzywicki, T., Lauquin, G. J., and Vignais, P. V. (1980) *Biochim. Biophys. Acta* **592,** 592–614
37. Botfield, M. C., and Wilson, T. H. (1988) *J. Biol. Chem.* **263,** 12909–12915
38. Rigaud, J. L., Paternostre, M. T., and Bluzat, A. (1988) *Biochemistry* **27,** 2677–2688
39. Lowry, O. H., Rosenbrough, N. J., Farr, A. L., and Randall, R. J. (1951) *J. Biol. Chem.* **193,** 265–275
40. Venyaminov, S. Y., and Kalnin, N. N. (1990) *Biopolymers* **30,** 1243–1257
41. Chirgadze, Yu. N., Fedorov, O. V., and Trushina, N. P. (1975) *Biopolymers* **14,** 679–694
42. Lórenz, V. A., Villaverde, J., Trézéguet, V., Lauquin, G. J.-M., Brandolin, G., and Padrós, E. (2001) *Biochemistry* **40,** 8821–8833
43. Craig, I. J. D., and Brown, J. C. (1986) *Inverse Problems in Astronomy: A Guide to Inversion Strategies for Remotely Sensed Data*, Adam Hilger Ltd., Bristol, England
44. Press, W. H., Teukolsky, S. A., Vetterling, W. T., and Flannery, B. P. (1992) *Numerical Recipes in C: The Art of Scientific Computing*, 2nd Ed., pp.

788–825, Cambridge University Press, Cambridge-NewYork-Melbourne
45. Mantsch, H. H., Moffatt, D. J., and Casal, H. (1988) *J. Mol. Struct.* **173,** 285–298
46. Rath, P., DeGrip, W. J., and Rothschild, K. J. (1998) *Biophys. J.* **74,** 192–198
47. Saba, R. I., Ruysschaert, J.-M., Herchuelz, A., and Goormaghtigh, E. (1999) *J. Biol. Chem.* **274,** 15510–15518
48. Alvarez, J., Lee, D. C., Baldwin, D., and Chapman, D. (1987) *J. Biol. Chem.* **262,** 3502–3509
49. Le Coutre, J., Narasimhan, L. R., Patel, C. K. N., and Kaback, R. (1997) *Proc. Natl. Acad. Sci. U. S. A.* **94,** 10167–10171
50. Ding, P. Z., Botfield, M. C., and Wilson, T. H. (2000) *Biochim. Biophys. Acta* **1509,** 123–130
51. Slotboom, D. J., Konings, W. N., and Lolkema, J. S. (2001) *FEBS Lett.* **492,** 183–186
52. Poolman, G. T., Knol, J., van der Does, C., Henderson, P. J. F., Liang, W.-J., Leblanc, G., Pourcher, T., and Mus-Veteau, I. (1996) *Mol. Microbiol.* **19,** 911–922
53. Saier, M. H., Jr. (2000) *Microbiol. Mol. Biol. Rev.* **64,** 354–411

Structural and Functional Implications of the Instability of the ADP/ATP Transporter Purified from Mitochondria as Revealed by FTIR Spectroscopy

Víctor A. Lórenz-Fonfría,* Joaquim Villaverde,* Véronique Trézéguet,† Guy J.-M. Lauquin,† Gérard Brandolin,‡ and Esteve Padrós*

*Biophysics Unit, Department of Biochemical and Molecular Biology, Autònoma University of Barcelona, Barcelona, Spain; †Laboratory of Molecular and Cellular Physiology, Institute of Biochemistry and Cellular Genetics, the National Center for Scientific Research, Bordeaux, France; and ‡the Laboratory of Biochemistry and Biophysics of the Integrated Systems, Department of Cellular Answers and Dynamics, French Atomic Energy Commission/Grenoble, Grenoble, France [AQ1]

ABSTRACT The ADP/ATP transporter shows a high instability when solubilized, making it difficult to obtain functional protein with sufficient purity for long-term spectroscopic studies. When solubilized in the detergent dodecyl maltoside the protein is in equilibrium between the so-called CATR and BA conformations and in a few hours it becomes nonfunctional, unable to bind either its inhibitors or its substrates. By Fourier transform infrared spectroscopy, we studied the structural changes involved in this denaturation process. To do so, the carboxyatractyloside-inhibited protein was used as a structural model for the protein in the CATR conformation and its spectrum was compared with that of the unliganded time-inactivated protein. From the difference spectra of the amide I, amide II, and amide A bands combined with dichroism spectra of the carboxyatractyloside-inhibited protein, we concluded that few structural differences exist between both states, affecting as few as 11 amino acids (3.5% of the protein); the structural changes consisted in the disappearance of large loop structure and the appearance of aggregated strands. We hypothesize that some mitochondrial loop (tentatively loop M1) shows a high tendency to aggregate, being responsible for the observed features. The functional consequences of this hypothesis are discussed.

INTRODUCTION

The ADP/ATP transporter is located in the inner mitochondrial membrane, from where it mediates the exchange of cytosolic ADP for ATP generated in the mitochondria. The transporter adopts two structural conformations, which can be detected by its characteristic sensitivity to inhibitors. In the so-called CATR conformation the transporter can be blocked by atractyloside (atr) and carboxyatractyloside (c-atr) acting from the cytosolic side, whereas in the BA conformation the bongkrekic acid (BA) and isobongkrekic acid block the transporter from the matrix side. Both conformations show particular chemical, immunochemical, and enzymatic reactivities, and their interconversions are probably a key feature of the transport process. For further details, see reviews by Brandolin et al. (1993a), Fiore et al. (1998), and Kaplan (1996).

Most of the knowledge about the ADP/ATP transporter has been obtained in experiments performed on mitochondria. In this way, valuable information concerning its function and indirect information about the structural changes involved in the CATR to BA conformation transition has been obtained. However, direct structural information about the ADP/ATP transporter is scarce to date.

Spectroscopic methods can supply part of this information which is currently lacking, provided that the protein is obtained highly pure and in a well-defined conformation. Spectroscopic studies of the ADP/ATP transporter have encountered one major problem: its instability during the purification process (Klingenberg et al., 1995). Since the ADP/ATP transporter is a membrane protein, purification is performed through a solubilized state. In studies performed in very fresh preparations of the solubilized protein, only half of its substrate binding sites are retained (Brandolin et al., 1993b; Krämer and Klingenberg, 1977). Therefore, the solubilized and unliganded ADP/ATP transporter contains a large number of inactive molecules which increase with the time the sample spends solubilized, until reaching full inactivation in a matter of a few hours. The carrier which has lost its capacity to bind ligands in a time-dependent manner will be referred to as *time-inactivated* (Krämer and Klingenberg, 1977). Once reconstituted into liposomes, the transporter remains stable for many hours (Brandolin et al., 1980; Klingenberg et al., 1995). To reduce the time the transporter spends solubilized, the purification procedure can be simplified, so that the reconstituted transporter is obtained only partially purified (50% of contaminating proteins; see Heidkämper et al., 1996; Klingenberg et al., 1995). Obviously, this preparation would not be suitable for spectroscopic analysis. The high instability of the solubilized ADP/ATP transporter entails some questions. Why is it so unstable in the solubilized state? Is the instability related to its function? Which structural changes are responsible for the reduction in the number of binding sites during its isolation?

Submitted November 27, 2002, and accepted for publication March 6, 2003.

Address reprint requests to Esteve Padrós, Unitat de Biofísica, Facultat de Medicina, Universitat Autònoma de Barcelona, 08193 Bellaterra, Barcelona, Spain. Tel.: 34-93-581-1870; Fax: 34-93-581-1907; E-mail: esteve.padros@uab.es.

0006-3495/03/07/1/12 $2.00

In this work, Fourier transform infrared (FTIR) spectroscopy is used, aiming at characterizing the structural changes responsible for the reduction of binding sites during purification of the yeast ADP/ATP transporter from *S. cerevisiae* (Anc2pHis; Fiore et al., 2000). FTIR spectra of proteins contain structural information, mainly encoded in band positions of the amide I, but also in the amide II and amide A vibrations (Bandekar, 1992; Goormaghtigh et al., 1994a; Krimm and Bandekar, 1986). Several guides to assign secondary structure from the position of the amide I components have been published; see Arrondo et al. (1993), Goormaghtigh et al. (1994b), and Tamm and Tatulian (1997).

Theoretically, by comparing FTIR spectra of time-inactivated Anc2pHis and fully functional, noninhibited Anc2pHis, we could have some insights into the structural changes responsible for or concomitant with the reduction of the number of binding sites. However, the noninhibited Anc2pHis can have an important proportion of time-inactivated Anc2pHis, growing during the acquisition of infrared spectra. To overcome this problem we considered that the Anc2p when solubilized in dodecyl maltoside (DM) is obtained in equilibrium between the so-called CATR and BA conformations (Roux et al., 1996). Many experimental evidences point to a high structural similarity between the CATR conformation and the c-atr-inhibited state for the beef heart carrier (Brandolin et al., 1993a). Moreover, the c-atr-inhibited state can be considered as a blocked or trapped CATR conformation (Brandolin et al., 1993a; Klingenberg, 1989; Klingenberg et al., 1995). In addition, the high affinity of the c-atr is compatible with a low structural rearrangement of the protein on binding, according to the induced transition fit theory of transport catalysis (Klingenberg, 1989; Klingenberg et al., 1995).

Therefore, in this work, the c-atr-inhibited state is used as a reference state for the noninhibited Anc2p in the CATR conformation, and its structure is compared with that of the time-inactivated unliganded state. FTIR spectra have been obtained for both states (inhibited and time-inactivated) solubilized in the nondenaturing detergent DM (Roux et al., 1996) in solution and dry film, and reconstituted in egg PC/PA phospholipids (dry film).

MATERIALS AND METHODS

Yeast strains and Anc2pHis purification

We used the genetically modified JL1-3-ANC2(His6) *Saccharomyces cerevisiae* yeast strain, which produced a modified isoform of Anc2p containing the extra sequence GSRSHHHHHH at its C-terminal end (Anc2pHis; Fiore et al., 2000). JL1-3-ANC2(His6) yeast cells were grown as described (Brandolin et al., 1993b). Preparation of yeast mitochondria and purification of Anc2pHis were done as described (Lórenz et al., 2001). All purification steps were carried out at 4°C. Isolated yeast mitochondria were preincubated with carboxyatractyloside (omitted or substituted with atractyloside when the time-inactivated form was purified).

Reconstitution of the Anc2pHis into liposomes

Egg PC/PA (9:1 w/w) presolubilized with DM was added to the purified Anc2pHis at a final lipid-to-protein ratio of 3:1 (w/w) and final DM-to-lipid ratio of 2:1 (w/w). After 1–2 h of incubation at 4°C, Bio-beads were added to a final ratio to DM of 33:1 (w/w). After 6 h of slow stirring at 4°C, the proteoliposomes obtained were centrifuged at 90,000 *g* for 90 min. The pellet was resuspended to the final concentration used in the experiments.

FTIR transmission experiments

Sample preparation

For IR transmission experiments of solubilized samples in solution, the Anc2pHis concentration was 10 mg/ml in DM 9% for the inhibited form, and 15 mg/ml in DM 15% when not inhibited, in Mes 10 mM and NaCl 50 mM (pH 6.8). The sample was placed between two CaF_2 windows using a 6 μm tin spacer. For transmission spectra of dry films of solubilized protein, 0.2–0.1 mg of protein was spread over a CaF_2 window and dried under vacuum.

Spectra acquisition

A total of 1000 scans were co-added in blocks of 40 reference scans and 40 sample scans using a shuttle accessory, with an instrumental resolution of 2 cm^{-1} on a Mattson Polaris FTIR equipped with an MCT detector. The resulting interferogram was apodized with a triangle function, and processed to give absorption spectra at 0.5 cm^{-1} digital resolution. The sample was placed in a circulating water holder connected to a thermostatic bath. An external probe fitted to the sample holder was used to keep the temperature at 25.0°C. The spectrometer compartment was purged with dry air, giving absorption spectra free from water vapor bands.

FTIR attenuated total reflection experiments

Sample preparation

Roughly 40–80 μg of reconstituted Anc2pHis was spread on a 45° trapezoid attenuated total reflection germanium crystal of 50 × 20 × 10 mm. The sample was dried at the atmospheric humidity first, and under a dry nitrogen flow later.

Spectra acquisition

A total of 2000 scans were co-added at an instrumental resolution of 2 cm^{-1} on a Bio-Rad FTS 6000 spectrometer equipped with an MCT detector. The resulting interferogram was apodized with a triangle function, and processed to give absorption spectrum at 0.5 cm^{-1} digital resolution. A cover jacket was placed over the crystal, and connected to a circulating thermostatic bath. The temperature was fixed to 25.0°C, controlled by an external probe fitted to the cover jacket. The spectrometer compartment was purged with dry air. No block averaging was used; under these conditions the presence of residual water vapor peaks in the absorption spectra cannot be fully prevented, so water vapor data were collected and subtracted when needed.

Orientation experiments

Absorption spectra were obtained by using KRS-polarized IR beam parallel (0) or perpendicular (90). The ratio between the total area for a band in both conditions is called the dichroic ratio (R), and is related to the band order parameter of the band transition dipole moment with respect to the crystal normal (p_ϕ; see Eq. 1 in Marsh and Páli, 2001).

When p_ϕ is equal to zero, R is named R_{iso}, which will generally depend on the wavenumber. A dichroism spectrum is obtained as $Abs_{90} - R_{iso}Abs_0$, with the property that only bands having a preferential orientation, different from the magic angle, appears in it. It is thus suited to enhance the resolution of oriented structures of proteins as transmembrane helices. To obtain $R_{iso}(\nu)$, the average values for the electromagnetic fields along the *x*-, *y*-, and *z*-directions should be evaluated. This is a hard task since they depend in a complex way on many parameters, namely: the wavenumber; the angle of the IR beam with the crystal; the refraction index of the crystal; the complex refraction index of the sample; and the thickness of the film over the crystal (Citra and Axelsen, 1996). Under the assumption that the sample is a weak absorber and either the film thickness is much higher than the evanescent wave penetration for all the studied wavenumbers (thick film hypothesis), or it is much lower than the evanescent wave penetration for all the studied wavenumbers (thin film hypothesis), relative expressions can be obtained to evaluate the average electromagnetic fields (Goormaghtigh et al., 1999). If only the weak absorber assumption is made, we can use a semiempirical expression (Eq. 44 in (Goormaghtigh et al., 1999) valid for films outside the thick film and thin film hypothesis. However, we need to evaluate the thickness of the film. To do so we consider the following: Once p_ϕ is obtained, it follows from the properties of the order parameter that for two vibrations from the same molecular structure (e.g., amide I and amide II), the following relation will hold:

$$p_\beta^{\text{Amide I}} = \frac{p_\phi^{\text{Amide I}}}{p_\alpha^{\text{Amide I}}} = \frac{p_\phi^{\text{Amide II}}}{p_\alpha^{\text{Amide II}}} = p_\beta^{\text{Amide II}},$$

where p_α is the order parameter of the transition dipole moment to respect the molecular structure axis and p_β is the order parameter of the molecular structure to respect any other frame of reference with axial symmetry. Since the amide I and amide II bands come from the same molecule their p_β should be equal. For a protein in an α-helix conformation p_α is equal to 0.43 for the amide I and –0.37 for the amide II band (Marsh et al., 2000).

With the information that the order parameter for the transmembrane helices (p_β) obtained from the amide I should be equal to that obtained from the amide II, we can determine the film thickness and the $R_{iso}(\nu)$, and so we can obtain the dichroism spectrum.

Spectral corrections and determination of experimental errors

Buffer subtraction

For transmission experiments in solution, a buffer spectrum was collected and subtracted, to eliminate the contribution of water, detergent, and salts. The subtraction factor was chosen as that leaving a flat baseline between 2000 and 1800 cm^{-1}.

Amino acid side-chain absorption subtraction

A synthetic amino acid side-chain absorption spectrum was constructed (Venyaminov and Kalnin, 1990), taking into account the primary sequence of the Anc2pHis (Le Saux et al., 1996). The subtraction factor was calculated as described (Lórenz et al., 2001).

Phospholipid and DM absorption

The phospholipids used have no significant absorption in the amide I or II, whether between 4000 or 3150 cm^{-1}. DM shows no absorption in the amide I or II, but it does between 3500 and 3100 cm^{-1}. Therefore the amide A, at ~3300 cm^{-1}, is not directly observable for the solubilized protein.

Spectral analysis

Fourier self-deconvolution

It was performed using the program supplied by Spectrum Square Associates, implemented in the GRAMS software (Galactic Industries). The theory of Fourier self-deconvolution (FSD) is well-developed (Lórenz-Fonfría et al., 2002; Moffat and Mantsch, 1992). Our spectra were deconvoluted for a Lorentzian profile of full-width at half-high (FWHH) equal to γ', filtered with a Bessel or a Gaussian function, and a narrowing factor of k (Kauppinen et al., 1981).

Maximum likelihood restoration

It was performed using the program supplied by Spectrum Square Associates, implemented in the GRAMS software (Galactic Industries). Maximum likelihood restoration (MLR) is a nonlinear iterative deconvolution method. Instead of trying to solve directly the deconvolution problem it searches for a solution that, when convoluted by a Lorentzian profile of FWHH equal to γ', matches the experimental spectrum to a certain degree. The method restricts the solution to be positive, but negative values may have a physical meaning if a band if over-deconvoluted or deconvoluted using a wrong profile. To overcome this restriction an offset was added before the analysis and removed after MLR.

Curve-fitting procedures

Curve-fitting was carried out using the program DATAFIT (Spectrum Square Associates) implemented in the GRAMS software. It uses the Levenberg-Marquardt method to find the parameters that yield a minimum χ^2. A maximum of 1000 iterations were used.

The number of bands to fit the amide I were obtained from FSD and MLR spectra. Curve-fitting was performed on deconvoluted spectra. To obtain accurate results on curve-fitting overlapped bands, the form of the component bands should be well characterized. If we assume that amide I component bands are Lorentzian bands, Voigt bands with fixed Gaussian width should be used to fit deconvoluted spectra (Lórenz-Fonfría et al., 2002). If we assume that the amide I component bands have mixed Lorentzian-Gaussian character, Voigt bands with free Gaussian width should be used (Lórenz-Fonfría et al., 2002). Finally, an offset was also included when the fitted spectra contained an absorption-free region.

Calculation and quantification of difference spectra

Difference spectra were obtained by subtracting two absorption spectra with a factor such that the 1700–1610 cm^{-1} interval (amide I) had as much positive as negative area. In transmission experiments, if two identical spectra are subtracted, a zero difference spectrum will be obtained. However, this is not true in attenuated total reflection experiments since the apparent film thickness depends on the actual film thickness and the wavenumber. The consequence is that true difference spectra can only be generally obtained for a short wavenumber interval without artifacts. The quantification of difference spectra was performed in the following way: difference spectra were deconvoluted, and band areas were obtained by integration and/or curve-fitting. In this way the possible area cancellation between positive and negative parts in the difference spectra is minimized. The band areas at the amide I interval were divided by the amide I total area and the same was done for the amide II. This allows us to obtain a percentage of the amino acids involved in the structural changes for both the amide I and amide II.

Fluorescence experiments

Intrinsic fluorescence data was acquired by exciting at 297 nm, using a slit of 4 nm, and collecting at 340 nm with a slit of 16 nm. The sample (1 ml of the

DM-solubilized Anc2pHis at a 0.04 mg/ml) was linearly heated (at 50°C/h) on an AMINCO SLM 8000 fluorimeter (SLM Instruments).

RESULTS

Purity of the samples

The first requirement for this study was to check that the c-atr-inhibited Anc2pHis and the time-inactivated Anc2pHis were obtained pure and in a well-defined state. The SDS-PAGE revealed that the Anc2pHis purity was higher than 95% (not shown). It was more difficult to assure that the protein was obtained in a single conformation. We assumed that the c-atr-inhibited form was almost 100% inhibited, since mitochondria were preincubated with an excess of c-atr, which shows a very high affinity for the Anc2p. An indirect observation of the c-atr binding was obtained from fluorescence experiments. It is known that the intrinsic fluorescence of the Anc2p decreases upon c-atr binding (Brandolin et al., 1993b). When the solubilized c-atr-inhibited Anc2pHis was heated, a fluorescence transition appeared, corresponding to an increase of intrinsic Trp fluorescence (not shown). We assign this fluorescence increase to the release of the c-atr. Moreover, the fluorescence increase was very intense and quite repetitive between different inhibited Anc2pHis purified samples (+99 ± 14%). It is therefore a very sensitive method to detect the presence of c-atr-inhibited Anc2p. When the time-inactivated Anc2pHis (noninhibited or preincubated with the low affinity inhibitor atr) was incubated with ATP (to promote the transition between BA and CATR conformations), c-atr and heated, no fluorescence transition was detected. We concluded that it was totally unable to bind c-atr, and so fully inactivated.

Solubilized Anc2p

Fig. 1 *A* displays the dry film transmittance absorption spectrum of the time-inactivated solubilized Anc2pHis. Previously we have shown that working with dry films does not alter significantly the Anc2pHis structure as revealed by infrared spectroscopy (Lórenz et al., 2001). The amide I appears at 1656.5 cm^{-1} and the amide II at 1545.1 cm^{-1}, which suggests a predominantly helix and/or unordered structure. The spectrum of the inhibited Anc2pHis was presented in a previous work (see Fig. 3 *A* in Lórenz et al., 2001). For the time-inactivated form, the amide I, amide II, and tyrosine appear at a slightly lower wavenumber, suggesting minor structural differences.

Deconvolution and curve-fitting

In Fig 1 *B*, the deconvoluted spectrum of Fig. 1 *A* is presented together with its curve-fitting. In Fig. 1 *C* the deconvoluted spectrum and curve-fitting of the c-atr-inhibited Anc2pHis is displayed for comparative reasons.

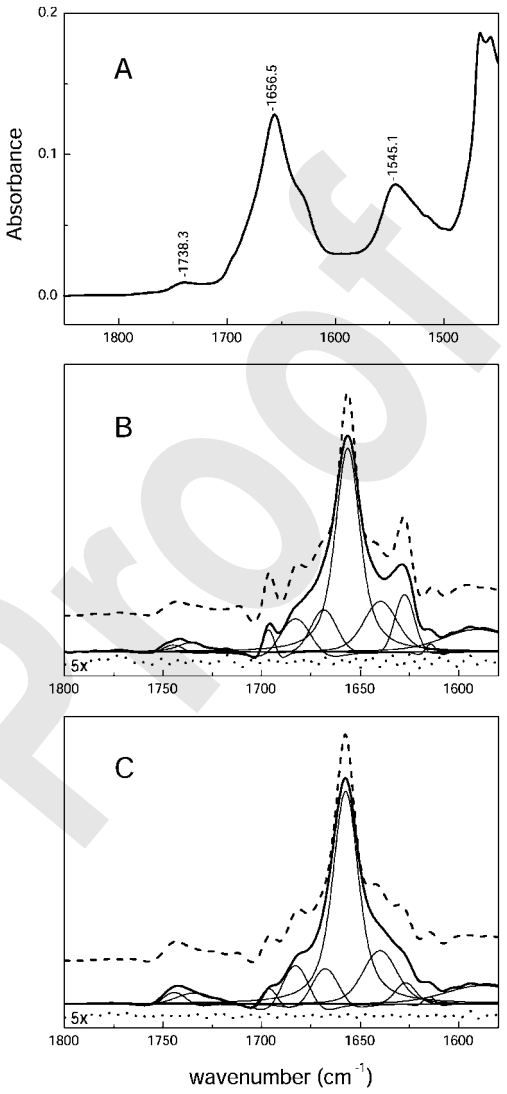

FIGURE 1 (*A*) (——) Transmission absorbance spectrum of a dry film of the DM solubilized time-inactivated Anc2pHis (isolated in the absence of inhibitors), corrected for amino acid side-chain absorption. Spectrum S/N was 2000. (*B*) (- - - - -) MLR ($\gamma' = 18\ cm^{-1}$) of the spectrum in *A*; (——) FSD of the spectrum in (A) ($\gamma' = 18\ cm^{-1}$, $k = 2.0$, and a Gaussian apodization). Curve-fitting was performed with Voigt profiles allowing for optimizing Lorentzian-Gaussian character (as described in Materials and Methods). Fit results are presented in Table 1. (·····) Curve-fitting residual in an enhanced scale and shifted down for a clearer display. (*C*) (- - - - -) MLR ($\gamma' = 18\ cm^{-1}$) of the c-atr-inhibited Anc2pHis. (——) FSD of the c-atr-inhibited Anc2pHis ($\gamma' = 18\ cm^{-1}$, $k = 2.0$, and a Gaussian apodization). Curve-fitting was performed with Voigt profiles allowing for an unknown Lorentzian-Gaussian character. Fit results are presented in Table 1. (·····) Curve-fitting residual in an enhanced scale and shifted down for a clearer display.

The most striking differences of Fig. 1 *B* with respect to Fig. 1 *C* are the prominent bands at 1628 cm^{-1} and 1696 cm^{-1} in the noninhibited Anc2pHis, usually observed in aggregation processes induced by temperature (Heimburg and Marsh, 1993). These changes, however, result in only slight differences in the individual band positions, widths and areas, as presented in Table 1. Only three bands change their

TABLE 1

Noninhibited Anc2pHis			Inhibited Anc2pHis				
Position*	FWHH*	Area†	Position*	FWHH*	Area†	ΔArea	Assignments
1696.5 ± 0.1	9 ± 0.5	0.8 ± 0.2	1696.2 ± 0.2	12 ± 0.5	0.7 ± 0.2	+0.1 ± 0.3	β-sheets
1682.8 ± 0.9	22 ± 2	4.9 ± 0.8	1682.9 ± 0.6	19 ± 1	4.5 ± 0.6	+0.4 ± 0.8	turns
1668.5 ± 1.0	24 ± 1	9 ± 0.8	1667.7 ± 1.1	21 ± 1	5.5 ± 0.6	+3.5 ± 1.0	turns
1656.3 ± 0.1	27 ± 0.5	59 ± 1.3	1657.4 ± 0.1	28 ± 0.5	66.3 ± 1.1	−7.3 ± 1.7	α-helix + unordered
1639.7 ± 0.6	31 ± 2	17.4 ± 1.9	1639.9 ± 0.4	31 ± 2	18.8 ± 1.7	−1.4 ± 2.5	β-sheets
1627.4 ± 0.3	20 ± 1	8.9 ± 1.7	1627.0 ± 0.5	22 ± 1	4.1 ± 1.2	+4.8 ± 2.1	β-sheets

Summary of the curve-fit to deconvoluted spectra of noninhibited (Fig. 1 *B*) and carboxyatractyloside-inhibited (Fig. 1 *C*) Anc2pHis in dry film, together with band area differences between both states and band assignments. The errors are standard deviations obtained from Monte Carlo simulations.
*In cm^{-1}.
†Area percentage with respect to all amide I bands.

area significantly: the bands at 1668, 1656, and 1627 cm^{-1}. The secondary structure estimation also presents small changes between the time-inactivated form and the c-atr-inhibited form. If we assume the amide I area to be directly related to the percentage of secondary structure, the structural changes between the inhibited and time-inactivated form are: $\Delta(\alpha\text{-helix} + \text{unordered}) = -7.3 \pm 1.7\%$; $\Delta\beta\text{-sheets} = +3.4 \pm 1.5\%$; and $\Delta\text{turns} = +3.9 \pm 0.8\%$.

Difference spectra

Fig. 2 *A* presents the transmittance absorption spectra for the DM solubilized time-inactivated Anc2pHis and c-atr-inhibited Anc2pHis (scaled to have the same area in the amide I), together with their difference spectra. The difference spectra obtained is rather simple (see Fig. 2 *B*), with only one very well-defined band disappearing in both amide I and amide II regions, and two bands appearing in the amide I and one band in the amide II. After Fourier self-deconvolution of the difference spectrum (see Fig. 3 *A*), the bands appeared more defined but no additional bands were detected. Since the changes in the amide I and amide II regions are of the same type, and the negative and positive bands can be assigned to secondary structures from their position (α-helix + nonordered and β-sheets respectively), we conclude that the difference spectrum comes from changes in the amino acid peptide bond vibration (and not from amino acid side-chain groups, which would cause different effects in the amide I and the amide II regions). The difference consists in some peptide bonds changing from a secondary structure with amide I and amide II bands at 1662 cm^{-1} and 1548 cm^{-1} respectively, to another secondary structure giving amide I bands at 1627 cm^{-1} and 1697 cm^{-1} and an amide II band at 1522 cm^{-1}. From the area differences obtained from the deconvoluted spectrum in both amide I and amide II, we can conclude that ~3.5% of the amino acids of the protein (≈11 amino acids) are involved in the structural changes. This value is not far from that determined from the curve-fitting of the deconvoluted spectra for the time-inactivated and c-atr-inhibited forms (7%, 22 amino acids), as shown in Table 1. According to the hypothesis that the structure of the c-atr-inhibited form is similar to the *CATR* conformer, the structural changes concomitant with the loss of binding sites are the following: formation of intermolecular antiparallel β-sheets (bands appearing at 1697, 1627, and 1522 cm^{-1}), at the expense of some helix or unordered structure (bands disappearing at 1662, and 1548 cm^{-1}). From Fig. 2 *B* it seems that the number of turns does not significantly vary in the transition to the inactive state. Nevertheless, since turns do not give a single defined vibration, their changes, if there were any, would be poorly defined and more difficult to detect in the difference spectra.

The 1741 cm^{-1} band in the difference spectrum has its origin in the lipid that remains bound to the protein after the last step of the purification. The band appears negative, meaning that the time-inactivated protein retains fewer lipids per protein than the c-atr-inhibited protein. From the area of this band, we conclude that the time-inactivated form retains one third less phospholipid than the inhibited form. This represents a reduction of six phospholipids per Anc2p dimer (Lórenz et al., 2001).

The structural changes presented in Figs. 1 and 2 point to an aggregation process. To rule out the possibility that this aggregation is due to the low concentration of water during film preparation, we obtained the Anc2pHis spectra in solution (for the time-inactivated and c-atr-inhibited forms) together with the difference spectrum. Fig. 2 *C* shows that the level of change in secondary structure (5% of the amino acids involved in the structural change) is similar to that of dry film, but the low S/N and baseline uncertainty reduce the precision of the data obtained from this experiment.

Detailed analysis of the difference spectrum

If our interpretation of the difference spectrum in Fig. 2 *B* is correct, this is an interesting opportunity to gain some insight into the infrared bands corresponding to short segments of only 10 amino acids in a protein composed by more than 300. We used two approaches to obtain this information. The difference spectrum in Fig. 2 *B* was deconvoluted and curve-fitted allowing for an unknown Lorentzian-Gaussian character for the bands (Fig. 3 *A*). In this way, we obtained the

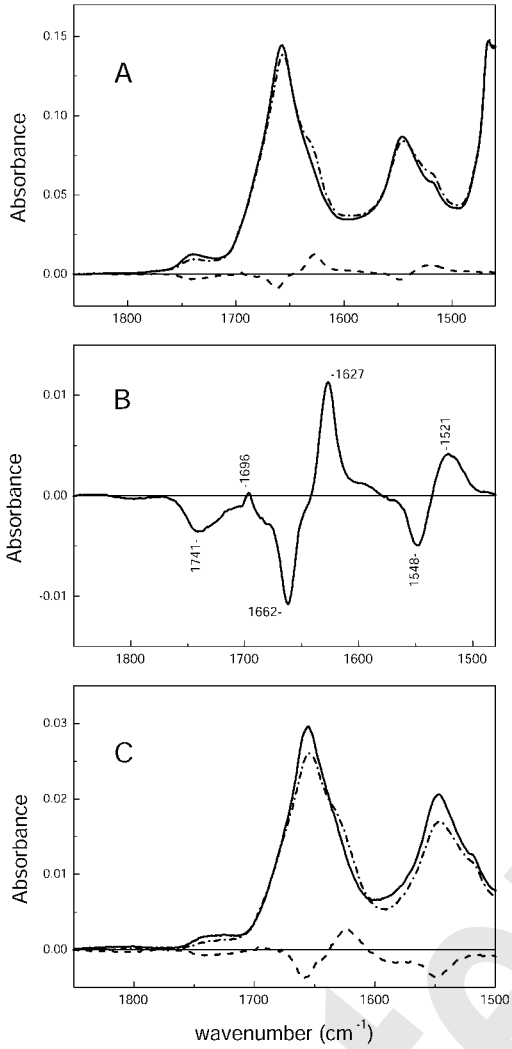

FIGURE 2 (*A*) (——) Dry film of DM solubilized c-atr-inhibited Anc2pHis and (-·-·-) time-inactivated Anc2pHis spectrum scaled to have the same area in the amide I. A DM spectrum was subtracted to compensate differences in the amount of retained detergent. (·····) Difference spectrum between time-inactivated and inhibited forms. (*B*) Difference spectrum in a expanded scale. (*C*) (—) DM solubilized c-atr-inhibited Anc2pHis and (-·-·-) time-inactivated Anc2pHis in solution scaled to have the same area in the amide I. (·····) Difference spectrum between time-inactivated and inhibited forms.

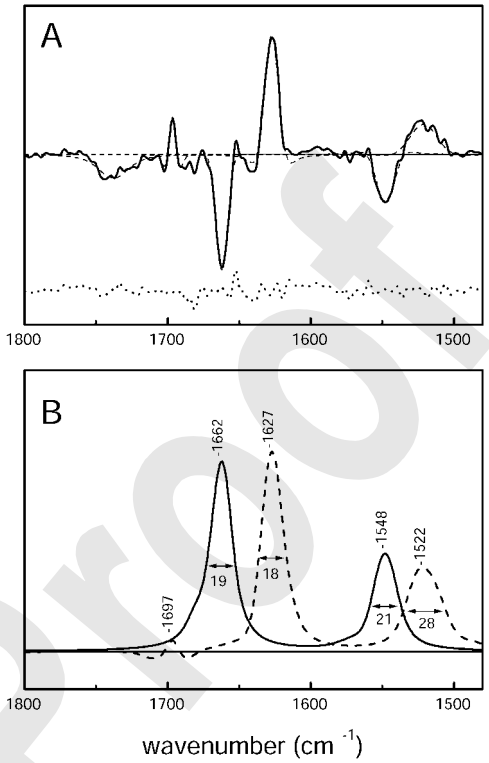

FIGURE 3 (*A*) (——) FSD ($\gamma' = 14$ cm^{-1}, $k = 2$ and Gaussian apodization) of the difference spectrum in Fig. 2 *B*. (- - - - -) Curve-fitting with Voigt bands allowing for Lorentzian-Gaussian character. (·····) Curve-fitting residual shifted down for a clearer display. (*B*) Bands in *A* were extracted and convoluted with a Lorentzian profile of 14 cm^{-1} width. Positive bands in the difference spectrum are shown in continuous line; negative bands are shown in dotted line.

position, area, width, and Lorentzian character percentage for the appearing and disappearing bands. The band parameters obtained are presented in Table 2.

The second approach to study the bands in the difference spectrum also applies FSD but afterwards we do not perform curve-fitting; instead, we extract the resolved bands and reverse the deconvolution process. Fig. 3 *B* shows the amide I and II bands of the lost structures (*continuous line*) and of the new structure (*dotted line*). The advantage of this approach is that we do not need to assume a parametric form for the bands; we only assume that, after FSD, the bands were almost completely resolved.

The results of both analyses can be compared to those of deconvolution of the original spectrum presented in Table 1. We will focus first on the amide I. In the difference spectra, a band disappears at 1662.0 cm^{-1} with a FWHH of 16 cm^{-1}, whereas from Table 1 a band at 1657.4 cm^{-1} with a FWHH of 28 cm^{-1} reduces its area and a band at 1668 cm^{-1} with FWHH of 24 cm^{-1} increases its area. On the other hand, in the difference spectrum a band appears at 1627.3 cm^{-1} with a FWHH of 16 cm^{-1}, whereas from Table 1 a band at 1627.4 cm^{-1} with FWHH of 20 cm^{-1} increases its area. For a protein of this molecular weight the bands obtained by curve-fitting the deconvoluted spectra most likely describe several protein segments whose positions are close enough to remain unresolved. Because frequency proximity usually agrees (with exceptions) with structure similarity for the amide I, the validity of deconvolution plus curve-fitting to predict secondary structure should remain in most cases. However, the use of deconvolution plus curve-fitting to describe subtle structural changes between two states seems less precise than the use of difference spectroscopy combined with curve-fitting or/and deconvolution, since for the first case, the same bands that describe the spectrum also have to describe the changes, which may involve only part of the structure

TABLE 2

Position*	FWHH*	L†	Area	Assignment
1696.4	7	15	+0.2‡	Intermolecular strands
1662.0	16	80	−3.6‡	Large loops
1627.3	16	40	+3.4‡	Intermolecular strands
1547.8	20	40	−3.4§	Large loops
1521.3	28	25	+3.5§	Intermolecular strands

Summary of the curve-fitting to the deconvoluted difference spectrum (noninhibited minus carboxyatractyloside-inhibited Anc2pHis dry film; see Fig. 3 *B*).
*In cm^{-1}.
†Lorentzian intensity percentage.
‡Area percentage with respect to the amide I area.
§Area percentage with respect to the amide II area.

contributing a given component. For the present analysis, the negative band at 1662 cm^{-1} in the difference spectrum requires the variation of two bands in the curve-fitting of deconvoluted spectra (an increase at 1668 and a decrease at 1657 cm^{-1}).

In the case of the amide II region, a band disappears at 1548 cm^{-1} with a FWHH of 20 cm^{-1}, another appearing at 1522 cm^{-1} with a FWHH of 28 cm^{-1}. Amide II bands appear broader and closer than amide I bands.

Reconstitution of Anc2pHis into liposomes and lipid-protein interactions

We first checked the efficiency of the reconstitution by following the lipid/protein ratio obtained in proteoliposomes. From the ratio C=O to amide I of the spectrum of a dry sample, we estimated that both the initial and final lipid/protein ratio in the reconstitution mixtures of the time-inactivated form was 3 (w/w). The efficiency was similar to that of the inhibited protein, where a lipid/protein ratio ~3 was also estimated. Nevertheless, for unknown reasons (probably protein segregation), when mitochondria were not preincubated with atr, the time-inactivated form showed low reconstitution efficiency, giving rise to lipid/protein ratios of 6 or higher.

FTIR analysis of reconstituted Anc2pHis

Fig. 4 *A* shows the absorbance spectra of the time-inactivated reconstituted form (with and without the amino acid side-chain contribution). Fig. 4 *B* displays the deconvoluted spectrum of the side-chain-corrected spectrum, along with that of the inhibited form. Both spectra present differences compared with their solubilized counterparts, suggesting that reconstitution affects the protein structure. Again, the time-inactivated form shows strong bands at 1697 and 1628 cm^{-1} pointing to an aggregation process. The deconvoluted spectra were curve-fitted (not shown). The band differences are similar to those of the solubilized form: the A band at 1659 cm^{-1} decreases its area, whereas bands at 1628, 1670, and 1696 cm^{-1} increase their area. The net result is an increase of turn (+9%) and sheet (+6%) structures and a decrease of helix and unordered structures (−15%).

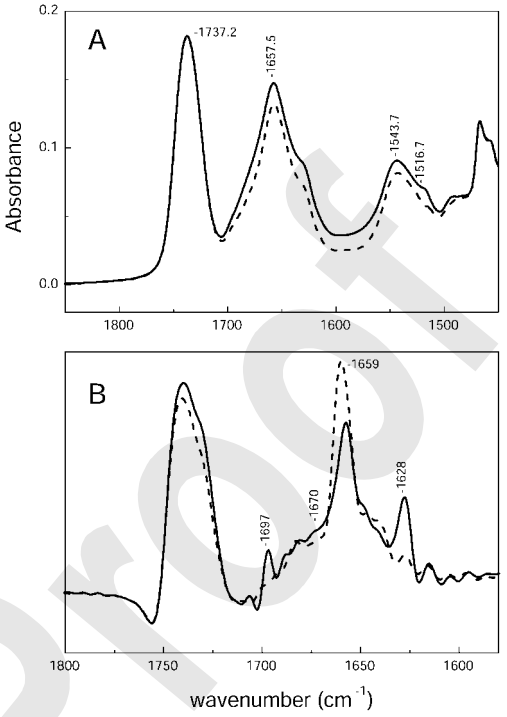

FIGURE 4 (*A*) (——) Attenuated total reflection-FTIR spectrum of a dry film at 25°C of the reconstituted time-inactivated Anc2pHis, corrected for amino acid side-chain absorption. Spectrum S/N was 6500. (*B*) FSD ($\gamma' =$ 18 cm^{-1}, $k = 3$, and Bessel apodization) of (——) the time-inactivated Anc2pHis and (- - - - -) the inhibited Anc2pHis.

Difference spectroscopy between both states (Fig. 5 *A*) gave similar results to those of the solubilized form either in shape or position (compare Fig. 2 *A* with Fig. 5 *A*), with bands appearing at 1696, 1628, and 1524 cm^{-1} and disappearing at 1661 and 1547 cm^{-1}. The difference spectrum for the amide A band gave a band disappearing at 3300 cm^{-1} and a band appearing at 3240 cm^{-1}. The difference spectrum for the amide A was not centered at zero, probably due to slight differences in the amount of retained water in the films. In keeping with amide I and II results, the appearing band can be assigned to β-sheets. Bands at 3300 cm^{-1} have traditionally been assigned to helices (Goormaghtigh et al., 1994a), whereas, to our knowledge, amide A band position for unordered or large loop structures has not been reported.

The amide I difference spectrum was studied further, by FSD followed by curve-fitting and by FSD followed by band isolation and convolution. The results from FSD-band extraction-convolution are presented in Fig. 5 *B* for the amide A, amide I, and amide II bands. The amide I changes accounted for 15% of the amide I area, and so ~7.5% of the protein (25 amino acids) was involved in the structural changes. For rehydrated films (bulk H_2O is deposited over the dry film) amide I difference spectra bands appeared roughly at the same positions (not shown).

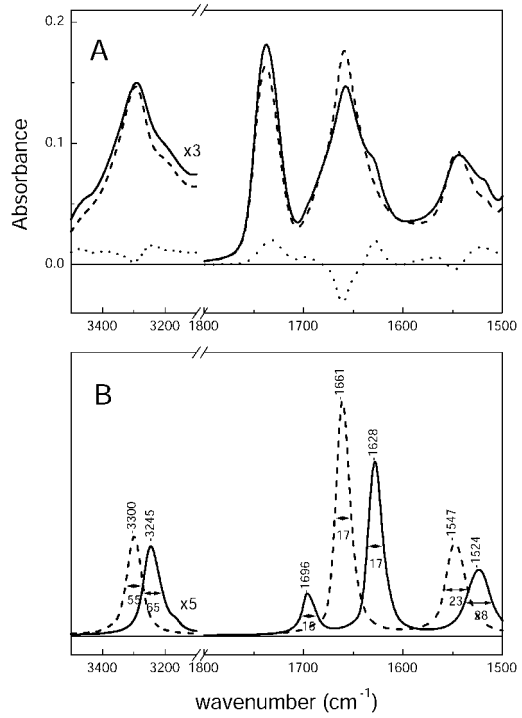

FIGURE 5 (*A*) Samples reconstituted in phospholipid vesicles. (——) Time-inactivated Anc2pHis spectrum and (- - - - -) c-atr-inhibited Anc2pHis spectrum scaled to have the same area at the amide I. (·····) Difference spectrum between the time-inactivated and inhibited reconstituted Anc2pHis. (*B*) Bands in the difference spectrum where resolved by deconvolution, baseline-corrected (for the amide II), extracted, and convoluted back. Band positions and FWHH are displayed. Positive bands in the difference spectrum are shown in continuous line; negative bands are shown in dotted line.

Therefore, it must be concluded that, although different in magnitude from a solubilized to a reconstituted state, the structural changes that prevent the Anc2p from binding its substrates/inhibitors are of the same type, independently of the presence of phospholipid or DM. In other words, once the structural changes that prevent substrate binding happen in the solubilized state, they cannot be reverted by reconstitution into liposomes. In the reconstituted form, the structural differences appear larger, but this is probably because the reconstituted form is obtained later than the solubilized form. In fact, we observed that the intensity of the difference spectrum increases, with time, the sample spent stored.

Effect of SDS

SDS is considered a denaturing detergent promoting the formation of helical segments, preventing the formation of intermolecular interactions and reducing the tertiary interactions (D'Auria et al., 1997; Muga et al., 1993; Torres et al., 1995). Therefore, we analyzed the effect of SDS on both forms of Anc2pHis, in an attempt to distinguish conformational differences caused by the presence or absence of the inhibitor.

When the time-inactivated reconstituted Anc2pHis was solubilized in SDS, a strong structural rearrangement occurred. The aggregation bands disappeared from the IR spectra (Fig. 6), that consisted mainly in an intense and relatively narrow band at 1657 cm^{-1} (70% of the amide I area). However, for the inhibited form the SDS-solubilized protein showed an IR spectrum similar to that of the inhibited form solubilized in DM. It seems that in the absence of inhibitor the protein structure is strongly dependent on the solubilizing detergent. This is coherent with a labile structure for the protein in the absence of inhibitors, that tends either to aggregate (in DM) or to rearrange (in SDS) in accordance with the detergent nature. On the other hand, the structure of the inhibited form is highly insensitive to the detergent nature, probably due to the stabilizing presence of the c-atr.

Orientation experiments

To better perceive the nature of the structure lost in the native to time-inactivated transition, orientation experiments were performed. Based only on band position, the disappearing band at 1661 cm^{-1} cannot univocally be assigned either to transmembrane helices or to unordered structures. Transmembrane helices have a tendency to be ordered to some degree with respect the lipid bilayer normal, hence their amide I and II bands will appear in a dichroism spectrum. Therefore, we compared these bands with those of the difference spectrum. Fig. 7 *A* shows the polarized spectra for the c-atr-inhibited Anc2pHis, together with its dichroism spectrum. The amide bands appeared in the dichroism spectrum at 3296 cm^{-1}, 1658 cm^{-1}, and 1548 cm^{-1}. Even after FSD (see Fig. 7 *B*) the dichroism spectrum appeared rather simple, although two bands were resolved in the amide

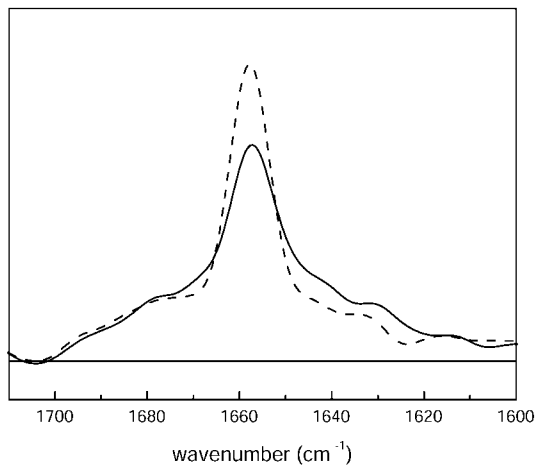

FIGURE 6 Deconvoluted attenuated total reflection-FTIR absorption spectrum (*continuous line*) of the reconstituted c-atr-inhibited Anc2pHis incubated with SDS. Spectrum for the time-inactivated form incubated with SDS (*dashed line*). Deconvolution was performed with $\gamma' = 18$ cm^{-1}, $k = 2.3$, and Bessel filter, and spectra were scaled to the same area between 1700 and 1615 cm^{-1}.

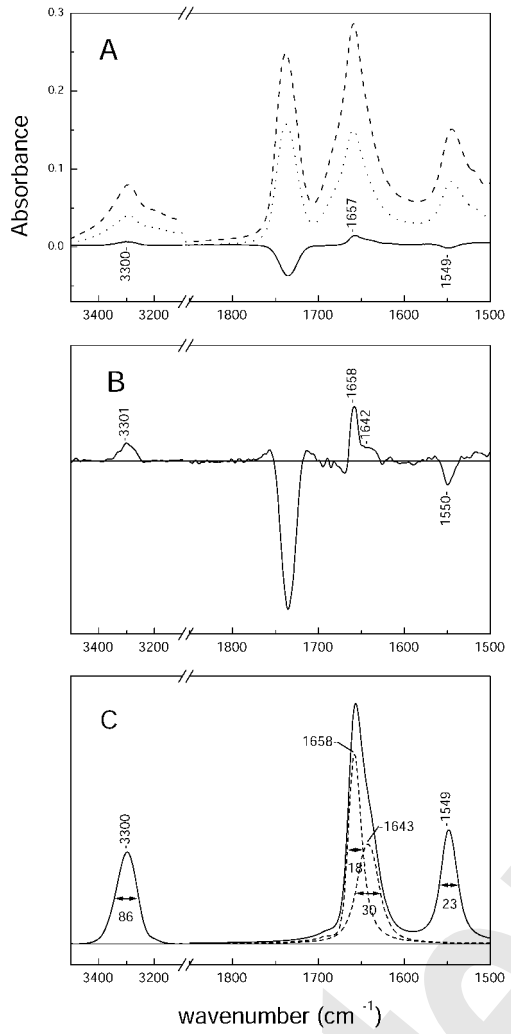

FIGURE 7 (*A*) Attenuated total reflection-FTIR absorption spectrum of the reconstituted Anc2pHis inhibited with c-atr when: (- - - - -) the IR beam was polarized at 90° (Abs_{90}) and (·····) the IR beam was polarized at 0 degrees (Abs_0). (——) Dichroism spectrum obtained as Abs_{90} - $R_{iso} \times Abs_0$ (see Materials and Methods for R_{iso} calculation). The value of R_{iso} at the amide I was 1.81. (*B*) FSD of the dichroism spectrum ($\gamma' = 16\ cm^{-1}$ and $k = 2$ at the amide I and II, and $\gamma' = 50\ cm^{-1}$ and $k = 1.7$ with Gaussian apodization). (*C*) Band obtained after extracting and convoluting the bands in *B*. For the amide I, where the bands are not totally resolved after FSD, the assumptions that the 1658 cm^{-1} deconvoluted band had no absorption down 1643 cm^{-1}, and that the band at 1642 cm^{-1} was symmetrical, were used.

I. In Fig. 7 *C* we present the amide A, I, and II bands for the oriented structures. The band at 1658 cm^{-1} can be assigned to typical transmembrane α-helices, whereas the assignment of the 1643 cm^{-1} is less clear, although it is not important for the present study.

Before we can compare the position of the transmembrane α-helices in the dichroism spectrum with the position of the disappearing band in the difference spectrum we must consider the following: infrared bands coming from α-helices have two close components in the amide I (an intense component and a less intense component at a $\approx$ 4–6 cm^{-1} lower frequency, with different dichroism; see Reisdorf and Krimm, 1995). In absorbance spectra both show positive sign, therefore the α-helix band maximum appears at a slightly lower frequency than the main component. In contrast in a dichroism spectrum of a transmembrane α-helix, the main band has positive intensity, whereas the small band shows negative intensity, the result being a positive band at a higher frequency than the main component. From the position of the band in the dichroism spectrum at 1658 cm^{-1} we can estimate that for the absorbance spectrum the transmembrane α-helix band maximum will be $\sim$1657 cm^{-1}. Therefore, the transmembrane helix seems not to be the structure that disappears in the difference spectrum (at 1661 cm^{-1}), since there exists a 4 cm^{-1} gap in their positions.

DISCUSSION

The Anc2p shows high instability when solubilized, making it difficult to obtain the Anc2p in a native state at sufficient purity for long-term spectroscopic structural studies. We hypothesize that the high tendency of the Anc2p to undergo a structural change that suppresses the binding of its natural substrates/inhibitors could be related to its structural conformation and dynamics in the solubilized state. We aimed at determining the structural changes that prevent Anc2p from binding its substrates/inhibitors, and the cause of this tendency. To this end, Anc2pHis inhibited by c-atr was used as a structural model for Anc2pHis in the *CATR* conformation, and compared with the noninhibited Anc2pHis (that represents unliganded time-inactivated Anc2pHis) by means of FTIR spectroscopy.

Two methods have been used to analyze the structural information contained in the FTIR spectra. First, the protein amide I deconvoluted spectra were curve-fitted and the results compared among the different states. Second, the amide I and amide II (and the amide A in some cases) difference spectra between two states was calculated. Curve-fitting of deconvoluted spectra has the advantage over difference spectroscopy, in that we obtain an estimation of the secondary structure for the studied states. On the other hand, difference spectroscopy has the advantage that spectral features of common structural motives are cancelled out in the subtraction, and differences only appear in the form of positive and negative bands. Therefore, difference spectra seem more appropriate to analyze structural changes between two similar protein states.

When the structure of the noninhibited time-inactivated Anc2pHis was compared to that of the c-atr-inhibited Anc2pHis through the amide A, amide I, and amide II difference spectra, seven well-resolved bands appeared. They were interpreted as arising from formation of intermolecular β-sheets in the time-inactivated state, with bands appearing at 3240, 1697, 1628, and 1524 cm^{-1}. The corresponding disappearing bands at 3300, 1662, and 1547 cm^{-1} come from residues participating in some helix or nonordered structures

in the c-atr-inhibited form. We propose that the structure that disappears in this process corresponds to nonordered structures; more specifically, to large loops. First, it is conceptually difficult to regard a transmembrane helix as a structure prone to forming intermolecular β-sheets without a gross reorganization of the protein structure. Moreover, from data based on the dichroism spectrum, we have shown that the amide I band position of transmembrane helices is shifted by 4 cm^{-1} from the disappearing structure. On the other hand, helices in soluble domains give bands down to 1656 cm^{-1} for the amide I (Goormaghtigh et al., 1994b). Large loops and atypical nonperiodic structures have been assigned at 1655 cm^{-1} in D_2O solutions (Prestrelski et al., 1991; Surewicz and Mantsch, 1988); therefore, in H_2O, they should be expected $\sim$1665–1660 cm^{-1}. The disappearing structure at 1662 cm^{-1} most probably corresponds to this group.

Therefore, FTIR results point to structured large loops (rather than unordered structures) as the feature that is lost on aggregation, although the conclusions we will draw are mainly unaffected by the assignment to large loops or unordered structures. These results were independent of Anc2pHis being in the solubilized state (in DM) or reconstituted (in egg PC/PA), although the number of amino acids involved in the structural changes was higher in the reconstituted form that in the solubilized form. This is probably a time effect, as the reconstituted form requires more time to be obtained than the solubilized form.

From band area quantification, it can be estimated that after a change in the structure of only $\sim$11 amino acids, the binding ability of the protein is lost. This implies that the structure lost in the transition from the *CATR* conformation to time-inactivated Anc2pHis plays a key role in the binding capability. Our hypothesis is that, per Anc2p dimer, at least two (topological) loops facing the matrix side (the so-called M loops; see Fig. 8) form structurally large loops (or unordered structures) which can aggregate to form intermolecular β-sheets, making the protein nonfunctional. This is supported by the evidence that the M loops play an important functional role in the protein, being involved in the substrates/inhibitors binding (especially the M2 loop; see Bogner et al., 1986; Dalbon et al., 1988; and Dianoux et al., 2000), substrates transport (Brandolin et al., 1993a; Majima et al., 1994), and perhaps forming a portion of the translocation pathway (Kaplan, 1996; Klingenberg, 1989). Moreover, the M loops contain many conserved residues (Brandolin et al., 1993a), and some of them have been proven to be essential for the protein function as revealed from site-directed mutagenesis (Müller et al., 1996, 1997). We discarded the involvement of the cytosolic loops in the aggregation process for two reasons: no functional role has been suggested for them, and the C loops are apparently too short to aggregate forming intramolecular β-strands without a more important rearrangement of the protein conformation (Fig. 8).

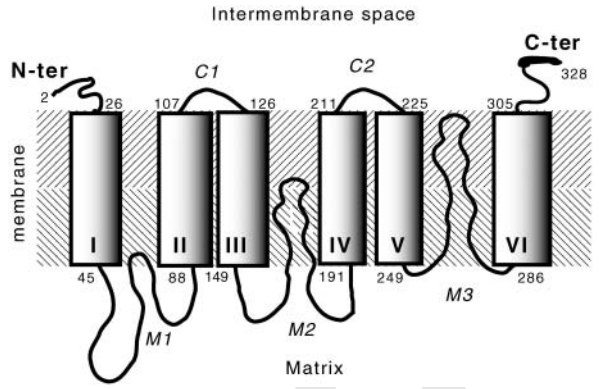

FIGURE 8 Topological model of Anc2p from *S. cerevisiae*. His-tagged Anc2p (328 amino acids) contains six putative transmembrane segments (TMS, I–VI) connected by two cytosolic (C1 and C2) and three matrix (M1, M2, and M3) hydrophilic loops. Arabic numbers denote amino acid positions in the primary structure at the beginning and at the end of each putative TMS. Mature Anc2p starts with an *n*-acetylated N-terminal Ser and is only 317 residues long (Dianoux et al., 2000). Bold line at the C-ter denotes the polyhistidine tag.

In the *CATR* conformation none of the M loops is accessible to membrane impermeable chemical reagents from either the matrix or the cytosolic side, whereas, in the *BA* conformation, the loop M1 and, to a lesser degree, the loop M2 are accessible only from the matrix side (Majima et al., 1994). Enzymatic proteolysis studies showed that the M loops are only accessible from the matrix side in the *BA* conformation, and not from the cytosolic side nor in the *CATR* conformation (Marty et al., 1992). The interconversion between the *BA* and *CATR* conformations (involved in the ADP/ATP transport) seems to consist mainly in the intrusion into the transmembrane region of some of the M loops. Moreover, the loop M1 seems to have an especially high mobility in the *BA* conformation, as revealed by Cys crosslinking (Hashimoto et al., 1999; Majima et al., 1995), which is totally inhibited in the *CATR* conformation. It has been suggested that it acts as a gate for the ATP and ADP binding (Majima et al., 1995). The high mobility of the M1 loops (probably enhanced when solubilized) could allow the interaction between them to form a more energetically stable structure (an antiparallel β-sheet). Although M1 has not been directly related to the binding site, its aggregation could impose such a steric restriction that molecules as bulky as c-atr, BA, ADP, or ATP could not reach the binding site. Moreover, since the *BA* to *CATR* conformation transition involves some reorganization of the M1 loops, its aggregation could impede such a transition.

Although any of the three M loops could show a tendency to aggregation, we tentatively consider the loop M1 as the one that most likely aggregates, given the experimental evidences. We hypothesize that, due to unknown functional reasons, the M1 loop is highly dynamic and this dynamism causes a high instability when solubilizing the Anc2p. The c-atr-inhibited form is thought to be highly stable during

isolation because loop M1 is hidden (not accessible from the matrix side) and in a blocked *CATR* conformation (Hashimoto et al., 1999) that is stable even in the presence of SDS. The BA inhibited form would be partially stable because loop M1 is extended into the matrix but its mobility is probably restricted by the inhibitor presence. Noninhibited Anc2p obtained in the *CATR* conformation probably is able to equilibrate with the *BA* conformation in a relatively short time (hours), even in the absence of the substrates ATP/ADP, from where loops M1 can rapidly aggregate. Finally, when solubilization is performed in the presence of ATP or ADP, the *CATR* and *BA* conformations equilibrate very rapidly, and so the protein could become readily inactivated from the *BA* conformation. This sequence agrees with the stability sequence observed when isolating Anc2p (Klingenberg, 1989).

In conclusion, we hypothesize that the high mobility of a M loop (most probably the M1 loop) allows it to become accessible or inaccessible from the matrix side in the *BA* to *CATR* conformational transition. This high mobility could be responsible for the instability of the Anc2p in the solubilized state. Its aggregation, although affecting very slightly the protein structure, is accompanied by the loss of the protein binding sites. It should be pointed out that this is the first spectroscopic evidence of the importance of the M loops in Anc2p function.

This work was supported by grants Bio4-CT97-2119 from the European Commission to G.L., G.B., and E.P., BMC2000-0121 from the Dirección General de Investigación, MCYT, and 2001SGR00197 from the Generalitat de Catalunya, and fellowship 1998-FI-00215 from the Generalitat de Catalunya to V.A.L.-F.

[AQ2]

REFERENCES

Arrondo, J. L. R., A. Muga, J. Castresana, and F. M. Goñi.1993. Quantitative studies of the structure of proteins in solution by Fourier-transform infrared spectroscopy. *Prog. Biophys. Mol. Biol.* 59:23–56.

Bandekar, J. 1992. Amide modes and protein conformation. *Biochim. Biophys. Acta.* 1120:123–143.

Bogner, W., H. Aquila, and M. Klingenberg. 1986. The transmembrane arrangement of the ADP/ATP carrier as elucidated by the lysine reagent pyridoxal 5-phosphate. *Eur. J. Biochem.* 161:611–620.

Brandolin, G., J. Doussiere, A. Gulik, T. Gulik-Krzywicki, G. J. Lauquin, and P. V. Vignais. 1980. Kinetic, binding and ultrastructural properties of the beef heart adenine nucleotide carrier protein after incorporation into phospholipid vesicles. *Biochim. Biophys. Acta.* 592:592–614.

Brandolin, G., A. Le Saux, V. Trézéguet, G. J. Lauquin, and P. V. Vignais. 1993a. Chemical, immunological, enzymatic, and genetic approaches to studying the arrangement of the peptide chain of the ADP/ATP carrier in the mitochondrial membrane. *J. Bioenerg. Biomembr.* 25:459–472.

Brandolin, G., A. Le Saux, V. Trézéguet, P. V. Vignais, and G. J. Lauquin. 1993b. Biochemical characterisation of the isolated Anc2 adenine nucleotide carrier from *Saccharomyces cerevisiae* mitochondria. *Biochem. Biophys. Res. Commun.* 192:143–150.

Citra, M. J., and P. H. Axelsen. 1996. Determination of molecular order in supported lipid membranes by internal reflection Fourier transform infrared spectroscopy. *Biophys. J.* 71:1796–1805.

Dalbon, P., G. Brandolin, F. Boulay, J. Hoppe, and P. V. Vignais. 1988. Mapping of the nucleotide-binding sites in the ADP/ATP carrier of beef heart mitochondria by photolabeling with 2-azido[α-32P]adenosine diphosphate. *Biochemistry.* 27:5141–5149.

D'Auria, S., R. Barone, M. Rossi, R. Nucci, G. Barone, D. Fessas, E. Bertoli, and F. Tanfani. 1997. Effects of temperature and SDS on the structure of β-glycosidase from the thermophilic archaeon *Sulfolobus solfataricus*. *Biochem. J.* 323:833–840.

Dianoux, A. C., F. Noël, C. Fiore, V. Trézéguet, S. Kieffer, M. Jaquinod, G. J. Lauquin, and G. Brandolin. 2000. Two distinct regions of the yeast mitochondrial ADP/ATP carrier are photolabeled by a new ADP analogue: 2-azido-3′-O-naphthoyl-[β-32P]ADP. Identification of the binding segments by mass spectrometry. *Biochemistry.* 39:11477–11487.

Fiore, C., V. Trézéguet, A. Le Saux, P. Roux, C. Schwimmer, A. C. Dianoux, F. Noël, G. J. Lauquin, G. Brandolin, and P. V. Vignais. 1998. The mitochondrial ADP/ATP carrier: structural, physiological and pathological aspects. *Biochimie.* 80:137–150.

Fiore, C., V. Trézéguet, P. Roux, A. Le Saux, F. Noël, C. Schwimmer, D. Arlot, A. C. Dianoux, G. J. Lauquin, and G. Brandolin. 2000. Purification of histidine-tagged mitochondrial ADP/ATP carrier: influence of the conformational states of the C-terminal region. *Prot. Expr. Purif.* 19:57–65.

Goormaghtigh, E., V. Cabiaux, and J. M. Ruysschaert. 1994a. Determination of soluble and membrane protein structure by Fourier transform infrared spectroscopy. I. Assignments and model compounds. *Subcell. Biochem.* 23:329–362.

Goormaghtigh, E., V. Cabiaux, and J. M. Ruysschaert. 1994b. Determination of soluble and membrane protein structure by Fourier transform infrared spectroscopy. III. Secondary structures. *Subcell. Biochem.* 23:405–450.

Goormaghtigh, E., V. Raussens, and J. M. Ruysschaert. 1999. Attenuated total reflection infrared spectroscopy of proteins and lipids in biological membranes. *Biochim. Biophys. Acta.* 1422:105–185.

Hashimoto, M., E. Majima, S. Goto, Y. Shinohara, and H. Terada. 1999. Fluctuation of the first loop facing the matrix of the mitochondrial ADP/ATP carrier deduced from intermolecular cross-linking of Cys56 residues by bifunctional dimaleimides. *Biochemistry.* 38:1050–1056.

Heidkämper, D., V. Müller, D. R. Nelson, and M. Klingenberg. 1996. Probing the role of positive residues in the ADP/ATP carrier from yeast. The effect of six arginine mutations on transport and the four ATP versus ADP exchange modes. *Biochemistry.* 35:16144–16152.

Heimburg, T., and D. Marsh. 1993. Investigation of secondary and tertiary structural changes of cytochrome c in complexes with anionic lipids using amide hydrogen exchange measurements: an FTIR study. *Biophys. J.* 65:2408–2417.

Kaplan, R. S. 1996. Mitochondrial transport processes. *In* Molecular Biology of Membrane Transport Disorders. S. G. Schultz, T. E. Andreoli, A. M. Brown, D. M. Fambrough, J. F. Hofman, and M. J. Welsh, editors. Plenum Press, New York. pp.277–302.

Kauppinen, J. K., D. J. Moffat, H. H. Mantsch, and D. G. Cameron. 1981. Fourier transforms in the computation of self-deconvoluted and first-order derivative spectra of overlapped band contours. *Anal. Chem.* 53:1454–1457.

Klingenberg, M. 1989. Molecular aspects of the adenine nucleotide carrier from mitochondria. *Arch. Biochem. Biophys.* 270:1–14.

Klingenberg, M., E. Winkler, and S. Huang. 1995. ADP/ATP carrier and uncoupling protein. *Methods Enzymol.* 260:369–389.

Krämer, R., and M. Klingenberg. 1977. Reconstitution of inhibitor binding properties of the isolated adenosine 5′-diphosphate, adenosine 5′-triphosphate carrier-linked binding protein. *Biochemistry.* 16:4954–4961.

Krimm, S., and J. Bandekar. 1986. Vibrational spectroscopy and conformation of peptides, polypeptides, and proteins. *Adv. Protein Chem.* 38:181–364.

Le Saux, A., P. Roux, V. Trézéguet, C. Fiore, C. Schwimmer, A. C. Dianoux, P. V. Vignais, G. Brandolin, and G. J. Lauquin. 1996. Conformational changes of the yeast mitochondrial adenosine diphosphate/adenosine triphosphate carrier studied through its intrinsic fluorescence. 1. Tryptophanyl residues of the carrier can be mutated without impairing protein activity. *Biochemistry.* 35:16116–16124.

Lórenz, V. A., J. Villaverde, V. Trézéguet, G. J. Lauquin, G. Brandolin, and E. Padrós. 2001. The secondary structure of the inhibited mitochondrial ADP/ATP transporter from yeast analyzed by FTIR spectroscopy. *Biochemistry*. 40:8821–8833.

Lórenz-Fonfría, V. A., J. Villaverde, and E. Padrós. 2002. Fourier deconvolution in non self-deconvolving conditions. Effective narrowing, signal-to-noise degradation, and curve fitting. *Appl. Spectrosc.* 56:232–242.

Majima, E., K. Ikawa, M. Takeda, M. Hashimoto, Y. Shinohara, and H. Terada. 1995. Translocation of loops regulates transport activity of mitochondrial ADP/ATP carrier deduced from formation of a specific intermolecular disulfide bridge catalyzed by copper-o-phenanthroline. *J. Biol. Chem.* 270:29548–29554.

Majima, E., Y. Shinohara, N. Yamaguchi, Y. M. Hong, and H. Terada. 1994. Importance of loops of mitochondrial ADP/ATP carrier for its transport activity deduced from reactivities of its cysteine residues with the sulfhydryl reagent eosin-5-maleimide. *Biochemistry*. 33:9530–9536.

Marsh, D., M. Müller, and F. J. Schmitt. 2000. Orientation of the infrared transition moments for an α-helix. *Biophys. J.* 78:2499–2510.

Marsh, D., and T. Páli. 2001. Infrared dichroism from the x-ray structure of bacteriorhodopsin. *Biophys. J.* 80:305–312.

Marty, I., G. Brandolin, J. Gagnon, R. Brasseur, and P. V. Vignais. 1992. Topography of the membrane-bound ADP/ATP carrier assessed by enzymatic proteolysis. *Biochemistry*. 31:4058–4065.

Moffat, D. J., and H. H. Mantsch. 1992. Fourier resolution enhancement of infrared spectra data. *Methods Enzymol.* 210:192–200.

Muga, A., J. L. R. Arrondo, T. Bellon, J. Sancho, and C. Bernabeu. 1993. Structural and functional studies on the interaction of sodium dodecyl sulfate with β-galactosidase. *Arch. Biochem. Biophys.* 300:451–457.

Müller, V., G. Basset, D. R. Nelson, and M. Klingenberg. 1996. Probing the role of positive residues in the ADP/ATP carrier from yeast. The effect of six arginine mutations of oxidative phosphorylation and AAC expression. *Biochemistry*. 35:16132–16143.

Müller, V., D. Heidkämper, D. R. Nelson, and M. Klingenberg. 1997. Mutagenesis of some positive and negative residues occurring in repeat triad residues in the ADP/ATP carrier from yeast. *Biochemistry*. 36: 16008–16018.

Prestrelski, S. J., D. M. Byler, and M. N. Liebman. 1991. Comparison of various molecular forms of bovine trypsin: correlation of infrared spectra with x-ray crystal structures. *Biochemistry*. 30:133–143.

Reisdorf, W. C., Jr., and S. Krimm. 1995. Infrared dichroism of amide I and amide II modes of αI- and αII-helix segments in membrane proteins. *Biophys. J.* 69:271–273.

Roux, P., A. Le Saux, V. Trézéguet, C. Fiore, C. Schwimmer, A. C. Dianoux, P. V. Vignais, G. J. Lauquin, and G. Brandolin. 1996. Conformational changes of the yeast mitochondrial adenosine diphosphate/adenosine triphosphate carrier studied through its intrinsic fluorescence. 2. Assignment of tryptophanyl residues of the carrier to the responses to specific ligands. *Biochemistry*. 35:16125–16131.

Surewicz, W. K., and H. H. Mantsch. 1988. Conformational properties of angiotensin II in aqueous solution and in a lipid environment: a Fourier transform infrared spectroscopic investigation. *J. Am. Chem. Soc.* 110: 4412–4414.

Tamm, L. K., and S. A. Tatulian. 1997. Infrared spectroscopy of proteins and peptides in lipid bilayers. *Q. Rev. Biophys.* 30:365–429.

Torres, J., F. Sepulcre, and E. Padrós. 1995. Conformational changes in bacteriorhodopsin associated with protein-protein interactions: a functional αI-αII helix switch? *Biochemistry*. 34:16320–16326.

Venyaminov, S., and N. N. Kalnin. 1990. Quantitative IR spectrophotometry of peptide compounds in water (H2O) solutions. I. Spectral parameters of amino acid residue absorption bands. *Biopolymers*. 30:1243–1257.

Agradecimientos

"La felicidad no consiste en tener cosas,
sino en formar parte de ellas"
Chris Stevenson (Doctor en Alaska)

Durante más de tres años he estado pensando en qué decir, en qué agradecer y en cómo hacerlo. He escrito mentalmente decenas de agradecimientos, la mayoría indignos de ese nombre.

Soy tristemente consciente que ésta es la única parte atractiva de una tesis, lo único que será leído. Finalmente parece que la tesis es el epilogo de los agradecimientos. Es la fascinación y atracción de lo personal, privado y sentimental. Pero ¿quién puede agradecer lo que ha recibido sin que parezca poca cosa, en este mundo donde reina la exageración y las grandes palabras? Yo no soy capaz.

He recibido y he intentando dar las gracias devolviendo, o haciendo honor a lo recibido. En verdad, han sido cosas pequeñas, pero con la grandeza de lo real y genuino. En este aspecto quiero nombrar la apuesta de Esteve Padrós i Morell, dejándome buscar, con ciertas limitaciones razonables, mi camino y realizar mi investigación. Yo, por mi parte, creo haber hecho honor a la confianza depositada en mí, siguiendo mi camino hasta el final de mis fuerzas, y sin abandonar, muchas veces a mi pesar, las obligaciones adquiridas en la investigación del transportador ADP/ATP.

Objetivamente, creo que mis únicas deudas pendientes que tengo son una con mis padres, la cual sólo podré pagar en mis hijos, si los tengo; la otra conmigo mismo, por el desgaste físico y anímico que a supuesto la realización de este deseo en forma de tesis. El precio no ha sido baladí.

Subjetivamente, siento que debo disculpas a mucha gente por mi actitud, muchas veces distante, brusca, impersonal, y torpe. También por ser tan desagradecido. Realmente desearía poder decir lo que siento, pero carezco del valor, del ingenio y de la elegancia necesarios. Sí que puedo asegurar que he formado parte de Biofísica, de mi familia y de mis amigos. Que no puedo pensar en vosotros con indiferencia.

Memorama

"La vida se compone de unos pocos momentos aislados, sumamente llenos de sentido, y de infinitos intervalos en los que, a lo sumo, se proyecta sobre nosotros las sombras de esos momentos"

Friedrich Nietzsche

Me incorporé a la Unitat de Biofísica a finales de septiembre de 1997, y defenderé la tesis doctoral a finales de julio del 2003. Estos dos eventos forman un ciclo de casi seis años. Tanto la dedicación que requiere investigar, como el desplazamiento de València a Barcelona, han significado un cambio de hábitos, y a la postre un cambio en mi vida.

Llegué con muchos sueños, esperanzas, fantasías, pues tenía muchas cosas que mejorar en mi vida. Aunque no puedo decir que haya cumplido las expectativas más optimistas, he conseguido más de lo razonadamente esperable.

Como homenaje a estos años, y a la gente cuya vida se ha cruzada con la mía, quiere nombrar y recordar ciertos momentos de estos años, pues no habrá otra ocasión.

1) La visita que realicé a mi hermana Sofía a Lyón (Semana Santa de 1998). Recuerdo a Nadja.

2) Entre los momentos de felicidad más completa recuerdo las vacaciones que pasé en París (verano de 1998), con continuidad en la Bretaña, con mis hermanas Sofía y Ana, y con Fran, Fernando y Javier. Las largas e interesantes conversaciones alrededor de las botellas de porto, en las que había mucho que escuchar.

3) Para aprender a purificar el transportador ADP/ATP fui a Burdeos a principios de 1999. Estuve una semana y fui muy bien acogido. Es especial quiere destacar a Caterine.

4) En el verano de 1999 llegué a mi punto más bajo profesional (o *becaril*). Tenía que escribir la tesina y no tenía nada que contar. Los resultados experimentales eran pobres y no creía en lo que hacía. Hacer un ajuste o desconvolución me producía problemas de conciencia, pues era consciente de todas las incorrecciones en las que incurría. Decidí no presentar la tesina.

5) Durante el otoño de 1999 desarrollé mi primera idea propia: el uso de bandas Voigtianas en el ajuste de bandas Lorentzianas desconvuladas. Gracias a Quim y sus críticas pude ordenar mis ideas y conseguir que Esteve mostrará interés en este proyecto naciente, que a la postre crecería y se derivaría en los Resultados Teóricos de esta tesis.

6) La última reunión del proyecto europeo, a que pertenecía nuestro grupo, se realizó en Burdeos antes del verano del 2000. A destacar la cena en unos viñedos, una maratón de carcajadas, que no impidió disfrutar del vino y la comida.

7) En el verano del 2000 caminé, o mejor dicho, fui caminado por el Camino de Santiago. La compañía de Jaime y los encuentros realizados en el Camino lo convirtieron en un Viaje. No llegamos a Santiago, pero lo importante es el Camino. Experimenté la felicidad de la vida sencilla.

8) Después del verano del 2000, Natàlia se quedó sin beca. Pluriempleada, disminuyó su presencia en el laboratorio. Su ausencia hizo presente mi amistad por ella. Me había acercado demasiado a mi *archienemiga*.

9) En el congreso de Praga (septiembre del 2001) pasé unos días extraordinarios con Natàlia, Ana Andrés, Reiner, Markus y Jarmina. Sentí que formaba parte de algo. Cómo desearía pasar unos días en este recuerdo.

10) A finales del otoño del 2001 pasé los días más oscuros de estos seis años. Fueron dos semanas en las que me sentí fuera del mundo. El proceso se inició con una discusión tonta y acalorada con Natàlia. Sobre la verdadera causa desarrollé al menos cuatro hipótesis: (1) El vértigo por la caída me hizo caer. (2) Mi desconsideración por mi parte animal. (3) El miedo a una posición emocional frágil. (4) La conciencia de la posibilidad de crear algo de la nada. La interpretación que elegí fue la segunda, pues me permitía negociar con alguien para salir de este estado.

11) Uno de los días previos a la navidad del 2001, después de la celebración en el laboratorio, algunos de nosotros fuimos a tomar algo. Después de ciertas bajas, quedamos Julio, Natàlia, Dani, Ana Andrés y yo. Jugamos a diversos juegos en los que estaba involucrado el consumo de cerveza. Nos cambiamos los nombres, prohibimos decir *no*, y pronunciamos en diversos idiomas cierta frase de lealtad a los superiores. Lo más significativo de la noche pasó más adelante.

12) En enero del 2002 me puse muy enfermo. Me cuidó mi hermana Ana y después de madre. Por primera vez, tuve miedo de estar sólo. Somos débiles, necesitamos a alguien.

13) En septiembre del 2002 estuve una semana sólo en la casa del campo de mis padres, trabajando en la tesis. Me invadió una gran felicidad y paz.

14) Durante el invierno del 2002/3 conviví cierto tiempo con Empar. Quiero recordar especialmente los días que pasamos en Moià. Me inquirió sobre ciertos temas incómodos, muy incómodos. Tuve que pensar sobre ellos, en vez de evitarlos, y me sentó bien. Lo demás fue un placer absoluto, aunque dudo que ella se lo crea.

15) Finalmente, destacar el día que deposité la tesis. Me libré de dos pesos que me ahogaban desde hacía tiempo.

Es difícil destacar lo que no es singular, sino que aflora por acumulación. También es difícil recordar lo que fue y ya no es, pues seis años tienen sus momentos.

1) Las conversaciones que mantuvimos Quim, Natàlia y yo. Hablábamos de temas muy variados, con la sinceridad y simplicidad de no necesitar convencer, de querer compartir. Así empezamos a llevarnos mejor. 2) Las conversaciones entre mujeres en las que alguna vez me dejaron observar. El descaro y desparpajo de alguna/s de ellas (ya os podéis imaginar quién/es) aún me sonroja: Gracias a Ana Andrés, Carol, Merce, Mònica y Natàlia, me lo pasé muy bien. 3) El sofisticado sentido del humor de Ramon, y el efecto dominó que producía en las celebraciones, que pronto se convertían en celebración del ingenio. 4) La contundente y sincera manera de expresarse de Julio y Xavi, que en diferentes momentos han animado las cenas y fiestas. 5) Con Mónica y África pasé bastantes buenos momentos. Quizá tendría que haber surgido algo más que una profunda simpatía. 6) El contacto humano de Ana Andrés, que me fue tan necesario y tan agradable. 7) Algunas conversaciones con Mercè, en las que yo simulaba ser su hijo, y ella mi madre. 8) El tiempo que pasé con Makiko y Satoko, y la fascinación que generaron. 9) La extraña evolución de mi relación con Pau a través de los sueños. 10) El año que compartí piso con mis dos hermanas y Dario. 11) El nacimiento y crecimiento de Marcos, y el nacimiento de Diana, a la que al escribir estas líneas todavía no conozco. 12) La muerte de mi abuela María y mi tío-abuelo Manolo. 13) Mis actividades extra-investigadoras: estudiar japonés, cocina y danza contemporánea, y ir a la filmoteca. 14) Las fiestas que he pasado con Bernat, en especial en el festival de Benicàsim. 15) El tiempo que he pasado con los amigos/as de Ana, y el tiempo que pasé con los compañeros de trabajo de Sofía en Trama. 16) El tiempo, breve pero intenso, que pasé con Milos. 17) Los infinitos momentos que he dedicado a pensar sobre la desconvolución, la inversión de la transformada de Laplace y el ajuste.

Estos son algunos de los recuerdos que me llevaré. Supongo que con los años algunos de ellos irán cayendo, y que otros, ignorados o no valorados en su momento, aflorarán para reclamar su justo lugar.